Stony Brook University

Evolution of Gas Across Spiral Arms in the Whirlpool Galaxy

A Dissertation presented

by

Melissa Nicole Louie

to

The Graduate School

in Partial Fulfillment of the

Requirements

for the Degree of

Doctor of Philosophy

in

Physics

(Concentration - Astronomy)

Stony Brook University

December 2015

Stony Brook University

The Graduate School

Melissa Nicole Louie

We, the dissertation committee for the above candidate for the

Doctor of Philosophy degree, hereby recommend

acceptance of this dissertation

Jin Koda - Dissertation Advisor
Associate Professor, Department of Physics and Astronomy

Alan C. Calder - Chairperson of Defense
Associate Professor, Department of Physics and Astronomy

María Victoria Fernández-Serra - Committee Member
Associate Professor, Department of Physics and Astronomy

Héctor Arce - External Committee Member
Associate Professor, Astronomy Department, Yale University

This dissertation is accepted by the Graduate School

Charles Taber
Dean of the Graduate School

Abstract of the Dissertation

Evolution of Gas Across Spiral Arms in the Whirlpool Galaxy

by

Melissa Nicole Louie

Doctor of Philosophy

in

Physics

(Concentration - Astronomy)

Stony Brook University

2015

To investigate the dynamic evolution of gas across spiral arms, we conducted a detailed study of the gas and star formation along the spiral arms in the Whirlpool Galaxy, M51. This nearby, face-on spiral galaxy provides a unique laboratory to study the relationship between gas dynamics and star formation. The textbook picture of interstellar medium (ISM) evolution is rapidly changing. Molecular gas was once believed to form along spiral arms from the diffuse atomic gas in the inter-arm regions. Star formation occurs within giant molecular clouds during spiral arm passage. Lastly, the molecular gas is photo-dissociated back into atomic gas by massive stars on the downstream side of the spiral arm. Recent evidence, however, is revealing a new picture of the interstellar medium and the process of star formation. We seek development of a new picture by studying the development and evolution of molecular gas and the role of large scale galactic dynamics in organizing the interstellar medium.

This thesis begins by presenting work measuring the geometrical offsets between interstellar gas and recent star formation. Interstellar gas is traced by atomic hydrogen and carbon monoxide (CO). Star formation is traced

by ionized hydrogen recombination lines and infrared emission from dust warmed by young bright stars. Measuring these offsets can help determine the underlying large scale galactic dynamics. Along the spiral arms in M51, offsets between CO and the star formation tracers suggest that gas is flowing through the spiral arms, but the offsets do not show the expected signature of a single pattern speed and imply a more complicated pattern.

This thesis also examines the intermediate stages of gas evolution, by studying a denser component of the ISM closer to which stars will form. Only a small percent of the bulk molecular gas will become dense enough to form stars. HCN and HCO+ probe densities $\sim 10^4 \mathrm{cm}^{-3}$, where as the bulk gas is 500 cm^{-3}. This thesis looks at HCN and HCO+ emission in M51 across the central 7 kpc disk and localized along a region of spiral arm. This work combines observations that were made with the Green Bank Telescope (GBT) and higher resolution data using the Combined Array for Research In Millimeter-wave Astronomy (CARMA).

These observations show dense gas tracers are localized along the star forming spiral arms. In particular, there are regions where dense gas is present but there is no evidence of massive star formation. This may imply that the local environmental conditions, like temperature and velocity dispersion, or small scale physical processes, like turbulence and local gravitational collapse, are important for determining which gas will form stars. This new data also tests an existing relationship between dense gas and infrared emission. Previous work shows a linear relationship connecting distant galaxies and local star forming regions in our own galaxy. These new observations in M51 help fill in the four magnitude gap separating the galaxies and the star forming regions. The presence of an offset between observations in nearby galaxies suggest a change to the hypothesis of HCN tracing a 'basic unit of star formation' by include a secondary effect regulated by either the conversion from mass to light or the star formation efficiency.

To M, *I'm sorry I don't laugh at the right times...*

Contents

List of Figures

List of Tables

Acknowledgements

There are many people who have helped in allowing this thesis to come together. First and foremost, I want to send my sincerest regards to my advisor Jin Koda. I feel honored to be his first Ph.D student at Stony Brook. Since my first summer in graduate school, he have helped guide me to become the researcher I am today. He has always been available for discussions in his office, observing runs, and on Skype during his time at Caltech. I am grateful for his advice and company during my thesis work.

I would like to thank my thesis committee. First, I thank Alan Calder for acting as chairperson for my thesis committee and his useful advice and discussions throughout my time at Stony Brook. I would like to thank Marivi Fernández-Serra who served on my committee and provided expertise in fields outside of astronomy. I also thank Héctor Arce for participating on my thesis committee as an external member, as his expertise in astronomy was a welcome addition.

I send my warmest regards to the members of the Astronomy group at Stony Brook who have contributed immensely to my personal and professional time at Stony Brook. In addition, the larger Stony Brook Physics community, particularly, my housemates, Oumarou, Karen, and Kendra, and all of my classmates. Between homework sets and social gatherings, you all helped make my time at Stony Brook more memorable.

I extend my regards to Combined Array for Research in Milimeter-wave Astronomy staff, specifically, John Carpenter, for providing me with financial support to visit as an onsite observer multiple times throughout my thesis work. This provided an opportunity that played a crucial role in my understanding of interferometry. In addition, I thank David Frayer and the Green Bank Telescope Staff for help, support, and engaging discussions while on observing runs.

Lastly, I would like to thank my family for their love and support. For my parents who put up with me through all my pursuits. From space camps to lacrosse games, you provided me with an opportunity to explore my interests throughout my childhood, without which would not have lead me to purse a Ph.D. My brother, P.J. for encouragement while I contemplated my future pursuits. And most of all, my supportive and patient partner Monica, who has been my support system throughout my graduate career.

The text of this thesis in part is a reprint of the materials that appears in the Astrophysical Journal. The co-authors listed in the publications directed

and supervised the research that forms the basis for this thesis. Several images included in this thesis have been reprinted by permission of AAS.

This research made use of observations from the Combined Array for Research In Millimeter-wave Astronomy. Support for CARMA construction was derived from the Gordon and Betty Moore Foundation, the Kenneth T. and Eileen L. Norris Foundation, the James S. McDonnell Foundation, the Associates of the California Institute of Technology, the University of Chicago, the states of California, Illinois, and Maryland, and the National Science Foundation. Ongoing CARMA development and operations are supported by the National Science Foundation under a cooperative agreement, and by the CARMA partner universities. In addition, results are based on observations from the Green Bank Telescope, at the National Radio Astronomy Observatory in Green Bank, WV.The National Radio Astronomy Observatory is a facility of the National Science Foundation operated under cooperative agreement by Associated Universities, Inc.

Chapter 1

Introduction

The focus of this thesis is to determine how gas evolves across spiral galaxy structure and how this evolution impacts star formation. Studying the flow of gas across spiral arms and the formation of stars can also probe the dynamics of spiral structures. In this chapter, we begin by discussing the gas dynamics in spiral galaxies and leading theories of spiral arm structure and the composition of the interstellar medium (ISM). We will also review the classical theory for the evolution of gas across spiral arms and present more recent evidence to suggest a new picture of this evolution. We will describe some of the physical scales and processes associated with star formation. We explain how millimeter/sub-millimeter molecular emission allow for unique physical regions within the ISM to be studied, thus presenting an opportunity to develop and test a new picture of gas evolution.

1.1 Disk Dynamics in Spiral Galaxies

Spiral galaxies are some of the most recognizable structures in astronomy. They are commonly seen throughout the universe, two thirds of massive galaxies are spiral (Lintott et al. 2011). In addition, spiral galaxies have a wide range of structures, with many different classifications. Hubble classified galaxies via what is now known as the Hubble turning fork diagram, which is shown in Figure 1.1. The handle of the turning fork represents elliptical galaxies and disk galaxies with no visible spiral structure. The spiral galaxy sequence progresses to the right based on how tight the spiral structure appears. Spiral galaxies also fork into two separate classifications based

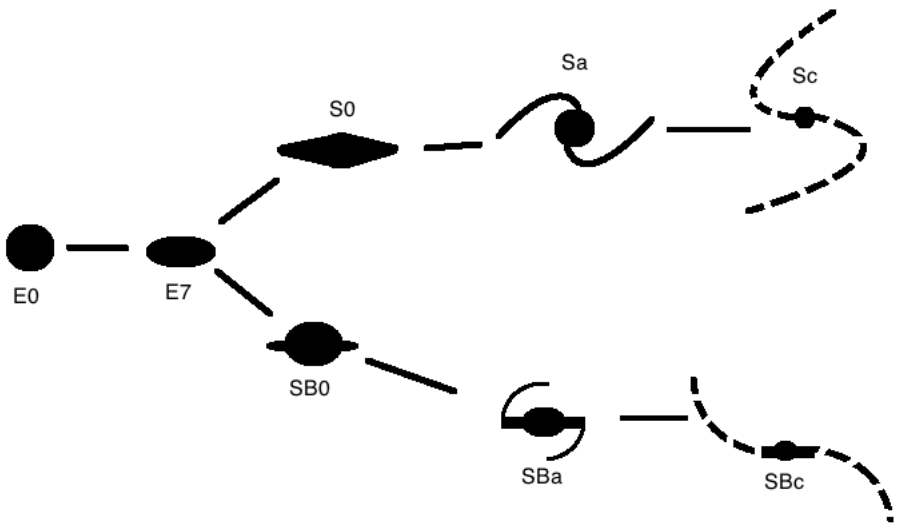

Figure 1.1 Hubble Tuning Fork Diagram for Galaxy Classification shows the wide range of spiral galaxy properties seen in the universe.

on the presence of a bar structure in the middle of the galaxy. New large scale surveys continue to show a wide variety in spiral structure (Lintott et al. 2011). Spiral arm structure is seen in observations of gas and dust in nearby galaxies. In addition, spiral arms appear to be associated with recent star formation. Despite the continued work in spiral arm structure theory, many questions still remain unanswered about the dynamics of spiral structure. This section outlines some of the main theories on the cause of spiral structure.

1.1.1 Quasi-static Density Wave

In the early 20th century, spiral arms were thought to be material arms that were physically moving around the galaxy. If spiral arms are material arms, over time, the differential rotation of the disk would cause the arms to wind up. Spiral structure would be lost in a few galactic rotations. Since spiral structure is commonly seen throughout the universe, it was thought unlikely for spiral structure to be a material arm. Lin & Shu (1964) first proposed that spiral arms are not material arms, but structures that appeared due to

regions within the disk with an enhanced density. Material in this 'density wave' would move slower than when outside of the density wave. Both stars and gas would move through the density wave. This density enhancement is caused by the orbits of the stars and gas. The stars and gas in spiral galaxies move in small epicyclic orbits while traveling on circular orbits around the center of a galaxy. This causes the material to rotate in nested elliptical orbits. This is one model of density wave theory.

Figure 1.2a shows a model of the nested elliptical orbits stars and gas may follow. When the axes of these orbits are aligned, a density enhancement will be seen along the major axis and may describe bar structures in galaxies. When the axes of these orbits are rotated, a spiral arm pattern can be seen. The density enhancement made by the slower velocities of the material at the ends of the elliptical orbits traces out a spiral structure (Binney & Tremaine 2008). Spiral structure can easily be generated by rotating nested elliptical orbits. These rotated orbits are seen in Figure 1.2b and where generated by rotating the nested elliptical orbits shown in Figure 1.2a.

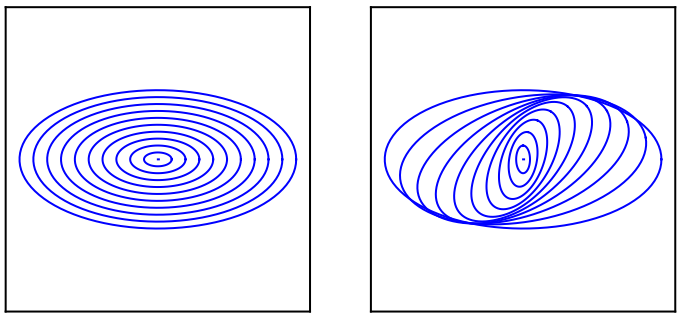

Figure 1.2 Nested elliptical orbits representing the stars and gas within a disk galaxy. (a) Shows the elliptical orbits without any rotation, which can explain galactic bar structures. (b) Rotated elliptical orbits showing how spiral structure may be generated in the quasi-static density wave theory.

The density wave theory predicts that spiral structure should be a long lasting, global event, effecting the entire galaxy. These standing waves in the stellar disk were considered to be *quasi-stationary* (Lindblad 1963). Following the work of Lin & Shu (1964), we can assume linear perturbation, tightly wound spiral arms, and quasi-stationary spiral structure, to write a dispersion relationship for a thin disk,

$$(\omega - m\Omega)^2 = c_{\rm s}^2 k^2 = \kappa^2 - 2\pi G\Sigma_{\rm o}|k|, \tag{1.1}$$

where Ω is the angular frequency and $c_{\rm s}$ is the sound speed. κ is the epicyclic frequency of the orbits and Σ is the surface density of the disk. ω is the angular frequency of the pattern and m is the number of spiral arms , these two define the pattern speed $\Omega_{\rm p} = \omega/m$. k is the radial wave number and is defined such that when $k > 0$, the spiral is a trailing spiral and when $k < 0$ the spiral is leading. Stable perturbations exist when $(\omega - m\Omega)^2$ is positive and this gives a condition for which density waves are stable,

$$Q \equiv \frac{\kappa c_{\rm s}}{\pi G\Sigma_{\rm o}}. \tag{1.2}$$

This quantity is known as the Toomre parameter. For longer wavelengths the waves are supported by pressure and shorter wavelengths are supported by rotation. Figure 1.3 shows the Lin-Shu dispersion relationship for a fluid disk for a range of Q values. Similarly, a dispersion relationship can be made for a stellar disk with

$$Q \equiv \frac{\kappa\sigma_{\rm R}}{3.36G\Sigma_{\rm o}} \tag{1.3}$$

where $\sigma_{\rm r}$ is the radial velocity dispersion in the disk (Kalnajs 1965; Lin & Shu 1966). In this picture gravity promotes collapse, whereas the stellar dispersion and angular momentum prevent collapse. Spiral structure is promoted when the disk is gravitationally unstable. This happens in environments with low stellar velocity dispersion, higher surface density, or small epicyclic frequencies.

The Toomre Q allows for the development of spiral structure and this structure can be perpetuated and amplified in a processes known as spring amplification (Toomre 1981). The spiral density wave is created by the organization of gas caused by epicycle motions of stars in the disk. A leading spiral arm is sheared while passing through the spiral arm due to differential rotation in the disk and become a trailing spiral arm upon leaving the spiral arm.

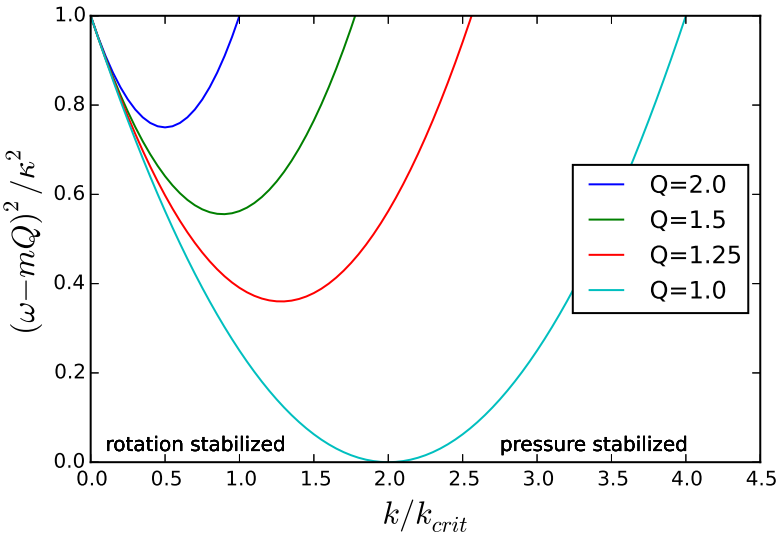

Figure 1.3 Dispersion relationship for density wave in a fluid disk. $k_{\rm crit}$ is defined as $\kappa/(2\pi G\Sigma_{\rm o})$. When a wave has a k less than $k_{\rm crit}$, it is considered a long wave and supported by rotation, and when k is greater than $k_{\rm crit}$, it is a short wave and supported by pressure.

1.1.2 Material Spiral Arms

Recent simulation work has reopened the discussion regarding the nature of spiral structure, specifically, that spiral arms are dynamic, transient, and local structures constantly undergoing change (Dobbs & Baba 2014, see recent review article). In the 1980's, N-body simulations began showing that spiral arm structures were generated from stellar disks (Sellwood & Carlberg 1984). Local over-densities would be sheered apart by differential rotation in the disk creating a spiral structure and will eventually break apart. These over-densities are compared to the average densities seen across the disk. Segments of the spiral structure will be constantly broken apart and rejoining other segments creating a constantly evolving spiral structure (Wada et al. 2011; D'Onghia et al. 2013). In some simulations spiral structures are seen to last for at least 10 Gyr (Fujii et al. 2011). As in the quasi-static stationary density wave theory, swing amplification is likely to play a role in the growth of perturbations in material spiral arms (Sellwood & Carlberg 1984).

1.1.3 Additional Theories of Spiral Arms

Tidal Interactions

Spiral structure can also be created via tidal interactions between two galaxies, like the response of the ocean tides by the Moon. Two-armed spiral galaxies with close companions have tidal perturbation which are built up due to swing amplification in the disk (Toomre & Toomre 1972). This tidal interaction could create the 'grand design' spiral pattern seen in galaxies like M51. Tidal interactions could produce a density wave driven arm or a material arm.

Bar Structure

Bar structure is common within spiral galaxies. 30% of spiral galaxies have bars (Masters et al. 2011). Bars have also been suggested to induce spiral structure. In barred spiral galaxies, spiral structure begins at the location where the bars end. This lead to the assumption that spiral structure is connected to the bar structure. Hydrodynamic simulations of bar structures in disks have been shown to create a steady state spiral structure (Sanders & Huntley 1976) but more recent numerical simulations have not shown any spiral structure in collisionless disks. A connection between spiral arms and

bars is possible, but it is unknown if it is physically based or only empirical coincidence (Mo et al. 2010).

1.2 Material Composition of Disk Galaxies

Spiral structure is seen throughout the various components within disk galaxies. It is seen in the distribution of stars, gas, and dust. Stars dominate the make up of the disk and influence the ISM, which is made up of gas and dust. To better understand how spiral structure can be observed and studied, this section give a brief description of these three components and how they are related to spiral structure and star formation.

1.2.1 Stars

The stellar component of galaxies dominates the structure of disks. The density wave theory, discussed in the previous section, describes the orbits of the stellar disk. In all disk galaxies, regardless of spiral arm type which can range from grand-design with two distinct arms or flocculent with many loosely connected spiral arms, the older stellar population dictates the gravitational potential (Binney & Tremaine 2008). Spiral arms have also been shown to have different spiral structure at different wavelengths. Observations have shown that the old stellar population can show a grand design spiral pattern in infrared observation, whereas, the young stellar population is shown to be more flocculent in optical observations (Block & Wainscoat 1991; Thornley 1996; Rix & Rieke 1993).

1.2.2 Gas

The global dynamics of the gas in the ISM can be dictated by the gravitational potential in the stellar disk. Gas and the associated recent star formation show a clear spiral arm structure. Gas only makes up a small fraction, 10% by mass, of the total disk (Sellwood 2013). Despite this, it is a very important component of the ISM, specifically to relate the spiral arm dynamics to physical processes regulating star formation. Gas is a key component of the star formation process as it is the material from which stars form. In the MIlky Way the ISM gas is 70 % hydrogen, 28% helium and 2% heavier elements

1.2.3 Dust

By mass, dust contains less than 1% of the total gas mass (Klessen & Glover 2014). Although it only represents a small fraction of the total ISM mass, dust grains aid in the formation of molecules, specifically molecular hydrogen (Gould et al. 1963). Dust is heated by nearby stars, specifically radiation from stars is absorbed by dust and reemitted as thermal radiation. Because of this, mid-infrared emissions are commonly used to trace warm dust heated by recent star formation (Kennicutt & Evans 2012). Dust also can cause extinction of light due to its high column density along the line of sight, but can also provide information on the structure of molecular clouds (Lada et al. 2007).

1.3 Gas Evolution Across Spiral Arms

Spiral dynamics leave an imprint on the ISM, which in turn can be used to test theories of spiral structure. Roberts (1969) proposed a clear evolutionary sequence of gas across spiral arms with a strong presence of gas on the upstream side of the spiral where gas enters the spiral enhancement and experiences a shock. Star formation appears on the downstream side of the spiral arm upon exit of the spiral potential. Figure 1.4 and Figure 1.5 illustrates the positions of the shock, gas, and young stars as predicted by Roberts (1969). In this Figure, the spiral is a trailing spiral inside the corotation radius where the gas and the density wave rotate at the same speed. Offsets are expected between the gas shock and young stars. Roberts (1969) supported this picture of gas evolution with observational evidence of HI peaks appearing at the entrance of the spiral pattern and Hα emission from young stars on the exit of the spiral pattern.

In this classic picture of gas evolution, spiral gas in the disk is primarily atomic, and is rotating around the galaxy. The gravitational potential of the stellar component causes gas to accumulate along the spiral arm. The gas slows as it enters and passes through the gravitational potential of the spiral arm. Molecular gas is formed due to shock along the spiral arms and is organized into giant molecular clouds (GMCs). Gravitational instabilities grow within the GMCs, and as the gas continues to move across the spiral arm, instabilities grow and become the sites of star formation. Newly formed stars appear on the downstream side of the spiral arm and the molecular gas

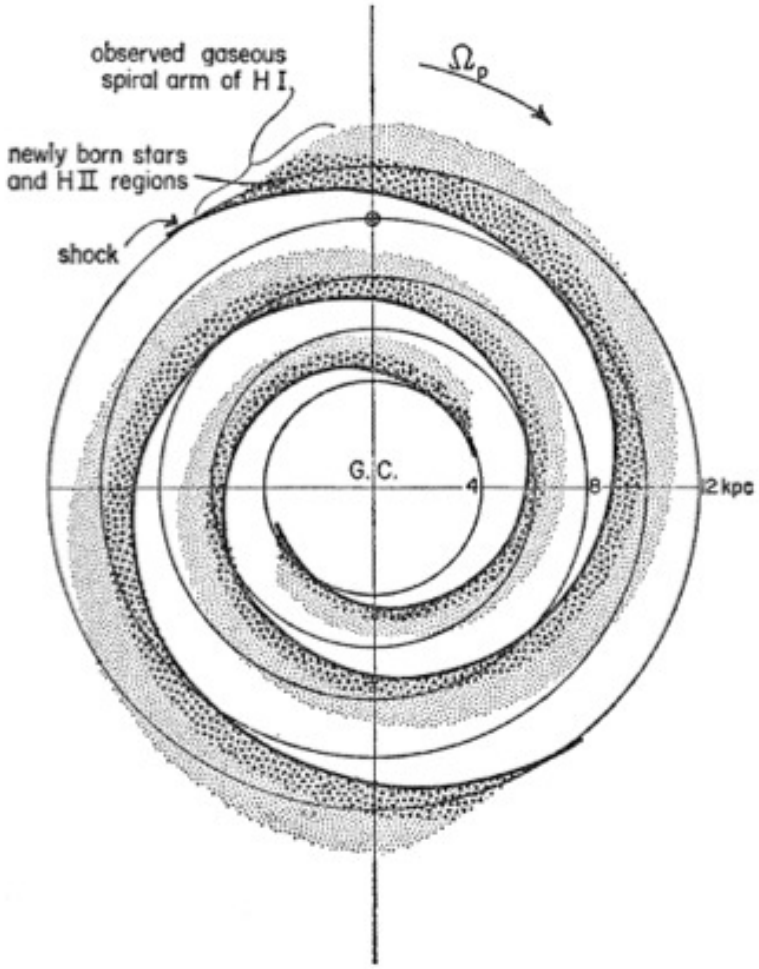

Figure 1.4 Illustration of the gas, young stars and shock associated with spiral structure in classical picture of gas flow across spiral arms as proposed in Roberts (1969). Face on view of the shock within the disk and the reaction from the gas. This is Figures 4 from Roberts (1969). These images are reproduced with permission from AAS.

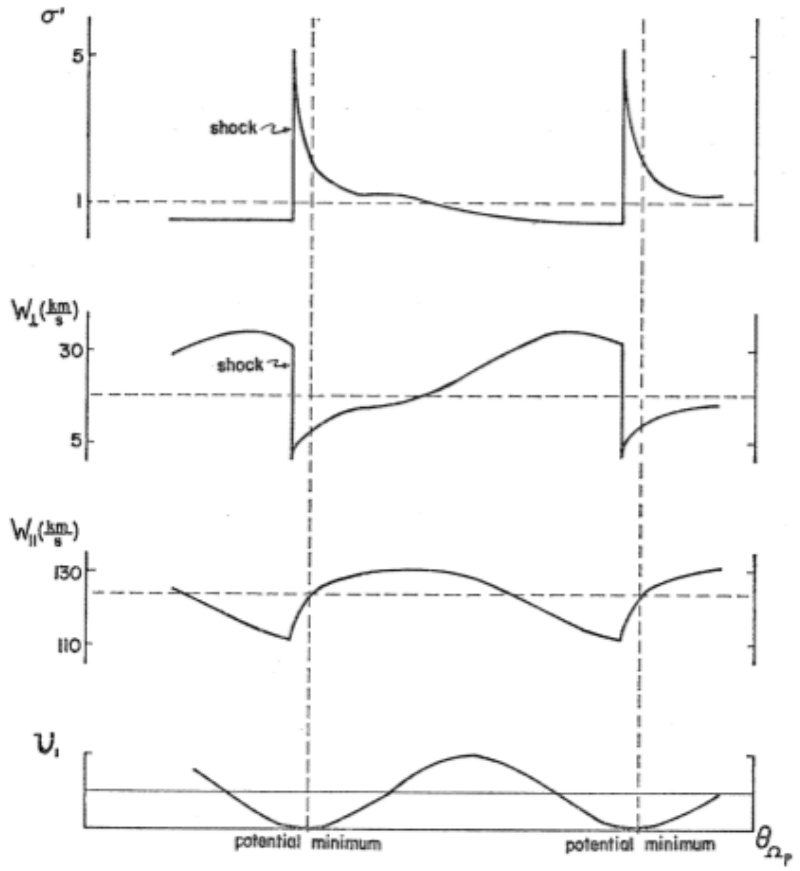

Figure 1.5 Azimuthal distribution showing (from top to bottom) density, perpendicular and parallel velocity of the gas, and the gravitational potential. This is Figure 5 from Roberts (1969). These images are reproduced with permission from AAS.

around the recently formed stars is photodissociated. This leaves the newly formed stars and atomic gas entering back into the next interarm region.

The clear evolutionary sequence suggested above can be directly tested in observations. Gas is seen to evolve across a spiral arm in IC 342, with GMCs without star formation markers on the upstream side and GMCs with star formation on the downstream side of the spiral arm (Hirota et al. 2011). In a study of nearby galaxies, Tamburro et al. (2008) found geometrical offsets between atomic gas and star formation tracers, as suggested by Roberts (1969). However, Egusa et al. (2004, 2009), also measured the geometrical offsets in a sample of nearby galaxies between molecular gas and star formation and measures larger offsets than those found previously by Tamburro et al. (2008). The offsets measured by Egusa et al. (2009) still appear ordered, but suggest that molecular gas, as opposed to the atomic gas, is the gas most relevant for studying gas evolution across spiral arms. This is backed up by Koda et al. (2009), who found that in M51 molecular gas remains present in the interarm regions and that GMCs are not formed along spiral arms but survive spiral arm passage. More recently, Foyle et al. (2011) reexamined the offsets from Tamburro et al. (2008) between atomic gas and star formation and expanded to include molecular gas. That work did not agree with the work by Tamburro et al. (2008) or Egusa et al. (2009) and reported non-ordered offsets compared to what would be predicted by the density wave theory. These works directly aimed to test the evolutionary sequence of gas as seen in nearby galaxies. The discrepancies seen between these works raise questions about the sequences of gas evolution proposed by Roberts (1969).

1.3.1 Working Hypothesis for Gas Evolution Across Spiral Arms

Recent observational evidence is suggesting a change in the evolutionary picture of gas across spiral arms. Figure 1.6 shows a schematic of one proposed model for gas flow across spiral arms. In this model, GMCs are present in the interarm regions. As they approach the spiral arm, they slow down as they enter the gravitational well produced by the stellar potential. This causes the small GMCs to combine into larger GMCs. These large GMCs continue to move across the spiral arm. Inside of the GMCs, gravitational instabilities lead to the formation of dense cores. Stars form from within

these dense cores, but are enshrouded by gas and dust. Over time, the material surrounding the star will dissipate and the stars will be left to shine. Any remaining molecular gas will be organized into smaller GMCs. Both the stars and GMCs will enter back into the next interarm region.

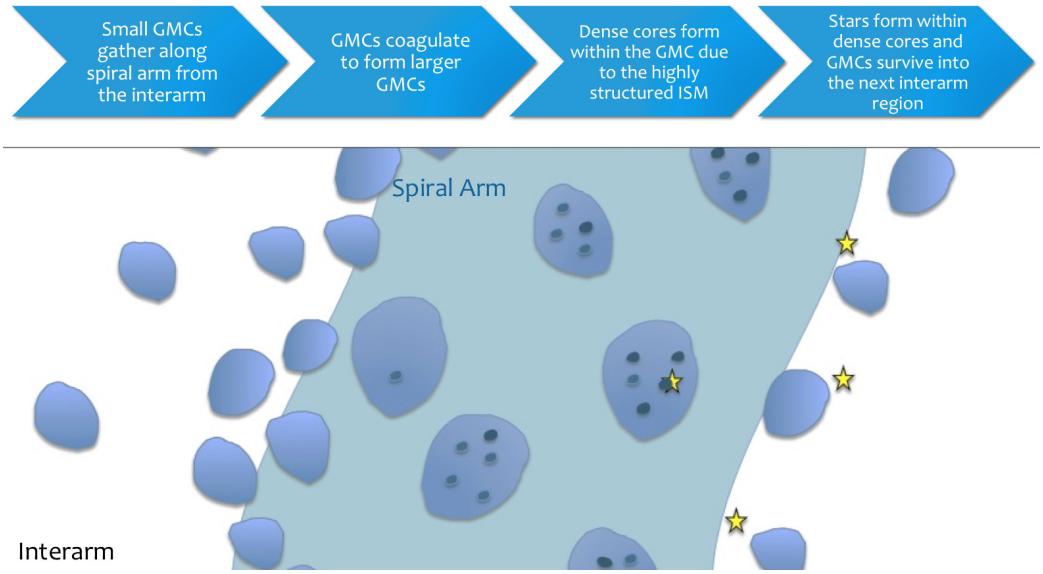

Figure 1.6 A proposed theory for the evolution of gas across spiral arms. This thesis aims to tests different aspects of this model and It focuses on studying the offsets between the gas on the upstream side of the spiral arm and the star formation on the downstream side of the spiral. In addition, we will look at dense star forming core development along spiral arms.

The proposed theory of gas evolution presented above is one that we will be testing throughout this thesis. This thesis focuses on two main aspects of Figure 1.6. First, we look at the geometric offsets between gas and star formation along the spiral arms in M51 (Chapter 3). We aim to resolve the tension between previous offset measurements and thus test our working theory of gas evolution. Next, we study the dense star forming gas associated along spiral arms to probe the intermediate stages of this proposed theory of gas evolution. HCN and HCO+ emission probes dense star forming regions that may not be spatially resolved due to the high densities required for their excitation. These emissions allow for a study dense star forming regions in M51 in the context of gas evolution (Chapter 4).

To understand the gas evolution across spiral arms one needs to determine the physical processes that act on various physical scales associated with star formation. Within the Milky Way, individual GMCs and dense star forming cores can be isolated and observed with a very high spatial resolution. However, connecting the gas evolution to spiral structure in the Milky Way is difficult given that we are located within the Milky Way. Spiral structure can be obscured due to our line of sights around/through the galaxy. On the other hand, observations of nearby galaxies have mainly been focused on the localized $\sim$ kilo-parsec regions within the disk (Bigiel et al. 2008) or disk averaged global influences (Regan et al. 2001). These provide environmental averages in a given region but tend to be over larger scales. Recent work is beginning to bridge the gap between galactic and extragalactic observations. Molecular gas structure and evolution in the Milky Way shows evidence of interarm gas being more diffuse but becoming more structured along spiral arms (Sawada et al. 2012). In nearby galaxies, GMC size scales ($\sim$ 50pc), can be observed over large scales and allow a direct comparison with global spiral structure (Schinnerer et al. 2013). Besides the most local galaxies, like the Large and Small Magellanic Clouds, it has been difficult until very recently, to study the conditions in individual extragalactic GMCs (Hughes et al. 2013). Large scale mappings of nearby galaxies at these GMC size scales are very time intensive and can not be done for all galaxies. In addition, even at these size scales, internal structure of GMCs can not be studied. The angular resolution required to match spatial scales in the Milky Way are extremely difficult to reach in extragalactic sources, although ALMA[1] will play a key role in this in the future. Other observational methods are required to be able to best compare Milky Way observations with nearby galaxies. One of these methods will be highlighted in §1.5.4, where we will show how HCN and HCO+ emission can be used to prove intermediate size scales and link galactic and extragalactic observations.

1.4 Scales of Star Formation

Observations suggest a strong link between galactic environment, gas evolution, and star formation. However, developing an evolutionary sequence of gas across spiral arms can be difficult due to the large range of physical

[1]Atacama Large Millimeter/submillimeter Array (ALMA)

scales involved in the star formation process. There are many orders of magnitude between global influences (kilo-parsec scales) and star forming dense gas cores (sub-parsec scales). Understanding the interplay between them is key to understanding star formation. Figure 1.7 shows the hierarchical ISM molecular gas structure from cloud to clump to core in the Rosette molecular cloud (Blitz & Williams 1999). The left panel shows the bulk molecular gas traced by CO. The middle panel shows higher resolution observations of denser clumps within the molecular cloud traced by $C^{18}O$. Finally, the right panel shows individual star forming cores in the dense gas CS emission. Table 1.1 gives a list of typical values of physical parameters associated with clouds, clumps, and cores.

On the largest scales, global influences, like disk dynamics, play a role in organizing and shaping the bulk molecular gas, but only impact the ISM on kilo-parsec scales. On intermediate scales, observations show that molecular gas is organized into GMCs. These GMCs have a typical size of $\sim$ 50 pc (Solomon et al. 1979) and host virtually all star formation. From Milky Way observations, and more recent observations in nearby galaxies, GMCs tend to have universal properties which are described by the Larson Relationships (Larson 1981; Solomon et al. 1987; Hughes et al. 2010; Rebolledo et al. 2012; Donovan Meyer et al. 2013). However, recently, in the largest extragalactic GMC study has shown that GMCs vary across galactic environments (Colombo et al. 2014) and even vary from galaxy to galaxy (Hughes et al. 2013), suggesting that there may be multiple mechanisms for GMC development and evolution, however it is likely that local gravitational instabilities still regulate GMC formation.

These clouds are the sites of star formation, but stars only form from a small percentage of the total GMC mass (Enoch et al. 2007a). Within GMCs, local regions with over-densities collapse and become the sites of star formation. In the Milky Way, star formation occurs in dense clumps on $\sim$1 pc scales (Lada & Lada 2003). These clumps are coherent structures within GMCs that are denser than the mean GMC environment and are individually gravitationally bound (Williams et al. 1994) and will become the birth place of stellar clusters.

In very simplistic terms, star formation can be thought as a two stage process. The first stage being the creation of over-densities within the bulk molecular gas. This may be due to supersonic turbulence, cloud-cloud collisions, or shock associated with spiral density wave. This creates an active and inhomongeous GMC. Gravitational collapse happens in the densest regions,

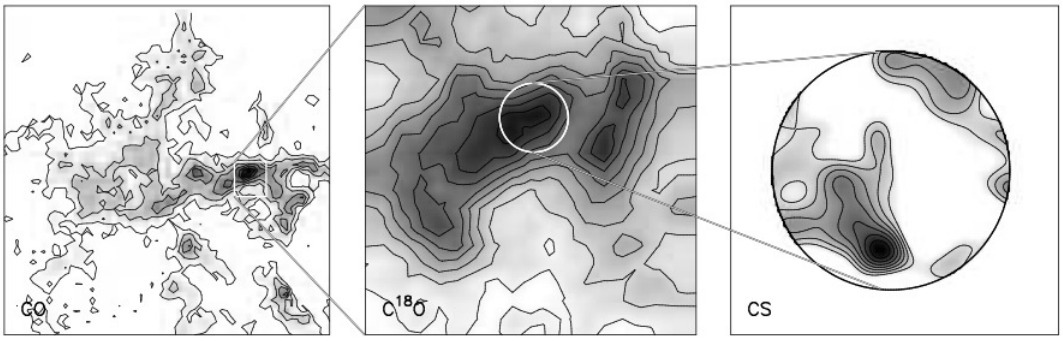

Figure 1.7 Comparison of size scales of clouds, clumps, and cores from observations. The left panel shows the bulk molecular gas traced by CO. The middle panel shows higher resolution observations of denser clumps within the molecular cloud traced by $C^{18}O$. Finally, the right panel shows individual star forming cores in the dense gas CS emission. This is Figure 4 from Blitz & Williams (1999). This image is reproduced with permission from the authors.

Table 1.1. Properties of ISM Star Forming Objects

Property	Unit	GMC	Clump	Core
Size	[pc]	10 - 100	1	0.1
Mass	[$M_\odot$]	10^5	30-10^3	3-10
Temperature	[K]	15	10	10
Density	[cm^{-3}]	300	10^4	10^5

above a critical density of 10^4 – 10^{-5} cm^{-3} (Evans et al. 2009; Heiderman et al. 2010; Lada et al. 2010, 2012). The second stage of star formation involves the creation of a protostar. The gas will eventually be blown way by the parent star via stellar feedback (i.e. winds, radiation, SNe explosion). This thesis focuses on this first stage of star formation and how it relates and is influenced by to the global dynamics.

Different physical processes effect the ISM on the various sizes scales described above. In order to provide a general picture of the various size scales related to star formation and discussed within this thesis, we describe of the two main physical processes responsible for the first stage of star formation and the relevant size scales for star formation, gravity and turbulence.

1.4.1 Gravity

Gravity plays a major role in the shaping and evolution of the ISM. Specifically, gravity is responsible for gas collapsing and the onset of star formation. A common method for determining the conditions for gravitational collapse is known as the Jeans Criterion. This is used in observations to determine if a observed regions are gravitationally bound. The derivation of this criterion is reviewed below.

Jeans Criterion

For a given a region of gas that is assumed spherical and homogenous, we can determine a criterion for which a region of gas will gravitationally collapse. This region could be a GMC, clump, or a core. This *ball* of gas has a potential energy of

$$\Omega = -\frac{3}{5}\frac{GM^2}{R}. \tag{1.4}$$

Assuming a sphere of perfect gas at a temperature T, the thermal energy associated with that cloud can be written as

$$E_{\rm therm} = \frac{3}{2}\frac{MkT}{\mu m_{\rm H}}, \tag{1.5}$$

where M is total mass of the cloud. From the virial theorem, we can obtain a criterion for stability as the total kinetic energy is equal to half of the gravitational potential, giving

$$M_{\rm sphere} > M_{\rm Jeans} = \frac{3kT}{2G\mu m_{\rm H}}R. \tag{1.6}$$

This method allows for an easy and quick criterion for collapse of a cloud, although it does not give much information on the ISM beyond the expectation of pre-existing clouds. Since this approach can be applied to any spherical volume of gas, it can be used to model GMCs, clumps, or cores of gas.

A more general approach is to consider this same instability but in a uniform, infinite medium. This can help determine the conditions for which clouds, and eventually stars will form from the ISM. We can use the following equations of an incompressible, self-gravitating, inviscid hydrodynamics to describe the dynamics of the medium with density, ρ,

$$\frac{\partial \rho}{\partial t} + \nabla \cdot \rho \mathbf{v} = 0, \tag{1.7}$$

$$\rho \left(\frac{\partial \mathbf{v}}{\partial t} + \mathbf{v} \cdot \nabla \mathbf{v} \right) = -\nabla P - \rho \nabla \Phi, \tag{1.8}$$

$$\nabla^2 \Phi = 4\pi G \rho. \tag{1.9}$$

The gas can be assumed to be isothermal and we can utilize the barotropic equation of state, $P = c_{\mathrm{s}}^2 \rho$, where c_{s} is the speed of sound. Assuming the gas begins in a state with a constant density, ρ_{o}, constant pressure, P_{o}, and is at rest (v_{o}= 0). Now, consider the following perturbations: $\rho = \rho_o + \rho_1$, $P = P_o + P_1$, $v = v_1$, and $\Phi = \Phi_{\mathrm{o}} + \Phi_1$. The quantities that correspond to the perturbations depend on both time and space and are small in comparison to the original state quantities.

By updating our dynamics equations from above and linearizing them, we obtain

$$\frac{\partial \rho_1}{\partial t} + \rho_{\mathrm{o}} \frac{\partial v_1}{\partial t} = 0, \tag{1.10}$$

$$\frac{\partial v_1}{\partial t} = -\frac{\partial \Phi_1}{\partial x} - \frac{c_{\mathrm{s}}^2}{\rho_{\mathrm{o}}} \frac{\partial \rho_1}{\partial x}, \tag{1.11}$$

$$\frac{\partial^2 \Phi_1}{\partial x^2} = 4\pi G \rho_1. \tag{1.12}$$

These can be simplified to,

$$\frac{\partial^2 \rho_1}{\partial t^2} = \rho_o \frac{\partial^2 \Phi_1}{\partial x^2} + c_s^2 \frac{\partial^2 \rho_1}{\partial x^2}. \tag{1.13}$$

If the perturbations are periodic, such that $\rho_1 = Ke^{i(kx+wt)}$, the following conditions must hold:

$$w^2 = k^2 c_{\mathrm{s}}^2 - 4\pi G \rho_{\mathrm{o}}. \tag{1.14}$$

There are unstable modes when $w^2 < 0$ and w is imaginary. Specifically those wave numbers, k, where

$$k < k_{\rm Jeans} = \left(\frac{4\pi G \rho_{\rm o}}{c_{\rm s}^2} \right)^{1/2} \tag{1.15}$$

are unstable. The characteristic point where they become unstable is the basis for the Jeans criterion. Specifically, a length scale can be defined as $\lambda_{\rm Jeans} = 2\pi/k_{\rm Jeans}$. Likewise, mass enclosed within a cube of size $\lambda_{\rm Jeans}$, becomes Jeans mass, $M_{\rm Jeans} = \rho(2\pi/k_{\rm Jeans})^3$. In terms of physical quantities, these can be rewritten as

$$\lambda_{\rm Jeans}^2 = \frac{\pi c_{\rm s}^2}{G\rho_{\rm o}} \tag{1.16}$$

$$M_{\rm Jeans} = 2.92 \frac{c_{\rm s}^3}{G^{3/2}\rho_{\rm o}^{1/2}} \tag{1.17}$$

Scales larger than the Jeans length and mass are unstable to gravitational collapse.

Considering the various elements involved in star formation, we can determine the Jeans length and mass for a GMC, clump, and dense cores for the typical values listed in Table 1.1. For a GMC, the Jeans length is 4 pc and the Jeans mass is 600 $M_\odot$. For dense cores, the Jeans length is 0.15 pc and the Jeans mass is 30 $M_\odot$. These size scales are similar to the substructure seen within local GMCs between clumps and cores.

1.4.2 Turbulence

One of the main drivers of the ISM is turbulence. It plays an important role in shaping and influencing the ISM through helping energy cascade from large scales down to smaller scales. Turbulence couples ISM features over four orders of magnitude of size. Here, we review the basic background of turbulence and explain how to relates the scales of star formation.

Turbulence in the ISM was thought to be generated by supernova explosions (Spitzer 1978). More recently, additional drivers of turbulence have been suggested: swing amplification (Wada 2008), large scale galactic accretion(Klessen & Hennebelle 2010), magnetorotation (Sellwood & Balbus 1999) and additional types of stellar feedback (ie. radiation or winds). Turbulence

requires a driving mechanism or it will decay quickly (Mac Low et al. 1998). The driving energy source and corresponding scales are still being debated.

Turbulence occurs because hydrodynamics flows are described by the Navier-Stokes Equation which is non-linear in nature. The Navier-Stokes Equation for an incompressible, viscous, fluid is written as

$$\rho\left(\frac{\partial v}{\partial t} + v\cdot\nabla v\right) = -\nabla P + F + \rho\nu\nabla^2 v \tag{1.18}$$

Turbulence can be considered as an energy cascade (Richardson 1920; Kolmogorov 1941), where eddy instabilities form smaller eddies. The energy in the largest eddies get moved down to smaller eddies. In the ISM, this will continue until the self gravity associated with the eddy over powers the ability to form smaller eddies. There is a transfer of energy from the scale at which energy is input into the system down to the the scale where energy dissipates, $k^{-5/3}$ (Kolmogorov 1941). Turbulence is driven on cloud size scales and is dissipated on core and protostar size scales.

1.5 Molecules in Space

1.5.1 Excitation of Molecule Emission in the ISM

Millimeter and radio observations are commonly utilized to study the ISM because many atomic and molecular emission lines are present at these wavelengths. These emission lines can be used to probe the physical conditions in the ISM. Molecules have three transitions: electronic, vibrational, and rotational. At radio and more specifically, millimeter wavelengths, rotational transitions dominate. The rotational transitions are the quantizations of the energy required for the molecules to rotate. These energies correspond to meV or a temperature of $\sim$ 10 K, similar to the thermal temperature of GMCs.

Rotational Spectra of Diatomic Molecules

Assuming a rigid diatomic molecule, the rotational energy can be written in terms of it's moment if inertia, I, and the angular momentum, J, as

$$H_{\rm rot} = \frac{1}{2}I\omega^2 = \vec{J}^2/2I. \tag{1.19}$$

The moment of inertia for a diatomic atomic with two atoms, A and B, with a distance of R is

$$I = m_{\rm r} R^2 \, , \text{where } m_{\rm r} = \frac{m_{\rm A} m_{\rm B}}{m_{\rm A} + m_{\rm B}}. \tag{1.20}$$

The Schrödinger equation for this system yields energy values of

$$E_{\rm rot} = \frac{J(J+1)\bar{h}^2}{2I}. \tag{1.21}$$

In order for radiative emission from a dipole rotational transitions we need $\Delta J \pm 1$. An emitted photon would have an energy of

$$\nu = \frac{\Delta E_{\rm rot}}{h} = \frac{\bar{h}^2}{2I}[J(J+1) - J(J-1)] = \frac{\bar{h}^2 J}{2\pi I}, \tag{1.22}$$

going from J to $J-1$, where J corresponds to the upper energy level quantum number.

Using Molecules to probe physical conditions within the gas

These molecules require certain physical conditions to be excited and emit at these rotational energies. Specially the temperature of the gas and the density of the gas will determine if a molecule is excited. For gas in Local Thermodynamics Equilibrium (LTE), the relative level population, n_i^* within a molecule can be expresses in terms of the Boltzmann Equations:

$$\frac{n_{\rm u}^*}{n_{\rm l}^*} = \frac{g_{\rm u}}{g_{\rm l}} e^{-\Delta E_{\rm ul}/kT} \tag{1.23}$$

where kinetic temperature of the system is represented by T, and g_i is the statistical weight of the ith energy level. The number densities are set by the physical state of the gas, in LTE the distribution of excitation states gives the rates of emission and absorption, specifically the spontaneous emission, stimulated emission, and absorption where all excitation temperatures are the same. However, the assumption of LTE is not required and different excitation temperatures could set the population of the different levels.

Considering that molecules are excited by collisions in the gas, the temperature needs to be above a certain threshold for collisional excitation of these rotational transitions. This temperature is roughly, $T \sim E_{\rm rot}/k$. So

the average minimum temperature required for a specific transitions can be written as

$$T_{\rm min} \approx \frac{\nu h(J+1)}{2k}. \tag{1.24}$$

Density of the gas also influences the chance of collisional excitation. To determine when emissions occurs, we consider the Einstein probability of spontaneous emission coefficient

$$A_{\rm ul} = \frac{64\pi^4}{3hc^3}\nu^3|\mu_{\rm ul}|^2 \tag{1.25}$$

where $\mu_{\rm ul}$ is the dipole moment matrix of the transitions. For a transition from $J+1 \rightarrow J$ the spontaneous emission coefficient can be rewritten as

$$A_{\rm ul} = 1.165 \times 10^{-11}\mu^2\nu^3\frac{J+1}{2J+3}. \tag{1.26}$$

The spontaneous emission rate must equal the rate at which radiating molecules collide and are excited. The higher the spontaneous emission rate, the larger the density of the gas must be in order for collisional excitation. This critical density can be written as

$$n_{\rm crit} = \frac{A_{\rm ul}}{\sigma\nu}. \tag{1.27}$$

There are more rigorous ways to determine the exact densities and temperature present in the ISM, specifically by looking at multiple transitions of the same molecule, but this can be thought of as a good approximation for a quick estimate of the density and temperature within the ISM.

1.5.2 Large Velocity Gradient Analysis

A common technique for modeling the physical conditions within the ISM is the Large Velocity Gradient (LVG) approximation, which allows for an estimate of the physical properties of the molecular gas. This approximation was developed for millimeter lines by Goldreich & Kwan (1974) and Scoville & Solomon (1974). The LVG approximation assumes the region of the ISM has a large velocity gradient along the line of sight that is larger than the thermal line width. The large velocity width is caused by a global collapse or expansion of the region. For a given frequency within the spectral line, that emission is coming from a small part of the region along the line of sight.

This means that photons only interact with molecules that are located in a small localized region around which the photons are emitted.

Across the entire region, the velocity gradient, density, kinetic temperature, and excitation temperature are assumed to be the same. Radiative transfer equations and statistical equilibrium are solved simultaneously. For an optically thick region, the probability an emitted photon will escape the region without being reabsorbed is also required. Four independent physical parameters are required for the LVG analysis: kinetic temperature, T_{kin}, gas density, n, molecular abundance, and the velocity gradient which describes the turbulent line width. These parameters will result in different excitation conditions within the gas. The LVG approximation is a common technique used to probe the physical properties of molecular gas and will be used later in this thesis.

1.5.3 H_2 and CO

Two main reasons for studying molecular gas in nearby galaxies are (1) the ISM is composed mainly of H_2 in the disk of galaxies (Scoville 1990) and (2) stars are born within clouds of molecular gas (Blitz 1993). Most of the gas in molecular clouds is in the form of molecular hydrogen, H_2. As a homonuclear molecule, H_2 has no permanent dipole moment and does no emit millimeter rotational emission lines. H_2 can be directly observed through absorption in the far-UV or via emission at infrared. UV absorption by H_2 molecules can be seen in the line of sight to nearby stars in electronic transitions, however finding lines of sight with background sources for specific regions is difficult. H_2 emission at infrared wavelengths come from rotational-vibration transitions in warm (2000 K) regions, associated with shocks and outflows from nearby stars. Neither of these allow a simple probe of the cold dense pre-star forming ISM gas. Instead, CO[2] has become the dominant tracer of the molecular ISM and used a a probe of the H_2 gas.

CO is commonly used to trace the total molecular gas. CO has been found to be a good tracer of the total molecular gas mass of Milky Way through empirical relationships between virialized GMC mass and CO luminosity (Dame et al. 1986; Solomon et al. 1987) and the general distribution of diatomic hydrogen (Young & Scoville 1991a; Young & Devereux 1991), despite only representing $\sim 10^{-4}$ of that of H_2. CO emission traces areas

[2]Hereafter, use of CO refers to ^{12}CO (J=1-0, at 115 GHz)

with higher density than neutral hydrogen (HI) since higher densities are required for collisional excitation. A conversion factor, $X_{\rm CO}$ is commonly used to determine the total amount of H_2 from observations of CO. Values of $X_{\rm CO}$ typically range between 2-3 x 10^{20} cm^{-2} (Solomon et al. 1987). There is some evidence that $X_{\rm CO}$ could vary due to environmental factors like metallically or galaxy type (Leroy et al. 2007; Blitz et al. 2007). Due to the relative ease of observing CO and its association with the bulk molecular gas, CO still remains the best way to study the H_2 present in the ISM.

1.5.4 HCN and HCO+

Observing emission lines from molecules that require higher densities or temperatures for excitation can probe the denser components of the ISM. Dense gas only represents a small percentage of the total GMC mass (Enoch et al. 2007a) as traced by CO. Since stars form from this dense component of the ISM, using denser (and/or warmer) tracers of the ISM allows us to study the intermediate stages of gas evolution in the ISM. Specifically, looking at denser gas along spiral arms can allow us to study how the spiral arm environment leads to the creation and evolution of dense star forming component of the ISM.

Tracing molecules, like HCN (J=1-0, 88.6 GHz) or HCO+ (J=1-0, 89.1 GHz), which require higher densities to be excited, can be used to observe the gas in the dense cores from which stars form. Due to its higher dipole moment, $\mu \sim 3\ D$, higher densities are required for collisional excitation compared to the dipole moment of CO, $\mu \sim 0.1D$. The critical density for excitation of HCN is of the order of $n > 10^4$cm^{-3}. This is much larger than the density required to excite CO, $n \sim 500$ cm^{-3}. These dense gas emissions only come from regions with high volume density, typically $n > 10^4$ cm^{-3} as seen in Milky Way observations of nearby clouds (Lada 1992; Lada et al. 2012).

From local observations of Milky Way molecular clouds, Heiderman et al. (2010) identified regions with high extinction and evidence of recent star formation and found that the HCN is correlated with star formation in this region. Thus HCN appears to be tracing a denser component within the bulk molecular cloud environment. These regions of high dust extinction within molecular clouds are the sites of recent star formation (Lada et al. 2010). HCN observations in the Milky Way are tracing the dense gas within GMCs. This implies that dense gas tracers, like HCN and HCO+, selectively trace

gas most relevant for star formation with the larger GMC environment.

From extragalactic observations, a close correlation was seen between dense molecular gas and massive star formation in the centers of galaxies (Nguyen et al. 1992a). These observations show that HCN has a linear correlation with infrared (IR) luminosities, a tracer of star formation, whereas, the CO has a super linear relationships. In addition, starburst galaxies may deviate from the CO-IR relationship with an excess of IR luminosity (Gao & Solomon 2004b). Figure 1.8 shows the relationships between HCN and IR luminosity and also CO and IR luminosity. The HCN-IR relationship is tighter than the CO-IR relationship. In addition, the CO-IR relationship may not be able to be explained in a single correlation for both of these classes of galaxies (Gao & Solomon 2004b).

A close relationship between dense molecular gas tracers is seen in nearby galaxies and in also in Milky Way GMC clumps. These are two extremely different size scales and suggest that HCN can probe dense gas without requiring the angular resolution associated with the dense regions. Since HCN allows for the selection of only the dense star forming gas, we can selectively trace the denser regions within a GMC. This is further confirmed with the work of Wu et al. (2005, 2010). The tight linear correlation between HCN and star formation, traced by IR, is not only present in distant galaxies as seen in Gao & Solomon (2004b), but it has also been shown to expand down to Milky Way size scales (Wu et al. 2005), as seen in Figure 1.9 and in follow up work by Graciá-Carpio et al. (2008); García-Burillo et al. (2012); Foster et al. (2011); Kepley et al. (2014); Usero et al. (2015a). The cause of the correlation has been suggested by Wu et al. (2005) to be caused if HCN traces a 'basic unit' of massive clustered star formation. This would link the stages of star formation on different scales and environments. In this picture, HCN emission selectively traces the dense star-forming cores even when they are not spatially resolved and these cores are all at a size for which they will form a stellar cluster. This conjecture provides a more complete picture linking HCN to the evolution of gas into stars. HCN and other high-density gas observations provide a key advantage in studying star formation in clumps in nearby galaxies even without the angular resolution to spatially resolve these clumps in nearby galaxies.

In Chapter 4, we focus on the formation of dense gas in the spiral arms of the disk of M51 by studying HCN and HCO+ emission. We aim to discuss the role of dense gas emission in the evolutionary sequence of gas along the spiral arms in M51. We do this through new observations of the $\sim$kpc scale

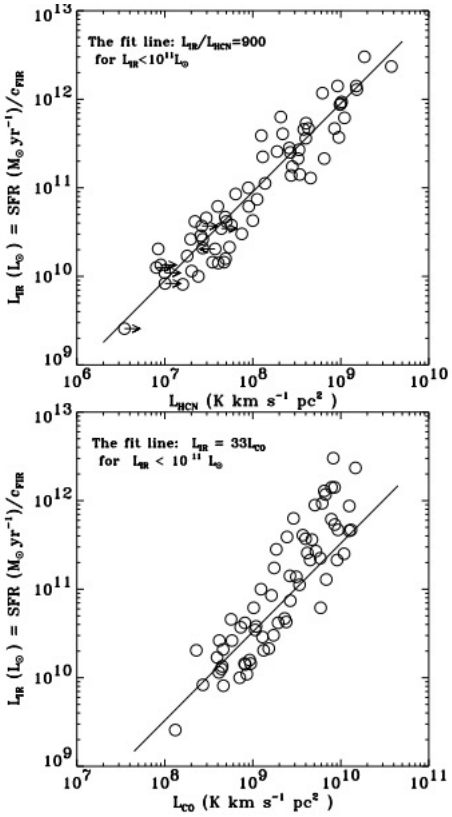

Figure 1.8 Correlation between HCN luminosity and star formation, which is traced by IR luminosity. A linear relation with a slope of 1 is seen between HCN and star formation, where as the correlation between CO and star formation is superlinear. In addition, the largest CO values deviate from the superlinear fit. This is Figure 1 from Gao & Solomon (2004b). This image is reproduced with permission from the AAS.

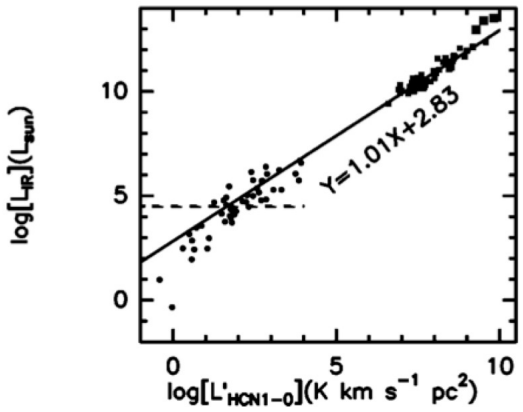

Figure 1.9 L_{HCN} to L_{IR} correlation for Galactic and extragalactic sources. This correlation spans over 7-8 orders of magnitude. This correlation suggests that there is a basic unit that can measure star formation based on the dense cores both in our galaxy and in extragalactic sources. This is Figure 1 from Wu et al. (2005). This image is reproduced with permission from the AAS.

dense gas distribution across the disk and also localized along spiral arm on 100 pc scales and its connection to the bulk molecular gas and recent star formation.

Chapter 2

Observational Techniques

In this chapter we introduce various concepts related millimeter single dish observations and interferometry observations which are used intensively for this thesis. The main results in Chapter 4 rely on data obtained via interferometric and single dish observing techniques. This chapter also serves to introduce and describe the collection and reduction of this data.

2.1 Observations of Global Distribution of Dense Gas with Green Bank Telescope

We perform a 3′x3′ on-the-fly (OTF) map of the central region of M51 in HCN and HCO+ both in the J=1-0 transitions. This area includes the spiral arms, interarm regions, and central nucleus. The yellow square shown in Figure 4.2, shows the area our observations mapped. Our observations took place between March 2013 and January 2014, on-site at the Green Bank Observatory, and remotely at Stony Brook.

2.1.1 Observations at Green Bank Observatory

In order to obtain these mm-observations, we used the Green Bank Telescope (GBT) at the National Radio Astronomy Observatory Green Bank location in West Virginia. The GBT is a 100m fully steerable dish that is able to observe at frequencies between 0.1 - 116 GHz. In addition to its large collecting area, the GBT dish is covered with adjustable panels to optimize performance.

The GBT is located within the National Radio Quiet Zone to limit radio frequency interference signals in the region.

Using the newly developed GBT W-band receiver, we produced a HCN and HCO+ map of the central region of M51. The W-band receiver saw first light in May 2011 and became available for public shared-risk time in 2013. The W-band receiver is able to observe between 67 - 93 GHz. The receiver is a Gregorian receiver with dual beam and dual polarization. The beams are separated by $4.8'$. The IF system for the receiver is broken into four separate filter bands each covering $\sim$ 7 GHz. Our observations utilize the FL4 filter covering 85-93 GHz.

The W-band receiver is unique to the other GBT receivers in that it does not have a noise diode. A calibration wheel is positioned within the W-band receiver to allow for necessary calibrations. Specifically, the calibration wheel contains a 'warm' and 'cold' load. The cold load temperature is set by the system and by recording the ambient temperature throughout the observations. These two loads allow for system voltages to be converted into system temperatures.

The backend Spectrometer on the GBT allows for a range of spectral line observations. The spectrometer provides wide (800, 200 MHz) and narrow (50, 12.5 MHz) resolutions. In addition to the Spectrometer, additional backends available for GBT observations can take continuum observations using either the Caltech Continuum Backend or the Digital Continuum Receiver. Since the observations described in this section have been taken, the VEGAS: Versatile GBT Astronomical Spectrometer is now used for spectral line observations.

All observations at the GBT are scheduled via the Dynamic Scheduling System (DSS). This system schedules projects for observations that optimize the required observing conditions for the large range of frequencies covered by the GBT and the ranking of observing priority for the projects. Some frequencies require observations at night when the sky is very calm and clear, where as, other projects can be scheduled regardless of the weather and time of day. There is an exception that when snow is accumulating on the dish or the winds are strong, observations are stopped for the safety of the equipment. The DSS schedules projects 24 - 48 hours in advance to try to maximize GBT functionality.

Observations were performed in the 2013A and 2013B semester. A detailed table of our observations can be found in Table 4. We will obtain data for first excitation transition for both HCN and HCO+ in both XX and

YY polarization. We only utilize one of the beams in our mapping due to the large spacing between the beams compared to our mapping area. The spectra were centered at 475 km s^{-1}, the LSR radio velocity of M51.

2.1.2 On-the-Fly Mapping Technique

These observations utilized the On-the-Fly (OTF) mapping procedure. The goal of OTF mapping is to map a large area quickly to avoid changes in atmospheric and instrumental fluctuations to minimize calibration overhead. For a more detailed review of OTF mapping, see Mangum et al. (2000).

In OTF mapping, spectral line data are taken continuously and in quick repetition while the telescope moves across the target or region being mapped. Over short intervals the data are 'dumped' and saved as a single spectrum. The locations where the data were collected between dumps are recored. At the start of the observations a reference scan is taken, which is typically longer than the scanning sampling rate, then data are collected while scanning in a given direction. At the end of the scan another reference scan is taken. This is done until the entire area is sampled. Typically scans are also taken in the perpendicular direction. Due to the short on-source integration time, the entire image plane can be sampled very quickly. At each position the S/N ratio will be very low, but the process is repeated many times. With respect to the beam, there is a maximum sampling interval required, $\lambda/2D$, where D is the maximum dimension of the antenna. This ensures that all of the spatial frequencies associated with the disk are detected. This corresponds to $\sim$3 pointing per full width half maximum (FWHM) of the dish. The data is sampled at the Nyquest sampling rate. The OTF method is very accurate because the spectra are oversampled and the rapid sampling results in minimal changes in the weather conditions effecting the final calibration. A final image is produced by placing the spectra on a grid and averaging the overlapping spectra on the gridded map.

2.1.3 Observing Procedure

The typical observing procedure went as follows:

- Dish surface corrections : The active surface of the GBT can be adjusted for thermal corrections. A nearby bright point source, typically a quasar, is observed and the shape of the dish is adjusted to optimize

observations. This was performed every three to four hours of observations. This improves both the observing beam size and the aperture efficiency.

- Pointing and focusing : Correction of telescope pointing and focus is done using a bright quasar. This step should be performed every hour. Scans are performed to correct for small misalignments between the pointing of the telescope and the future location of a star in the sky. This is done by scanning in both in Right Ascension (RA) and Declination (Dec) directions. After adjustments are made to align the source, the focus is set to find where the flux is most concentrated by varying the distance between the receiver and the dish.

- Flux calibration measurement: Typically preformed using the same quasar source from point and focus, observations of a quasar with a known flux allows for a conversion between instrumental voltages and flux. A simple on and off integration was taken. These observations allow for a calculation of the aperture efficiency and the main beam efficiency.

- Mapping: Utilizing the OTF capabilities of the GBT, 7 kpc around the center of M51. The galaxy is mapped both along the RA and Dec directions. During a single mapping sequence observations are preformed either scanning back and forth across the RA plane or the Dec plane. A full strip is made in either the positive or negative direction per scan. The speed at which that telescope scans across the mapping regions is set such that 4 seconds of integration are performed per resolution element in the mapping of the source target. Between each observed strip, a reference point was observed for 15 seconds of integration. An additional 20 seconds of overhead scan time was included for the telescope to slew from the mapping area to the reference point area. In total 22 strips were preformed to cover the galaxy for full beam sampling. The total time for one OTF mapping took 56 minutes. This provided a good duty cycle between point and focusing corrections that needed to be performed between each mapping.

  A schematic representation of the mapping technique is shown in Figure 2.1. Observation of a single row or scan begins in an 'OFF' position, represented here as the left circle in the position labeled 'OFF'. Next

the telescope moves to the edge of the mapping area and collects data in very short integrations while scanning across the mapping area (green path). Once the map reached the end of the mapping strip it moved to the right most off positions. After data is collected it begins to observe the next strip along the next row of the map (red path). This continues across the full map.

We utilized the RaLongMap and DecLatMap standard observing modes to aid in the execution of this observing scheme. These standard observing modes do not take into account separate reference or 'OFF' integration points. Our observing script was created in order to allow for a single strip to be observed with the two different reference images to be observed before and after the strip. The RaLongMap and DecLatMap modes were used for the data collection of a single strip but the Track command was used to observe the reference points between the scans.

In total we used four different mapping sequences. Two mapping sequences in the RA direction and two mapping sequences in the Dec direction. The strips were separated by the $10''$ resolving beam in an individual observing sequence and each of the same orientation set of mapping sequences were offset by $5''$, half the size of the resolving beam of the GBT. The location of our mapping sequences can be seen in Table 2.1.

- Flux calibration measurement: Repeat flux calibration measurement from above to characterize variations in aperture efficiency.

This observing sequence is repeated a number of times within the GBT observing client CLEO. This software, developed by the GBT staff, allows for control of the GBT system both on-site and remotely. Observing scripts for various stages of the data collection are written and submitted into a queue. The telescope is controlled via the procedures submitted by the observer and will move through the queue, notifying the observer of any issues while executing the commands. In addition, this software allows the observer to watch the status of the various systems associated with the telescope hardware, the receiver, the sky conditions, and communicates with the telescope operator. This last item becomes useful when observing remotely, in the event of weather or instrumentation problems. CLEO also allows the user to

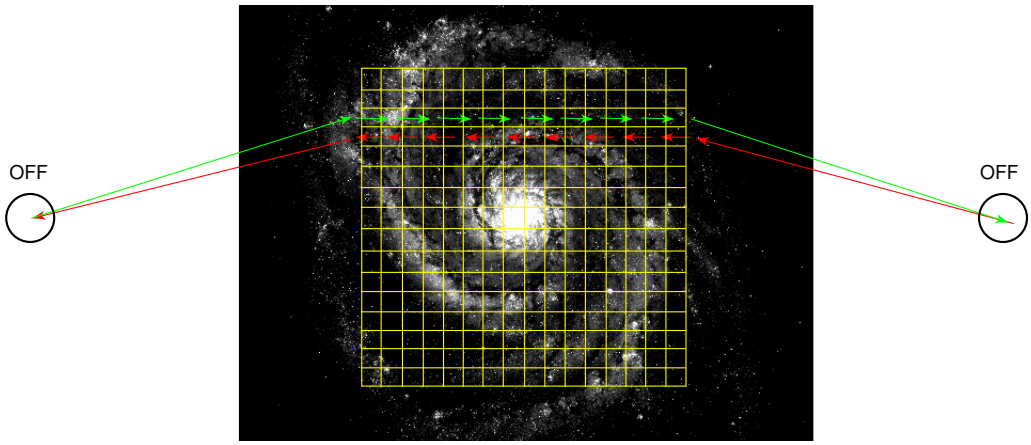

Figure 2.1 A schematic representation of the OTF mapping technique used for the RALongMap. This image is not to scale but is only meant to be representative of the mapping process.

watch data as it is taken and verify that the derived pointing and focusing solutions are correct.

2.1.4 GBT Data Reduction

The spectra data collected at the GBT was reduced using the package GBTIDL[1]. This software allows for viewing, manipulating, fitting, and comparing spectral line data taken with the GBT. For every mapping sequence, we generated spectra for both HCN and HCO+ lines, in both XX and YY polarization. For every integration, four unique spectra were obtained. Each of these spectra will need to be reduced. Reduction scripts were written in GBTIDL to perform the various calibration steps. The following outlines the overall reduction steps that were applied to the spectra.

One feature of the GBT that allows for proper reduction of the data is the 4mm calibration wheel. As discussed previously, this wheel contains six observing positions. The important locations on the wheel for our observations are the sky positions and also the warm and cold loads. These allows for a conversion of the instrumental voltages into antenna temperatures. Specifi-

[1]http://gbtidl.nrao.edu/

Table 2.1. M51 GBT Mapping Pointing

Location	RA	Dec
Image Center	13:29:52.71	+47:11:42.5
RA1 Map	13:29:52.71	+47:11:45.0
RA2 Map	13:29:52.71	+47:11:40.0
Dec1Map	13:29:52.95	+47:11:42.5
Dec2 Map	13:29:52.47	+47:11:42.5
Left Offset	13:30:30.0	+47:11:42.5
Right Offset	13:29:20.0	+47:11:42.5
Top Offset	13:29:52.71	+47:18:00.0
Bottom Offset	13:29:52.71	+47:05:00.0

cally this determined the gain:

$$g = [T_{\rm warm} - T_{\rm cold}]/(V_{\rm warm} - V_{\rm cold}). \tag{2.1}$$

The cold load temperature is set within the receiver and the ambient/warm temperature is recorded throughout the observations. The main beam temperature, $T_{\rm mb}$ is related to the observed antenna temperature, $T_{\rm a}$, using the main-beam efficiency, $\eta_{\rm mb}$,

$$T_{\rm mb} = T_{\rm a} \exp(\tau_{\rm o} A)/\eta_{\rm mb}, \tag{2.2}$$

$$n_{\rm mb} = 0.8899 \eta_{\rm a} (\Theta_{\rm FWHM} D/\lambda)^2, \tag{2.3}$$

where τ is the zenith opacity and A is the airmass. For the GBT, $\eta_{\rm a}$ can be determined using the flux density, S_ν, of a known source,

$$\eta_{\rm a} = 0.3516 T_{\rm a} \exp(\tau_{\rm o} A)/S_\nu. \tag{2.4}$$

From our observations of the quasars using the flux calibration measurements, we are able to determine $\eta_{\rm a}$ using CARMA CALFind[2]. CALFind keep a record of the historical fluxes of the brightest quasars. Using the determined gains and A at time of observations, and the measured sky opacity along

[2]http://carma.astro.umd.edu/cgi-bin/calfind.cgi

with the antennas efficiencies, we can reduce the scans and generate our map of M51.

During our mapping observing procedure, we took two different sets of scans: an on-source scan and an off-source scan. Every 'row' of on-source scans begins and ends with an off-source scan. The two off-source scans are averaged and become the master off-source scan for each row. This master off-source scan is used to correct for the sky during observations, this includes atmospheric and other non-source emission. To determine the true on-source emission we need to remove the off-source emission or sky emission,

$$T_{\rm a} = T_{\rm sys}(V_{\rm on} - V_{\rm off})/(V_{\rm off}) \tag{2.5}$$

where $T_{\rm sys} = gV_{\rm off}$. In addition, we perform a baseline subtraction to adjust for any offset from zero. To do this, the edge ranges of our spectra are fit between 88.43 - 88.44 GHz and 88.54 - 88.55 GHz, which is a range outside the line profile of the galaxy. A single first order polynomial is subtracted from the final off-source subtracted spectra. Using $\eta_{\rm mb}$, A, and τ we can put our spectra in $T_{\rm mb}$ units. Figures 2.2 and 2.3 show spectra presented in GBTIDL for a raw scan and a reduced scan, respectively. The data is of the same source and is representative of the individual scans taken.

Once all of the individual on-source spectra are calibrated and in $\rm T_{mb}$ units we utilize the GBT Mapping Pipeline. The Pipeline reads in all the spectra data than maps the data by gridding the individual spectra onto a compete data cube, where each spectra channel becomes an individual slice of a final position-position-velocity 3D array. Each pixel on the position-position surface will have a unique spectra. A map was generated from each mapping sequence to check the consistency between individual OTF maps.

To create a final map, the basket-weave algorithm was used to remove systematic noise generated from the scanning direction. This method was described by Emerson & Graeve (1988) and suggests the 'scanning effect' noise can be removed by Fourier transforming the maps, masking the scan noise in the Fourier domain, and inverse Fourier transforming the maps. In order to use the basket-weave technique, our RA and Dec spectra are mapped separately. Our maps are input into the Nobeyama *nostar* software package basket-weave algorithm which is based on Emerson & Graeve (1988). Within the program, the RA and Dec maps are Fourier transformed and a mask is applied along the smallest frequencies, which correspond to the noise along the scan direction. A representative single position-position array is shown

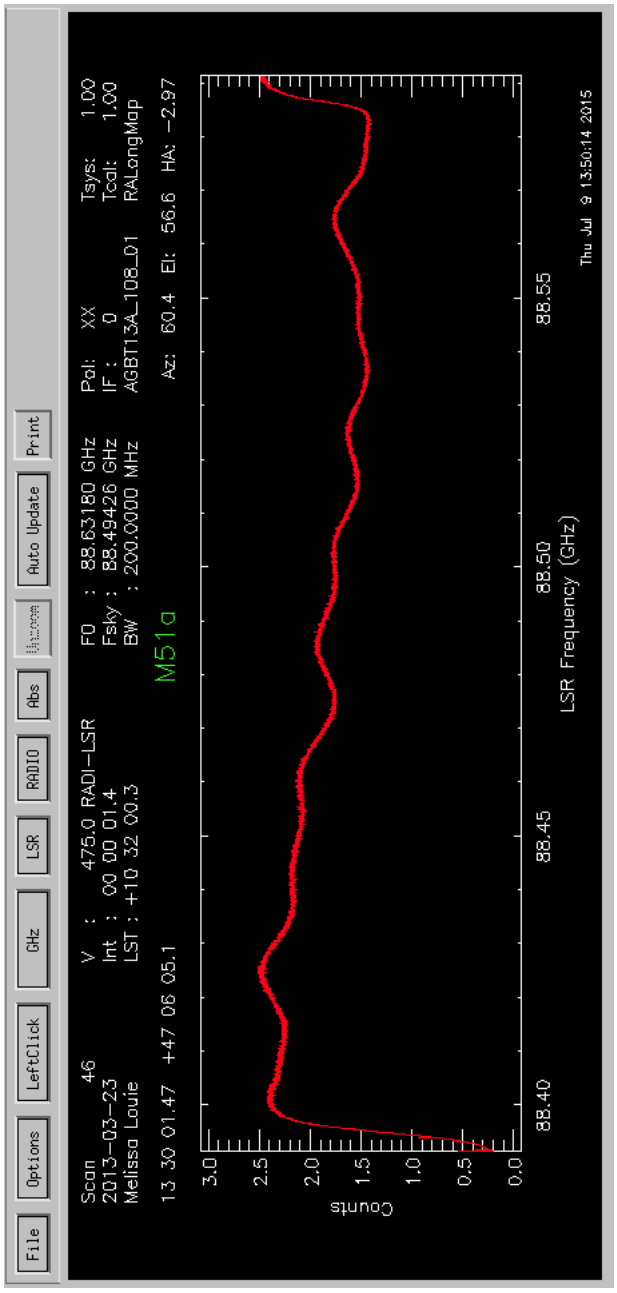

Figure 2.2 GBTIDL display of a single raw mapping scan from the 2013-03-23 observing session of HCN in the XX polarization.

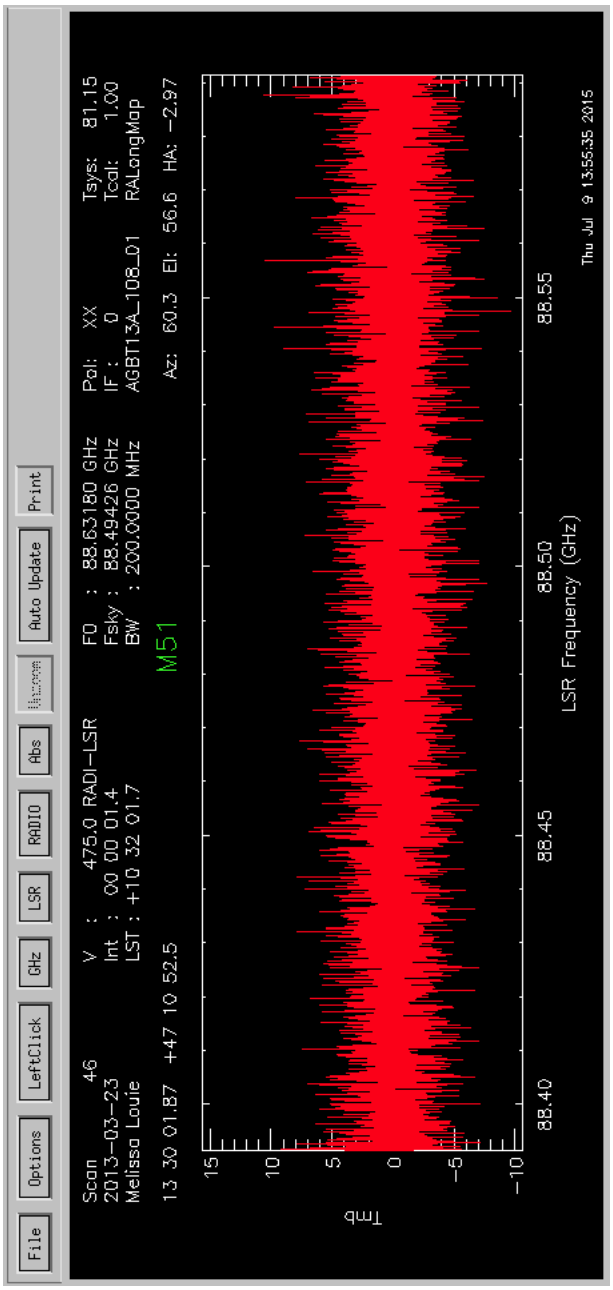

Figure 2.3 GBTIDL display of a single reduced mapping scan from the 2013-03-23 observing session of HCN in the XX polarization. This is the fully reduced scan of the raw image presented in Figure 2.2.

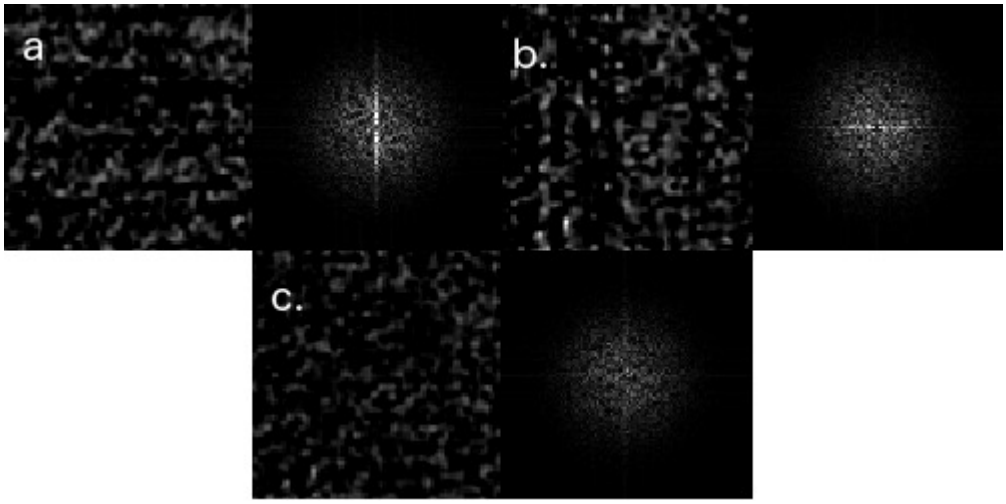

Figure 2.4 (Top) Sample RA (a) and Sample Dec (b) maps prior to basket weave and the corresponding Fourier transform. (Bottom) Final combined map and its Fourier transform. The noise created from the scan direction appears in the maps appears are perpendicular noise in Fourier space. This noise is masked out for creation of the final combined map.

on the left and the Fourier transform is shown on the right of Figure 2.4 for the HCN map. There is an increased amount of noise perpendicular to the scan direction and this can be seen in Figure 2.4 in the left panels the two top figures. Once the cut has been applied, the RA and Dec maps are combined and transformed back to real space. The final map and its Fourier transform are shown on the bottom of Figure 2.4c.

The reduction and imaging procedures explained above were shown with HCN data but the reduction and imaging of the HCO+ data followed the same procedure. These final maps are presented and analyzed in Chapter 4.

2.2 High Resolution Observation of Distribution of Dense Gas Along Spiral Arm with CARMA

We performed high resolution mapping of HCN and HCO+ emission along the western spiral arm in M51 with the Combined Array for Research In

Millimeter-wave Astronomy (CARMA) for this thesis. Data was collected in the CARMA D array configuration in December 2013. These maps were combined with previous Owens Valley Radio Observatory (OVRO) and CARMA C array data.

2.2.1 Millimeter interferometry

Millimeter wave interferometers like OVRO, CARMA, Nobeyama Millimeter Array, Plateau de Bure, and ALMA are essential for high resolution mapping observations of dense gas in nearby galaxies (Regan et al. 2001; Koda et al. 2009; Schinnerer et al. 2013). Interferometers allow for higher spatial resolution than single-dish telescope since spatially resolving sources in nearby galaxies with a single-dish telescope is nearly impossible, particularly at the long wavelengths required for millimeter wave observations.

The angular resolution that can be observed is proportional to the wavelength and indirectly proportional to the size of the telescope. The Rayleigh criterion states,

$$\theta \sim \frac{\lambda}{D} \tag{2.6}$$

where θ (radians), is the angular resolution, D (meters) is the diameter of the telescope, and λ (meters) is the observing wavelength. The Rayleigh criterion determines what angular resolution a telescope has at a given frequency. For millimeter observations $\lambda = 2.99\times10^{-3}$ m for CO (J=1-0). The leading single dish millimeter antennas have sizes in the range of tens of meters, Institut de Radioastronomie Millimtrique 30m and Nobeyama 45m, some as large as the Green Bank Telescope 100 m. Considering $D = 40$ m, the expected angular resolution of CO is around $15''$. With that resolution, one would be able to resolve $\sim$ 800 pc in a nearby galaxy 10 Mpc away. At these scales, large scale galactic structure can be studied, however, it does not provide high enough resolution to resolve smaller scales, such as GMC scale physics. In order to reach GMC scales of 100 pc, it requires an observing dish with a size of 300 m. To explore GMC structure at 1 pc scale requires a dish with a diameter of 30 km. These scales are far beyond engineering capabilities for a fully steerable dish. In this thesis, we utilize interferometric observations to observe at small angular resolution, $\sim 5''$ (200 pc at 8.2 Mpc).

Interferometry combines the light coherently from multiple spatially separated apertures. The result is an interference pattern called fringes, not an image as is obtained in typical CCD based astronomy. The advantage

of interferometry is that the maximum distance between apertures sets the angular resolution. For example, two antennas separated by 250 m yields an angular resolution of $2''$ for CO. Therefore, millimeter interferometers can easily provide spatial resolution from tens of arcseconds to subarcsecond resolution. With the increase in angular resolution, there is a decrease in sensitivity since with an interferometer only a small fraction of the total area that would be sample by a single dish with diameter D is covered by two smaller apertures with diameter d but separated by distance D.

The smallest separation between apertures creates a limitation for interferometers. Interferometers are not sensitive to angular scales less than $\sim \lambda/d_{\rm min}$, where $d_{\rm min}$ is the smallest spacing between antennas. Therefore the lowest spatial frequencies are not able to be measured, resulting in large-scale structure not begin recovered and the total flux can not be directly measured. Since there is always a finite distance between antenna positions in an interferometer, the total flux or zeroth spacing, V(0,0), can never be measured. In order to obtain this zeroth spacing data, many interferometric data sets are combined with single dish observations. This allows for the high resolution mapping with interferometers while having the total flux data only obtained via single disk observations. This technique is used in our ongoing CANON survey[3].

The interference pattern is the complex visibility pattern, V(u,v), and it is the 2D Fourier transform of T(x,y), the brightness of the source. The visibility provides information on the spacial frequencies associated with the source and an interferometer measures the spacial frequencies corresponding to the spacing between antennas. A schematic representation of the image plane and UV plane is shown in Figure 2.5.

$$V(u,v) = \iint T(x,y)\exp(2\pi i(ux+vy))dxdy \quad (2.7)$$

$$T(x,y) = \iint V(x,y)\exp(-2\pi i(ux+vy))dudv \quad (2.8)$$

The visibility is a complex quantity, where the phase gives information on location of a component and the amplitude gives information on the intensity of the component.

Interferometric arrays sample the UV plane discretely, therefore V(u,v) is measured on a specific number of points. To improve UV coverage for

[3]A survey overview is discussed in §A, along with a summary of the contributions of the author to the CANON survey.

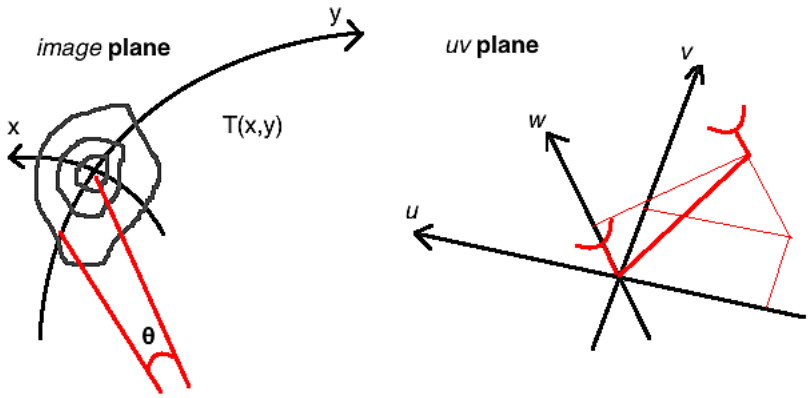

Figure 2.5 Schematic representation of the image plane and the UV plane.

better image quality requires increasing the number of antennas used to sample the sky and/or increasing observing time to utilize the rotation of the earth. A single pair of telescopes is separated by some baseline vector $\vec{B}$. The observed spatial frequency depends on $\vec{B}/\lambda$. As the Earth rotates relative to the source, the value of $\vec{B}/\lambda$ changes, which allows each baseline to sample many different Fourier components of the T(x,y). This technique is the basis of modern interferometry and is known as aperture synthesis. A sample of the UV coverage in for a single observing session and the total coverage for the interferometric data used in this thesis can be seen in Figure 2.7, respectively.

For an array with N elements, there are $N(N-1)/2$ pairs of visibilities. The placement of antennas in interferometric arrays are typically designed to maximize UV coverage. Due to the gaps in the UV coverage, the observed brightness of the source becomes

$$T'(x,y) = \iint W(u,v)V(x,y)\exp(-2\pi i(ux+vy))dudv \qquad (2.9)$$

where W(u,v) is a weighting function, specifically W(u,v) is 0 where UV plane is not sampled from observations. The observed brightness can than be written as

$$T'(x,y) = B(x,y) * T(x,y) \qquad (2.10)$$

$$B(x,y) = \iint W(u,v)\exp(-2\pi i(ux+vy))dudv \qquad (2.11)$$

where B(x,y) is the synthesized beam. For optical telescopes, the synthesized beam is the equivalent of the point-spread function.

The observed brightness contains artifacts that are a result of an incompletely sampled $W(u, v)$. The final image with these artifacts removed is created by modeling $T(x, y)$ through deconvolving $B(x, y)$ from $T'(x, y)$.

2.2.2 Previous HCN and HCO+ Observations

The nucleus and western spiral arm of M51 were mapped in HCN and HCO+ using observations made with the OVRO and, more recently, the CARMA. The OVRO observations were made between October 2003 and May 2004. The OVRO array consists of six dishes, each 10m in diameter. A three pointing mosaic was made and the field of view (FOV) of the pointing are shown as green circles in Figure 4.2. We made HCN (HCO+) channel maps with a synthesized beam of 7″.7x7″.4 (7″.8x7″.5) with a per channel RMS of 6.6 mJy beam^{-1}(8.1 mJy beam^{-1}) at 6.765 km s^{-1}(6.723 km s^{-1}).

The CARMA observations were made throughout the month of October 2010 in the C array configuration under the project code c0587. The CARMA array consists of the six 10m dishes from the OVRO array and an additional nine 6m dishes from the former Berkeley Illinois Maryland Association (BIMA) array. Baselines varied between 30m and 350m in the C configuration. A three pointing mosaic was observed at the same locations as the previous OVRO observations but with an extended FOV due to the addition of the 6m dishes. The increased FOV and locations of pointings are shown in Figure 4.2 in purple. We made HCN (HCO+) channel maps with a synthesized beam of 2″.4x1x2″.1 (2″.4x2″.1) with a per channel RMS of 6.6 mJy beam^{-1}(7.0 mJy beam^{-1}) at a velocity resolution of 6.765 km s^{-1}(6.723 km s^{-1}).

The previous HCN (HCO+) channel maps were made using a synthesized beam of 4″.25x3″.95 at 6.765 km s^{-1}(4″.4 x 4″.1 at 6.72 km s^{-1}), the velocity increment of the OVRO channel maps. The typical noise levels of the channel maps are 5.2 mJy beam^{-1}(5.4 mJy beam^{-1}). Integrated intensity maps of the pervious data are presented in Figure 2.6.

2.2.3 Observing HCN and HCO+ with CARMA

We performed a single pointing D array observations of HCN and HCO+ on a region of the western spiral arm in M51. The goal of these observations is

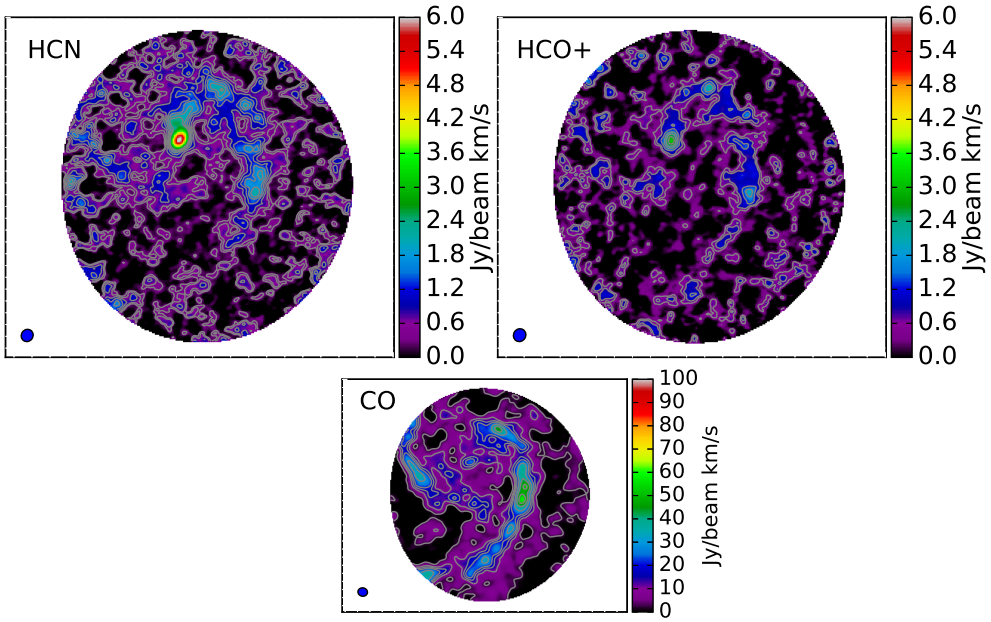

Figure 2.6 Previous combined OVRO and CARMA C HCN and HCO+ maps of M51. The FOV of these observations can be seen in Figure 4.2. Left: Integrated HCN (1-0) intensity. Center: Integrated HCO+ (1-0) intensity. Right: Integrated CO (1-0) intensity from Koda et al. (2009) smoothed to the resolution of the dense gas tracers. The contours of the HCN and HCO+ panels are multiples (3,5,7,9) of the corresponding to the σ values. The beam size is shown in the bottom left corner for each panel. The images are in units Jy beam^{-1} km s^{-1}.

to extend our FOV coverage along the spiral arm from the previous archival data. The observations were performed in December 2013 and January 2014 under the project code c1167. Total observing time for this project was 32 hours. Pointing center for the observations was 13:29:52.70, + 47:10:48.40. The reduction and imaging processes discussed in this section were applied to both the HCN and HCO+ data.

During this thesis work, I served as an on-site observer for five weeks. This required being on call and present at the CARMA observing site in California. The duties of the observers were wide and varied. On a typical observing run, observers were in charge of scheduling the observing programs to be run that day based on weather conditions and priority of observing program. Observers were also the first responder for with any software or hardware issues associated with the array. In addition, they assisted with configuration changes and various array maintenance tasks. In the event of poor weather conditions, observers were required to respond 24/7 to either remove snow from the antennas or place them in a safe position due to high winds. I had the opportunity to be involved with all of these various aspects while being an on-site observer at CARMA.

2.2.4 CARMA Data Calibration

Additional observations were made of calibration targets. These sources have known properties in order to understand and correct for instrument calibrations. Typical sources with known properties used for calibration are planets and quasars. There are four calibration stages of interferometric data reduction: bandpass calibration, phase calibration, gain calibration, and absolute flux calibration.

- Bandpass Calibration: Determine variations of amplitude and phase based on frequency. The variations between spectral channels are determined and a function is fit to remove any offsets across frequency. This variation is independent over the observing time and does not fluctuate over the course of the observations. A bright quasar was observed for 15 minutes at the beginning or end of the observations. 3C273 was our bandpass calibrator.

- Gain Calibration: Determine variations of amplitude over time. The variations in amplitude gain over time can be corrected by observing a

bright quasar. The intensity of a bright quasar should not vary over the length of a typical observation. A bright quasar, typically located near the target source is observed every 30 minutes for about five minutes to determine the gain variations. This corrects for changes in the weather and instrumental response. For our observations 1153+495 was used as the gain calibrator.

- Phase Calibration: Determine variations of phase over on time. Like the gain calibration, instrumental changes and slight errors in the relative locations of the antennas, can cause variations in phase. The phase variations are determined from observations of a bright quasar. Typically the same as sused for the gain calibrator, 1153+495 was used as the phase calibrator. Since the phase of the quasar, a point source, should be zero, the instrumental variations in phases over time can be fit to zero.

- Flux Calibration: By observing a source with a known flux allows for a determination of the gains and thus calibrated the flux of the observed source. Typically, flux calibration observations are taken of a planet at the beginning or the end of an observing session. Bandpass calibrations are done primarily through the observations of Mars. The observatory provides models of planets flux. 1153+495 was used as the gain calibrator.

The data was obtained over various observing sessions. Observation were run on-site by local observers. For this project, a custom observing script was submitted to the observatory in advance. A detailed table of observing session dates is seen in Table 2.2.4. We obtained observations of both HCN and HCO+. The total UV coverage of our observations can be seen in Figure 2.7.

There are some specific properties that make data reduction possible, specifically the closure effects between baselines that form closed figures. Any group of three baselines provide information about the phases introduced by the instruments. The phase closure is required by a set of three antennas during the observations of a point source. Specifically, the set of fringes observed for a group of three antennas, a, b, and c. For any pair of fringes between two antennas, ϕ_{ij}, the following sum of the fringe phase can be written,

$$\phi_{abc} = \phi_{ab} + \phi_{bc} + \phi_{ca}. \tag{2.12}$$

Table 2.2. Project c1167 Observation Log

Observing Bock	Date	Observing Length (Hours)
c1167.1D88M51.9	2013-12-27	3.50
c1167.1D88M51.12	2013-12-29	3.90
c1167.1D88M51.13	2013-12-31	3.90
c1167.1D88M51.14	2014-01-01	5.40
c1167.1D88M51.15	2014-01-02	9.60
c1167.1D88M51.16	2014-01-04	6.00

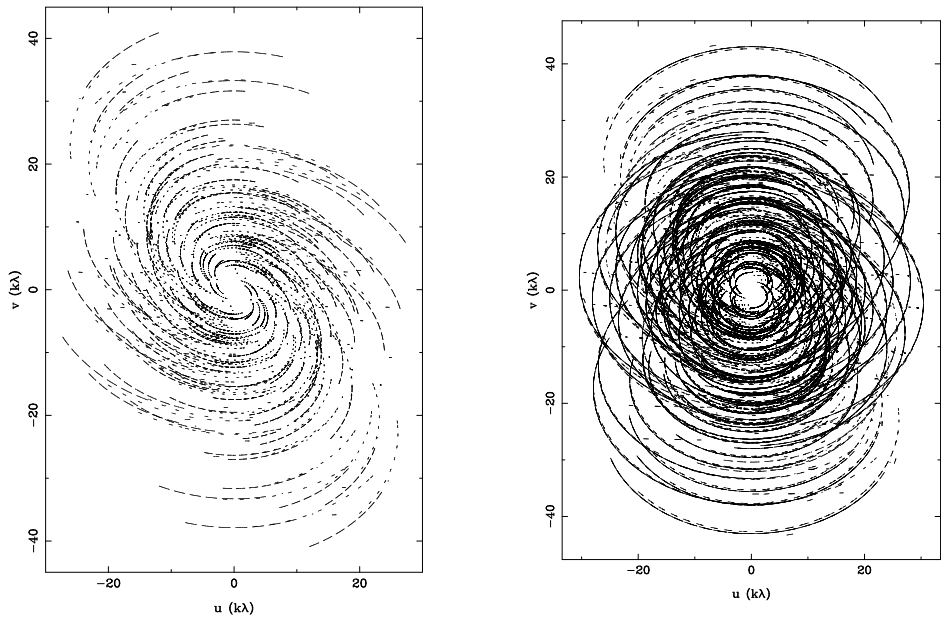

Figure 2.7 (a) UV coverage for an a single observing session on 2013-12-27 and (b) UV coverage for total observing program c1167. The arcs are produced by repeated observations during a single observing program while the earth moves with respect to the source in the sky and the projected baselines change.

This quantity is referred to as the closure phase. There is also a closure relationship for the amplitude of fringes, for any four sets of antennas,

$$A_{\rm abcd} = \frac{|V_{\rm ab}||V_{\rm cd}|}{|V_{\rm ac}||V_{\rm bd}|}. \tag{2.13}$$

Both the closure phase and closure amplitude relationships are assumed to be independent of instruments or atmospheric effects, therefore then can be used to determine the gains for each antenna. The adaption of these relationships into our data reduction are described below.

In addition to the calibration steps, there are also random variations that need be masked. Specifically, spikes in instrument response can cause isolated measurements to fluctuate. This may effect a single antenna, single baseline, or a single moment in time and many permutations of those. In order to 'flag' and remove these fluctuating measurements, the data is inspected post calibration for individual measurements that deviate from the normal distribution of that data set. This process is commonly refereed to as *flagging*. Removal of these points are crucial to avoid artifacts in the final data. Typically, there is a duty cycle between applying the systematic calibration stages and flagging erroneous data, as fitting performed during systematic calibration stages can improve greatly by flagging.

The reduction steps outlined above explain the basic reduction applied to our data, the reminder of this session describes how these steps were applied to the data in this thesis. Reduction scripts were created and utilized the MIRIAD data reduction software (Sault et al. 1995). The first stages of these scripts clean up the data, and isolate the useful data required for data reduction. MIRIAD tasks are preformed to flag data where any antennas are shadowed and apply corrections for the linelength system, which monitors the delay of signal across optical fibers to the antennas. Next, measurement of the positions of the antennas, taken close to the observation date, are updated within the data to ensure correct baseline calculations between antennas.

The task mfcal is used to determine the bandpass calibration required such that the bandpass shows zero-phase and constant amplitude across the bright quasar, 3C273. This correction is applied to all of the data taken. Next, the gains are determined for the phase and amplitude of the source 1153+495, this is done using the selfcal task. Using the phase and amplitude relationships above, selfcal with find the gain and phase solutions for them to be satisfied. These stages of data reduction, bandpass and gain calibrations, are performed and at the end the signals are visually inspected for issues.

Any data that appears to have obvious errors are flagged out of the data set and these two reduction steps are rerun. Sometimes these errors appear for a single antenna, single baseline, and/or single observing time and all combinations of these. This duty cycle between reduction and flagging typically last two to three cycles. Once the bandpass and gain calibration solutions have reached a point where the data appears to have been correctly reduced, the correct flux values are obtained using the model of the flux of Mars from our observations.

2.2.5 CARMA Data Imaging

In order to create an image from the now reduced visibilities, an inverse Fourier transform is performed. This is done using the MIRIAD task invert, which grids the data and performs a Fast Fourier Transform. This first image, created directly after the inverse Fourier transform, T'(x,y) is referred to as a *dirty* image because of the artifacts, or *side lobes*, present in the image due to the weighting function and missing information in the UV plane. The dirty map and synthesized beam for our observations combined with previous data can be seen in Figure 2.8 this previous data will be discussed in Chapter 4.

In order to model the true T(x,y), a process called CLEAN is used to determine the locations of the true emission and remove artifacts associated with the synthesized beam. Recall that dirty map, T'(x,y) is a convolution of the true sky brightness, T(x,y) with the dirty beam B(x,y). The typically 'cleaning' algorithm works by identifying peaks in source emission, while removing false artifacts due to the synthesized beam, or dirty beam. Consider the case of a simple emission map with a few strong point sources. The shape of the 'dirty beam' will be subtracted from that point source and the location and amplitude noted. This cleaning process would remove artifacts created by the dirty beam. Once the emission levels associated with that peak are subtracted to reach the noise floor, the next brightest peak is found. This is done for all emission peaks. This cleaning process is done in many iterations such that a small percentage of the peak value is subtracted from each peak before the next peak is identified. Iterations should continue until all the peaks have reached the noise floor. The output of the clean task is a map of the noise and a map of the emission peaks and their associated emission intensities. The final map is reconstructed by convolving the peak location map and amplitudes and a modeled beam, then adding the noise map. This modeled beam is a 2D gaussian fit to the first peak in the dirty beam. This

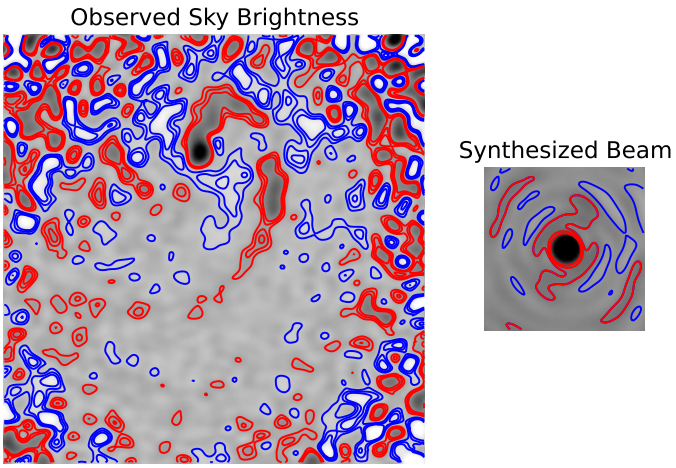

Figure 2.8 (a) Measured sky brightness or dirty map and (b) synthesized beam or dirty beam for the interferometric HCN data used in this thesis.

is done using the MIRIAD task restor. The final map of our interferometric data is shown in Figure 2.9, this is the final map generated from Figure 2.8. The negative emission present around the spiral arm, shown in blue, is significantly less in the final image than that in the dirty image. This final map will be analyzed in Chapter 4.

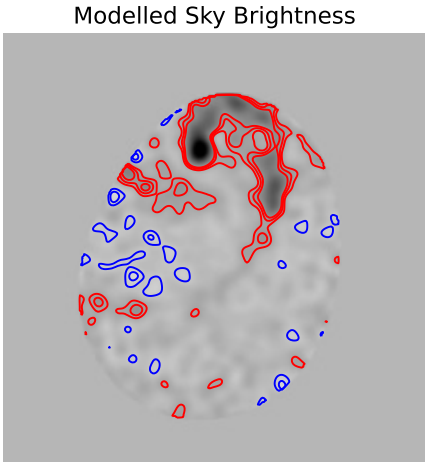

Figure 2.9 Final modeled sky brightness of the interferometric HCN data used in this thesis with FOV sensitivity cut applied. The noise in this image is greatly reduced compared to what is seen in Figure 2.8.

Chapter 3

Offsets Between Bulk Gas and Star Formation

Understanding how gas evolves during galactic rotation is critical to understanding the ISM, in particular the gas flow through spiral arms and interarm regions. The compression of gas in spiral arms, according to the density wave theory, would cause gas to accumulate on the upstream side of a spiral arm and eventually trigger SF which is seen on the downstream side of the spiral arm. In face-on galaxies, this sequence of evolution in time appears as a spatial sequence across spiral arms. Offsets between molecular gas and regions of star formation have been suggested by theory and seen observationally (Roberts 1969; Vogel et al. 1988; Scoville et al. 2001). These offsets were explained using the classic theory of gas evolution and have been used to derive properties of galaxies and also a timescale for which SF occurs. The offsets are important as they can be used as a probe of galactic dynamics and the parameters derived from the offsets can give insight on processes which trigger SF. A discrepancy has arisen between different measurements of these offsets (Egusa et al. 2004; Tamburro et al. 2008; Egusa et al. 2009; Foyle et al. 2011).

In this chapter, we present a study to clarify the source of the discrepancy in these previous works and after resolving this discrepancy discuss how the results impact the evolutionary sequence of gas across spiral arms. We characterize this expected spatial sequence from the compression of gas, spiral arm traced in atomic and molecular gas to SF using the methods developed by the previous works. Portions of this chapter are a reproduction of a published paper on the geometrical offsets measured in M51. It was originally published

in the Astrophysical Journal (Louie et al. 2013). This paper is reproduced by permission of the American Astronomical Society. The co-authors directed and supervised the research that forms the basis for this paper.

3.1 Introduction

The density wave theory (Lin & Shu 1964) has been a central paradigm for the formation of spiral structures in galaxies. (Roberts 1969) suggested that star formation (SF) in spiral galaxies is triggered by a spiral density wave and predicted that Hα emission around newly-formed stars should be offset from and appear downstream of the gas spiral arm due to flow through the density wave. The offsets would not only be evidence of the density wave, but would allow measurement of the angular speed of the spiral pattern and the timescale for star formation (Egusa et al. 2004), given a velocity difference between the matter and the spiral pattern and assuming that the SF timescale is constant. The offset and circular velocity can be measured observationally as a function of radius, and should obey the relationship,

$$\Delta\Theta(r)_{A\to B} = (\Omega(r) - \Omega_p)\Delta t \tag{3.1}$$

where $\Delta\Theta(r)$ is the azimuthal offset angle between gas spiral arms (A) and star forming regions (B), $\Omega(r)$ is the angular velocity of the gas, Ω_p is the angular pattern speed, and Δt is the time that the gas takes to evolve into young massive stars after spiral arm entry.

A discrepancy has emerged in recent studies of offsets (Tamburro et al. 2008; Egusa et al. 2009; Foyle et al. 2011). In an analysis of ~ 10 galaxies, (Egusa et al. 2009, hereafter E09) derived offsets larger by an order of magnitude in general than (Tamburro et al. 2008, T08). More surprisingly, (Foyle et al. 2011, F11) reported primarily non-ordered offsets compared to those predicted by the standard density-wave theory (Eq. 1). This discrepancy directly affects the estimates for Ω_p and Δt, and thereby their physical implications for star formation. Indeed, the measured star formation timescales are inconsistent: $5-30$ Myr for E09 versus $1-4$ Myr for T08. The shorter timescale may imply very short lifetimes for giant molecular clouds (GMCs), i.e., their exceedingly rapid formation and destruction and associated rapid star formation (T08), while the longer timescale may be consistent with the gravitational collapse of gas at typical giant molecular cloud gas densities (E09).

This study explores the potential causes of the discrepancy. Two major differences among these studies are the choices of emission tracers and the methods of offset measurement. E09, and originally (Egusa et al. 2004), used CO (J=1-0) and Hα as tracers of the dense gas and recently-formed young stars, respectively. T08 and F11 used HI 21 cm emission and IR 24 μm emission to trace the locations of the compressed gas and young massive stars, respectively. T08 and F11 also compared low-resolution CO and 24μm emission on a subset of galaxies. F11 also investigated other tracers such as UV emission to trace SF and 3.6 μm emission to trace the old stellar population. CO is the established tracer of the dense star forming molecular gas, while HI, if concentrated around spiral arms, may coincide with the dense gas. Hα observations typically provide a higher angular resolution than observations at 24μm. However, Hα observations could miss dust-obscured star forming regions, whereas 24μm emission suffers very little from extinction.

The methods of offset measurement could also be the cause of the discrepancy. (Egusa et al. 2004) and E09 compared the location of emission peaks by eye. This "Peak Tracing" Method is intuitive and easy to apply, but is possibly biased. T08 and F11 used an automated cross-correlation method to avoid any human bias. This "Cross-Correlation" Method is apparently less subjective, but surprisingly its application leads to inconsistent results even when the same data are used (T08 and F11).

The offset measurements may constrain emerging theories of spiral arm formation. In N-body simulations, the spiral arms appear to form as material arms instead of density waves (Wada et al. 2011). Spiral structures are constantly formed and broken apart by gravitational shearing (Goldreich & Lynden-Bell 1965). In this case, no clear offset would be expected across the spiral arm. The stellar and gas spiral arms are most likely co-spatial, the gas being pulled toward local stellar potential minima, instead of passing through them as predicted by the density-wave theory (Wada et al. 2011). (Dobbs & Pringle 2010) performed hydrodynamic simulations in stationary and transient stellar spiral structures (i.e., density-wave spiral versus material spiral, respectively) and found that the offset depends strongly on the nature of the stellar spiral structures. The ordered offsets measured by (Egusa et al. 2004), T08, and E09 support the density wave theory in its simplest form with a single pattern speed, while the result of F11 could indicate a transient spiral structure without a fixed pattern speed. Resolving the discrepancies in the offset measurements is therefore increasingly important.

In this paper, we reexamine the measurements of the geometric offsets by

T08, E09, and F11, using the previously-adopted four tracers, HI, CO, 24μm and Hα emission, and using both the Peak Tracing and Cross-Correlation methods. We focus on M51 to clarify the primary causes of the discrepant results from previous studies. We conclude that the discrepancy comes from the different tracers, mainly because the HI 21 cm emission traces the gas dissociated by young stars rather than the parental gas for star formation. We will demonstrate that the two measurement methods provide consistent results if appropriately applied. In addition, we will discuss some caveats in applying the offset model for deriving the pattern speed and the SF timescale.

M51 is among the galaxies analyzed by T08, E09 and F11. However, they did not find consistent geometrical offsets $\Delta\Theta$ (and, almost equivalently, the star formation timescale Δt). For example, T08 measured $\Delta t = 3.4 \pm 0.8\,\mathrm{Myr}$ ($\Omega_p = 21 \pm 4\,\mathrm{km\,s^{-1}\,kpc^{-1}}$), while E09 obtained $\Delta t = 13.8 \pm 0.7\,\mathrm{Myr}$ ($\Omega_p = 40 \pm 4\,\mathrm{km\,s^{-1}\,kpc^{-1}}$), i.e. a factor of 4 difference in Δt (a factor of 2 in Ω_p). A summary of the tracers used and results can be found in Table 3.1.

The data for the gas and star formation tracers are described in § 3.2. The offset measurement methods of the previous studies are discussed in § 3.3. Our results with four emission tracers, HI, CO, 24μm, and Hα, are discussed in § 3.4. The measurement methods and tracers are compared in §3.4.2 and §3.4.3, respectively. The cause of the discrepancies among previous measurements and the limitations of the model are discussed in § 3.5. A summary of this work is given in § 3.6.

3.2 Data

In order to elucidate the causes of the discrepancy, we compare the tracers (i.e., HI, CO, 24μm and Hα) previously used in T08, E09 and F11. The HI data are from the HI Nearby Galaxy Survey (Walter et al. 2008, THINGS), an HI survey made with the Very Large Array at the National Radio Astronomy Observatory. We use the data reduced with natural weighting. The CO data are from (Koda et al. 2009, 2011) and were obtained by combining Combined Array for Research in Millimeter Astronomy (CARMA) and Nobeyama 45m telescope observations as a part of the CARMA-Nobeyama nearby galaxies (CANON) CO (J=1-0) survey. The 24μm and Hα data are from the Spitzer Infrared Nearby Galaxies Survey (Kennicutt et al. 2003, SINGS). The 24μm observations were made with the Spitzer Space Telescope and the Hα observations were taken with the 2.1m telescope at The Kitt Peak National

Table 3.1. Summary of Previous Offset Studies

	Tracers		Analysis	Method	$t_{\rm SF}$	$\Omega_{\rm p}$
	Gas	SF			(Myr)	($\rm km\,s^{-1}\,kpc^{-1}$)
Tamburro et al. 2008	HI	24μm	Arm 1&2	CC	3.4 ± 0.8	21 ± 4
Egusa et al. 2009	CO	Hα	Arm 1&2	PT	13.8 ± 0.7	40 ± 4
Egusa et al. 2009	CO	Hα	Arm 1	PT	7.1 ± 0.5	31 ± 5
Foyle et al. 2011	HI	24 μm	Arm 1&2	CC	No ordered offsets	

Observatory. The spatial resolutions of HI, CO, 24μm and Hα data are $\simeq$6" (280 pc at 9.6 Mpc), 4" (160 pc), 5.7"(256 pc), and 1.9" (88 pc), respectively.

The HI and 24μm data are the same as used in T08 and F11. The CO data have a higher resolution and sensitivity than the data from the BIMA Survey of Nearby Galaxies (BIMA-SONG; Helfer et al. 2003) that were used in T08 and E09; however, both resolve the molecular spiral arms in M51, and there should not be much difference in the offset analysis. F11 used much lower resolution (13") CO (J=2-1) data from the HERA CO-Line Extragalactic Survey (HERACLES; Leroy et al. 2009) in their analysis. The Hα image is not the same as the one that E09 used, though it has a similar resolution. We do not expect a significant difference between the two, because the analysis is weighed significantly to high signal-to-noise regions in bright spiral arms. A slight improvement in the S/N does not change the positions of the bright peaks. We adopt the following parameters for M51: a distance (D) of 9.6 Mpc, a major axis position angle (P.A) of 22° and an inclination angle (i) of 20° (Sofue et al. 1999). We will test the different sets of these parameters and confirm that the choice does not affect our conclusions.

3.3 Offset Measurement and Analysis

The procedure for the offset method has two major steps: (1) measurements of azimuthal offsets between gas and star formation tracers, and (2) the determination of a star formation timescale and pattern speed using the measured offsets and a rotation curve. Our primary focus is to investigate possible causes of the discrepancy in step (1). The discrepancy between the previous offset measurements (i.e., large offsets in E09, small offsets in T08, and no ordered offsets in F11) could be due to differences in the methods employed and/or in the adopted tracers of dense gas and star forming regions. We briefly summarize the two methods here.

Both methods are based on theoretical predictions of the density-wave theory (Roberts 1969). Assuming a flat galactic rotation curve and a constant pattern speed, the relative velocity between the gas/stars and the spiral pattern changes with radius. If the timescale of SF after spiral arm compression is a constant, this differential motion results in a spatial offset between the gas spiral arm and star forming regions, and the offset changes with radius. If we measure the offset as a function of radius, the SF timescale and pattern speed can be determined (Egusa et al. 2004). Figure 3.1 shows

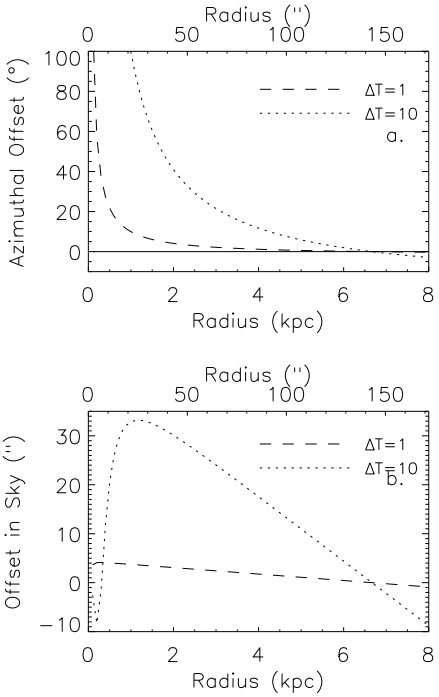

Figure 3.1 The expected offsets determined from Eq. (1) for a constant v_{gas} of $200\,\mathrm{km\,s^{-1}}$ and Ω_p of $30\,\mathrm{km\,s^{-1}\,kpc^{-1}}$. Two star formation timescales are assumed, $\Delta t = 1\,\mathrm{Myr}$ and $10\,\mathrm{Myr}$. (a) The azimuthal offset in the galactic disk plane as a function of radius. (b) The angular offset in the sky. The offset is expected to be largest at smaller radii and approaches zero with increasing radius.

two model plots of the expected offset versus galactic radius, assuming SF timescales of 1 and 10 Myr and other parameters appropriate for M51 (i.e., pattern speed and rotation velocity). Figure 3.1 (a) shows the azimuthal offset in the galactic disk, while Figure 3.1 (b) shows the offset in the sky. The azimuthal offset is expected to be large at small radii and approximately zero at large radii.

For both methods, the four images, HI, CO, 24μm and Hα, are regrided to the same pixel size using the Multichannel Image Reconstruction, Image Analysis, and Display (MIRIAD) software package (Sault et al. 1995) and are deprojected using the MIRIAD task "deproject". The deprojected images were transformed into phase diagrams (radius, azimuth) using the MIRIAD

task "polargrid". After the production of the phase diagrams, the analysis continues differently for each method as discussed below.

We wrote our own IDL programs to reproduce the different measurement techniques of E09, T08, and F11, following the detailed procedures discussed in these papers.

3.3.1 Peak Tracing Method

A measurement method for the geometrical offset was developed by (Egusa et al. 2004) and updated in E09. The offset is measured by eye as the azimuthal angular offset between the emission peaks of gas and star forming region tracers. This *Peak Tracing method* starts by binning the phase diagrams in the radial direction with an appropriate bin size to match the spatial resolution of all tracer images (here we use a bin size of 5"). The emission peaks are visually determined in an azimuthal intensity profile of each bin. The offsets are defined as the azimuthal shifts of the peaks between the two tracers. We find that this visual identification tends to pick up only peaks with a high signal-to-noise ratio. Obviously, some radii are not included in the analysis if no emission peaks could be identified in their azimuthal profiles. Figure 3.2 shows examples of identified peaks in all the four tracers in a part of Arm 1: (a) HI , (b) CO, (c) 24μm, and (d) Hα. Gas is flowing in a counter-clockwise direction.

3.3.2 Cross-Correlation Method

T08 cross-correlates the azimuthal profiles of the gas and SF tracers in each radial bin. They define a normalized cross-correlated function,

$$cc_{x,y}(l) = \frac{\Sigma_k[(x_k - \bar{x})(y_{k-l} - \bar{y})]}{\sqrt{\Sigma_k(x_k - \bar{x})^2 \Sigma_k(y_k - \bar{y})^2}}, \tag{3.2}$$

where x_k and y_k are the fluxes in gas and SF tracers (in T08 and F11, HI and 24 μm, respectively). $\bar{x}$ and $\bar{y}$ are the mean values of the fluxes. l is the lag (or the shift) in pixel units between the two profiles. The denominator normalizes the cross-correlation function based on the variance of each data set; this normalized cross-correlation function is useful when adopting a cutoff value to remove low signal-to-noise data at different wavelengths. In principle, the cross-correlation function shows a maximum at the value of $l = l_{\max}$

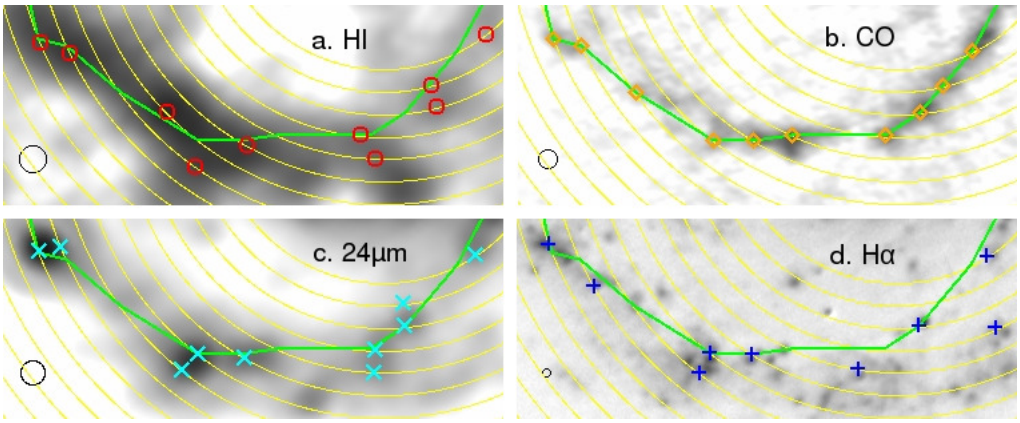

Figure 3.2 Images of a portion of Arm 1 in (a) HI, (b) CO, (c) 24μm, and (d) Hα. The positions of peaks identified by the PT method in radial bins (centered on the concentric arcs) are plotted on the images. The black circles in the lower-left corners indicate the resolutions of the data. The gas flow direction is counter-clockwise. As a reference, the CO peaks are connected with green lines in all panels.

that best aligns the two profiles – finding the peak of the cross-correlation function should be enough to obtain $l_{\max}$. In practice, we fit a polynomial to the profile of the cross-correlation function around the peak to reduce the effect of noise. T08 uses a fourth-degree polynomial, and we follow their method. Examples of the cross-correlation function for a radial bin (at the galactic radius of 2.51 kpc) are shown in Figure 3.3 for each set of tracer combinations. The offset is simply $\Delta\Theta(r) = l_{max}(r)$. T08 adopted a lower threshold (i.e., 0.2) for the normalized cross-correlation function to reject measurements with low significance and F11 used a threshold of 0.3. We set the threshold for an acceptable cross-correlation value to 0.3 to avoid low signal-to-noise measurements.

3.3.3 Parameters and Errors

We apply both the Peak Tracing Method and the Cross-Correlation Method to two gas tracers (CO and HI) and two SF tracers (Hα and 24μm). The phase diagrams are binned radially in 5" increments for all data. This bin size is chosen to match the resolutions of the HI and 24μm data. We denote the spatial offset between the gas (tracer A) and star forming regions (B)

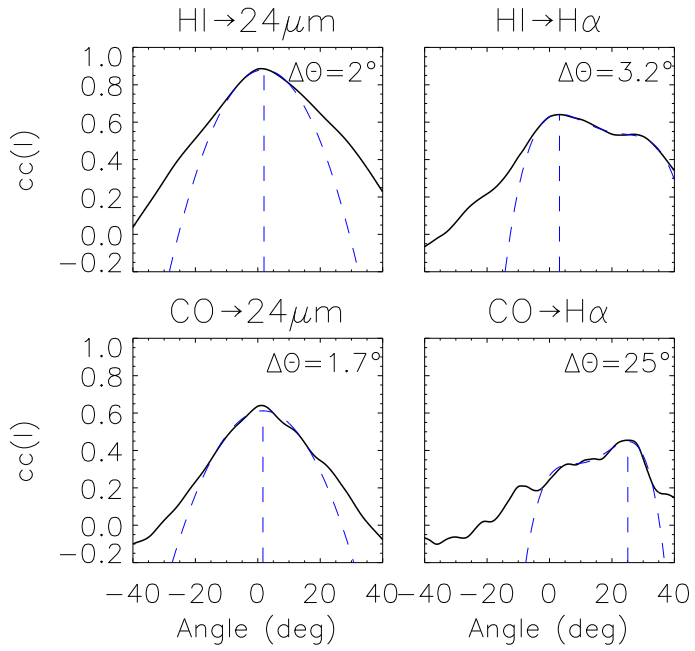

Figure 3.3 Examples of the cross-correlation function for the four combinations of the tracers at a radius of 2.51 kpc. The dashed curve show a forth degree polynomial fit around the maximum peak. The dashed blue line shows the location of the maximum peak. The offset value is listed in the top right of each panel for each tracer combination.

as $\Delta\Theta_{A\rightarrow B}$ and measure $\Delta\Theta(r)_{HI\rightarrow 24\mu\mathrm{m}}$, $\Delta\Theta(r)_{HI\rightarrow H\alpha}$, $\Delta\Theta(r)_{CO\rightarrow 24\mu\mathrm{m}}$, and $\Delta\Theta(r)_{CO\rightarrow H\alpha}$. If multiple peaks exist in the cross correlation function, the largest is chosen, since by definition this is the location where the peaks of the spiral arms are best aligned. For the Peak Tracing Method, the locations of any multiple peaks are checked against maps of M51 to make sure that they correspond to the spiral arms instead of emission in the inter arm regions (Koda et al. 2009).

Two types of error could be introduced in the analyses: (1) due to uncertainties in determination of peak positions in each tracer, and (2) due to the misassociation of the peaks in gas and SF (e.g., in the case of multiple peaks). The first type of error is easy to estimate and is simply related to the resolution of the images in both methods. This relation may not be so obvious in the case of the Cross-Correlation Method, but, for example, if there are point sources convolved with point-spread functions (PSF; i.e., resolutions) the cross-correlation function is simply a multiplication of the two PSFs with a variable lag. Its width (or the associated error) is therefore determined by the sizes of the resolutions. In all the data. we measure only the positions of bright peaks and the positional accuracy should be a small fraction of the resolutions. We here conservatively adopt half of the resolution as the error. This choice provides an error similar to that estimated by E09, but much larger than that of T08. The second type of error is difficult to estimate, and we neglect it for now. This error, however, should appear as scatter in our measurements.

3.4 Results

We qualitatively compare the images of the different tracers before making quantitative measurements. To distinguish the two arms, we define Arm 1 as the spiral arm that is further from the companion galaxy and Arm 2 as the one that connects to the companion.

Figure 3.4 shows phase diagrams of the four tracers. Contours of star formation tracers (Hα and 24μm) are shown on gas tracer images (CO and HI). Gas flows in the direction of increasing azimuthal angle. Figure 3.2 shows the relative locations of the peaks in the four tracers with respect to CO (i.e., green line). If we compare the peak locations of the SF tracers, Hα and 24μm, with respect to CO peaks, the Hα emission appears downstream of the CO emission when an offset is seen. This is consistent with the findings

in E09. The 24μm peaks show a similar trend and appear to be leading the CO peaks. Most important are the locations of the HI peaks as they are mostly at the leading side of CO, the well-established tracer of star-forming gas. The HI peaks appear to be spatially closer to the peaks of the two star formation tracers. This trend is inconsistent with the hypothesis in T08 and F11 that the HI traces the compressed, parental gas for SF. The Hα and 24μm peaks appear at similar locations in most radial bins, although occasionally they show offsets. The offsets between CO and Hα/24μm are evident over a range of radii, while HI shows little or no offsets from Hα and 24μm emission. Another notable point is that CO is predominantly in the inner part of the galaxy, while HI is in the outer part.

We note that the spiral arms do not form narrow smooth lines; on closer inspection they are fragmented and wiggle back and forth between the leading and trailing sides (most obviously seen in CO; see also Koda et al. 2009). This causes an additional intrinsic error in the offset measurements.

We apply the Peak Tracing Method and Cross-Correlation Method to these four data sets, and quantitatively verify the cause of the discrepancies in the previous measurements. We omit the very central part (radii $\lesssim$ 2 kpc), since the spiral structure is tightly wound and we cannot reliably associate the star-forming gas and resultant young stars in that region.

3.4.1 Comparisons to Previous Works

Figure 3.5 compares the offsets measured using the same tracers and methods as the previous studies. The left column shows the results from the Peak Tracing method applied to one spiral arm (i.e., Arm 1; as in E09). The right column shows the same offsets but from the Cross-Correlation Method applied to both arms (as done in T08 and F11). The offsets between HI and 24μm are shown in the top panels, and the offsets between CO and Hα are shown in the bottom panels.

The measured offsets in Figure 3.5 are consistent with the previous measurements of T08, E09, and F11 in terms of the ranges of their amplitudes. E09 compared CO and Hα data using the Peak Tracing Method and found offsets up to 25-30 $^\circ$ in Arm 1. Figure 3.5 (*bottom left*) shows our corresponding measurement. The amplitude range of our offsets between CO and Hα is similar to that in E09 (see their Figure 5, Arm 1). Our range in Arm 2 is also consistent with that of E09 (see Figure 3.6). E09 found irregular offsets between CO and Hα along Arm 2, and our measurements for Arm 2 see sim-

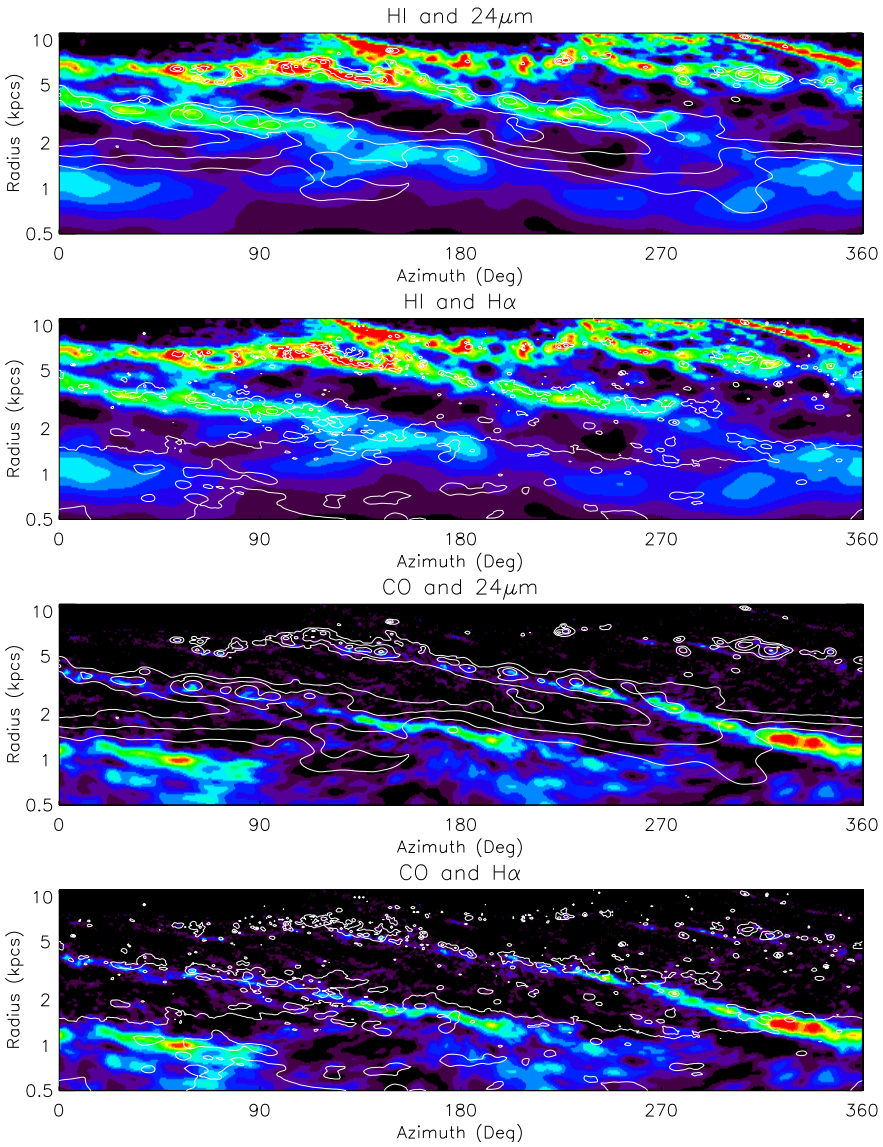

Figure 3.4 Phase diagrams of combinations of the four tracers for comparison of our results with those in T08, Fl1 (*top-right*) and E09 (*bottom-left*). The offsets are measured using the methods adopted in T08, F11 (*top panels*) and E09 (*bottom panels*).

ilar irregularities, which are discussed later in this section. T08 analyzed HI and 24μm using the Cross-Correlation Method (see their Figure 4) and found smaller offsets (mostly less than 5-10 °), except for the innermost radii (some large offsets of 15-20° $\lesssim$ 2 kpc). In our comparison of HI and 24μm (Figure 3.5, *top right*) we find similar small offsets, most of which are under 10 ° in $\gtrsim$ 2 kpc, consistent with T08 results. We were unable to measure offsets at the innermost radii (discussed above). F11 also measured offsets between HI and 24μm using the Cross-Correlation Method and found that they are mostly under 10° (their Figure 10), which is comparable to our amplitude range. The amplitude of the offsets found by T08, E09, and F11 agrees with our measured offsets when we use the same set of tracers and measurements method. Our measurements reproduce the amplitude discrepancy in the previous studies.

Figure 3.6 shows plots of all of the azimuthal offsets measured for each set of tracers as a function of galactic radius for the Peak Tracing method (*left two columns*) and the Cross-Correlation method (*middle two columns*). We measure the offsets in the two arms separately in these four columns. T08 and F11 analyzed the two arms together to measure one offset at each radius. For comparison, we also analyze the two arms together and show the plots in Figure 3.6 (*right column*). E09 found a strange trend in Arm 2, where the offset increases with radius (as opposed to the prediction in Figure 3.1). Our results for Arm 2 from the Peak Tracing method show similar behavior. Along Arm 2, the emission from the SF tracers appear to be scattered over a large area (though mostly at the leading side of the arm). Therefore, we discuss only Arm 1 in the following analysis when we analyze the two arms separately.

T08 also analyzed CO and 24μm data (their Figure 7) and found that the offsets are even smaller than those seen between HI and 24μm. We found the contrary. The offsets between CO and 24μm in Figure 3.6 (*third row*) are larger compared to those between the HI and 24μm (*top row*). F11 also compared a lower-resolution CO image with a 24μm image and noted possible evidence for ordered offsets in M51, though they did not quantify the CO$\rightarrow$24μm offsets further. Indeed, compared to their Figure 11, we find even larger offsets at the small radii (Figure 3.5 (*top right*)). Even if we smooth our CO data to a 13" resolution to match F11's, we still find larger offsets than F11. F11 also analyzed the two arms separately, but report no difference. Again, this is inconsistent with our results. Part of the reason for this difference may be that they used higher transition CO (J=2-1) data

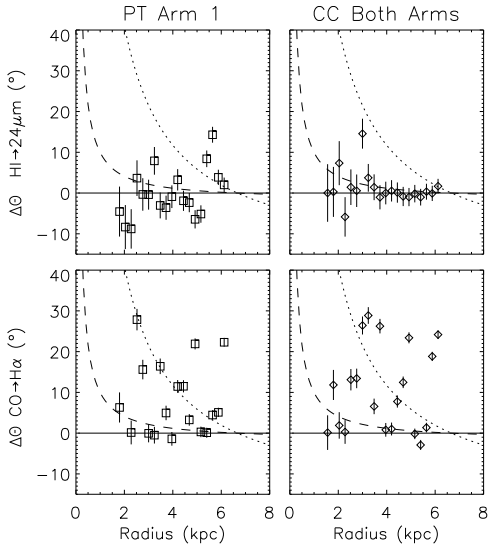

Figure 3.5 Azimuthal offsets between gas and SF tracers. The top row shows the offsets between HI and 24μm emission ($\Delta\Omega_{\mathrm{HI}\rightarrow 24\mu\mathrm{m}}$, while the bottom row shows those between CO and Hα ($\Delta\Omega_{\mathrm{CO}\rightarrow \mathrm{H}\alpha}$). The Peak-Tracing (PT) method is applied to Arm 1 for the left column, and the Cross-Correlation (CC) method is applied to both spiral arms simultaneously for the right column. The top-right panel is directly comparable to the measurements by T08 and F11 (as it uses the same tracers and method). The bottom-left panel is comparable to the measurement by E09.

while we used CO (J=1-0). The higher transition emission might be excited due to heating by young stars (Koda et al. 2012). If that is the case, CO (2-1) should appear closer to SF tracers (i.e. smaller offsets).

3.4.2 Method Comparison

The two measurement methods provide, in general, consistent results and do not appear to be the cause of the discrepancy. Figure 3.7 directly compares the measured offsets in Arm 1 from the Peak Tracing Method and the Cross-Correlation Method (i.e., the points in Figure 3.6) and shows good agreement, with some outliers. The dotted lines have a slope of one. Two solid lines in each panel show $\pm 5^\circ$ from the dotted line. We find that 70% of the data points are within $\pm 5^\circ$. Except for some outliers, most of the measured offsets are comparable, and neither method appears to bias the offsets in any systematic way in any of the panels. The two methods give roughly consistent offsets. The top left panel only has 3 out of 19 radii where the two measurement methods do not show a correlation. For the top right panel 6 out of 19 points do not agree. The bottom left panel has 5 points out of 19 and the bottom right panel has 6 out of 17 points that do not show a correlation.

E09 discussed that the two arms show quantitatively different offsets and analyzed them separately with the Peak Tracing Method. The difference between the two arms is clear in Figure 3.6 (*first and second columns*). Since the two methods generally provide consistent results when applied to single arms, it is natural to expect differences in the measured offsets when the two arms are analyzed simultaneously using the Cross-Correlation Method. We see this in our analyses of both arms simultaneously (Figure 3.6 (*fifth column*) and separately (Figure 3.6 (*third and forth columns*)) with the Cross-Correlation Method. We note that both T08 and F11 analyzed the arms simultaneously, while F11 also isolated individual arms; the difference between the two arms was not mentioned in either case. From our work, regardless of the measurement method (the Peak Tracing or Cross-Correlation Methods) and the analysis (the two arms separately or simultaneously), the offsets are mostly positive, but do not appear ordered.

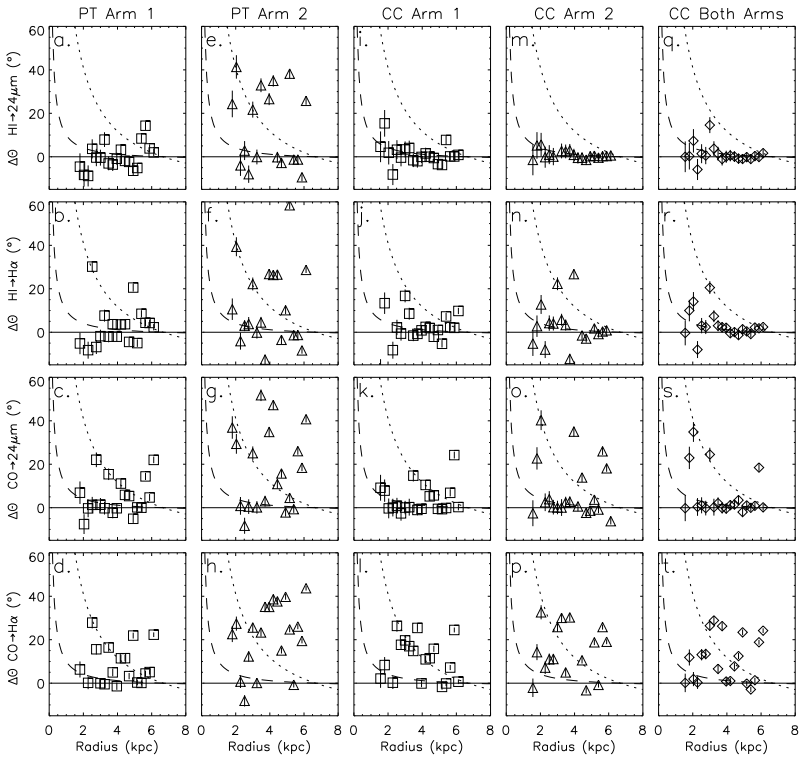

Figure 3.6 Azimuthal offsets between gas and SF tracers as a function of radius. The two spiral arms are analyzed both separately and simultaneously with the Peak Tracing (PT) method and Cross-Correlation (CC) method. *Left two columns:* the offsets determined by the PT method with the two arms analyzed separately, *Middle two columns:* by the CC method with the two analyzed separately, and *Right column:* by the CC Method with the two analyzed simultaneously. The rows from top to bottom show the offsets between HI $\rightarrow$ 24μm, HI $\rightarrow$ Hα, CO $\rightarrow$ 24μm, and CO $\rightarrow$ Hα. The model predictions of offsets for star formation timescales of 1 and 10 Myr are overplotted (see Figure 3.1).

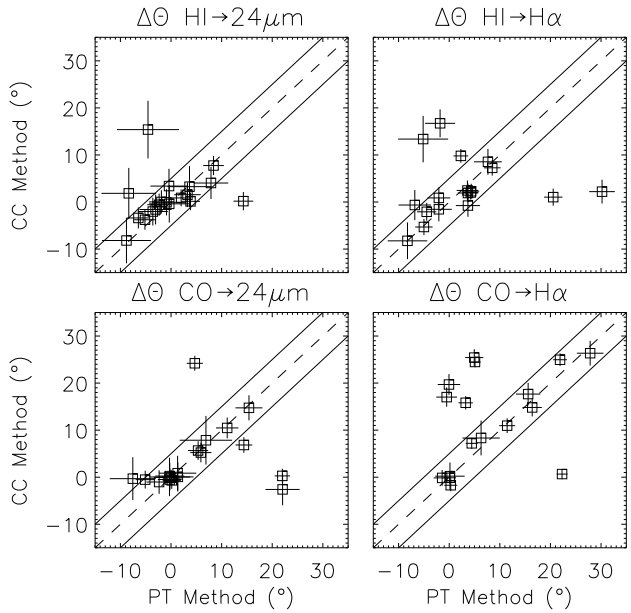

Figure 3.7 Comparisons between the offsets using the Cross-Correlation (CC) and the Peak Tracing (PT) methods. Offsets are measured at each radial bin for Arm 1, (see Figure 3.6). For all four tracers, the offsets measured with the two methods are in general agreement, with some outliers. Neither method appears to be biased in any systematic way. The fraction of data that show correlation is $\sim 70\%$. For reference, a dashed line with a slope of one is plotted and two solid lines are plotted to show $\pm 5°$.

3.4.3 Tracer Comparison

The choice of tracers appears to be the dominant cause of the discrepancy. Large differences are seen among the panels in Figure 3.6 (*left column*) and 3.6 (*middle column*), where the two arms are analyzed separately. Most remarkably, HI and 24μm – the combination employed by T08 and F11 show the smallest, if non-zero offsets for M51. Similarly, very small and zero offsets are seen between HI $\rightarrow$ Hα. If we use CO as a tracer of the dense, compressed gas (e.g., CO $\rightarrow$ Hα used by (Egusa et al. 2004) and E09), the offsets are much larger. Clearly, the difference in gas tracer is the dominant cause.

Figure 3.8 shows a direct comparison of the offsets between gas tracers and SF tracers in a given radial bin. The left column shows the offsets from the Cross-Correlation Method, while the right column shows those from the Peak Tracing method. The top panels compare the offsets found using HI with Hα and CO with Hα. The bottom panels show the same, but for 24μm. The offsets between HI and the SF tracers are mainly zero; however at the same radii the offsets between CO and the SF tracers are larger. In addition, when non-zero offsets are measured for both gas tracers, the offsets between CO and the SF tracers appear larger than the offsets between HI and the SF tracers. This is evident in Figure 3.8 as most data points appear in the top-left parts of the panels. Occasional outliers exist, but there are no more than two in each panel.

There are multiple components that could be contributing to the HI emission, which would give different offsets (and possibly non zero offsets) depending on which component is dominant at the radius in question. For example, HI may trace some of the gas compressed upon entry into a spiral arm, resulting in positive offsets, but would also trace the gas photo-dissociated by newly-formed young stars, leading to zero offsets. There is also an extended background component in the HI emission that is virtually everywhere across the galactic disk. We can also find some spatial displacements between HI and CO peaks in Figure 3.4 - HI is mostly downstream of CO, indicating that the HI emission is not simply from the dense gas, but multiple sources. This trend is also seen in Figure 3.9, where $\Delta\Theta_{\rm CO\rightarrow HI}$ is plotted against radius. The positive offsets suggest that HI is downstream of the CO. We will discuss this more in §3.5.1.

As for SF tracers, 24μm and Hα peaks are mostly consistent; therefore, the offsets with both tracers are more or less the same in Figure 3.6. However, there are some noticeable differences at some radii. For example, in Figure

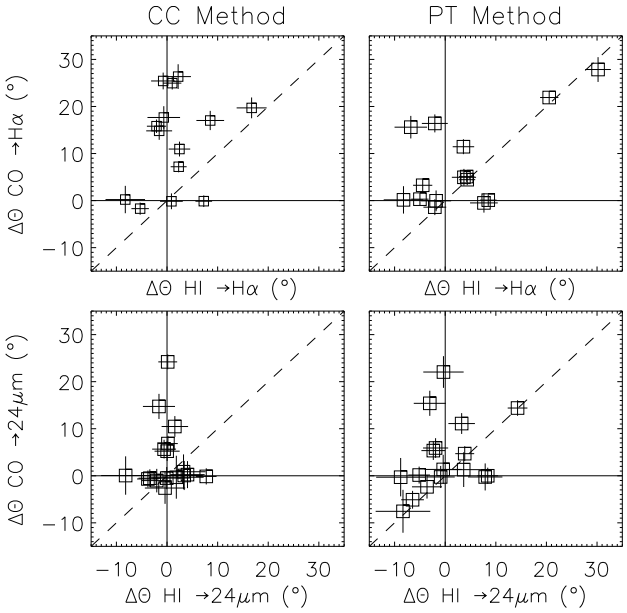

Figure 3.8 Comparisons between the offsets measured using different gas tracers on Arm 1. The top row shows the comparisons between $\Delta\Omega_{\mathrm{CO}\rightarrow\mathrm{H}\alpha}$ and $\Delta\Omega_{\mathrm{HI}\rightarrow\mathrm{H}\alpha}$, while the bottom row shows those between $\Delta\Omega_{\mathrm{CO}\rightarrow 24\mu\mathrm{m}}$ and $\Delta\Omega_{\mathrm{HI}\rightarrow 24\mu\mathrm{m}}$. The CC method is applied in the left column, and the PT method is applied in the right column. For reference, the dashed line has a slope of one (i.e., the two offsets are equal) and the two solid lines show zero (no offsets). Most points appear in the top-left of each panel, indicating that the offsets between CO and SF tracers are larger than those between HI and SF. The offsets between HI and SF tracers are often zero.

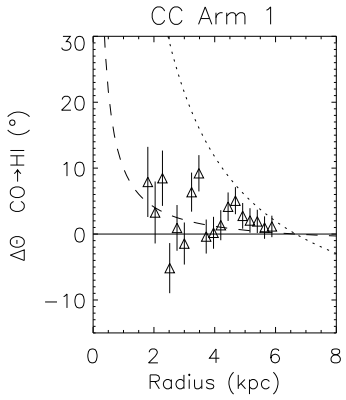

Figure 3.9 Offsets between CO and HI as a function of radius. Most offsets are positive, indicating that the HI peaks are on the downstream side of the CO.

3.4 there are radii at which Hα peaks appear downstream of 24μm peaks. This is perhaps due to the fact that the distribution of 24μm emission is affected by the distributions of both dense gas/dust and illuminating stars. If newly-formed stars escape from the dense parental gas (as we see in Figure 3.4), the 24μm emission may not trace the locations of the young stars any more, because the peak of dust density is left behind. The relevance of the tracers to the offset analysis is discussed in §3.5.1.

3.4.4 Miscellaneous Differences

Resolution

The offset measurement could be sensitive to the resolution of the data. From Figure 3.1, we can determine that the azimuthal offset is expected to be $5 - 30''$ in angular distance on the sky ($1.5 - 6$ kpc), if a star formation timescale of 10 Myr (E09) is assumed. This range is measurable with the spatial resolutions of the data. On the other hand, if the timescale is 1 Myr as suggested by T08, the spatial resolution required to see offsets would be

$1 - 5$". Therefore, the resolutions of some of the adopted data would be marginal (i.e., 4" in CO, 6" in HI, 1" in Hα, and 6" in 24μm) if Δt is as small as found by T08.

In order to test for a possible resolution dependence, we smooth the Hα data to match the resolution of the 24μm data ($\sim$6") and re-measure the offsets, and find practically no appreciable difference from the measurements at a higher resolution for HI$\rightarrow$Hα and CO$\rightarrow$Hα. A visual comparison of the H$\alpha_{smoothed}$ maps with the 24μm maps shows that the two emissions are very well aligned and trace similar emission sources. The difference in resolution of the SF tracers does not appear to be effecting the measured offset.

We also smooth the CO data to the resolution of the HI data (6") and re-measure the offsets with the SF tracers. Again, we find no significant difference in these measurements with the higher resolution images for CO$\rightarrow$24μm and CO$\rightarrow$Hα. Therefore, the resolution dependence is negligible for the data that we analyzed.

Bin Size

We also test two different radial bin sizes (5" and 2" bins) in measuring offsets. These are the bin sizes used in T08 and E09, respectively. We find little difference between the offset patterns for all four combinations of the tracers; and hence, this is not the cause of the discrepancy.

3.5 Discussion

3.5.1 Nature of Gas and Star Formation Tracers

We found that the most significant cause of the discrepancy between the previous studies is the difference in the gas and star formation tracers used. We also found that CO emission is the best tracer of the compressed gas in spiral arms and that Hα is the best tracer of the associated star forming regions. Thus, they are the most useful for the offset measurement among currently available archival data. The previous studies adopted different tracers for tenable and practical reasons. Here we discuss the advantages and disadvantages of each tracer.

Hα emission is from HII regions around young massive stars whose lifetimes are short ($\lesssim$ 10Myr). There is no doubt that discrete Hα peaks pinpoint the locations of very recent star forming regions. In addition, many

sets of Hα data are readily available in archives, and typically have a higher resolution than the Spitzer 24μm data, another widely-used tracer of star formation. On the other hand, Hα emission could be easily obscured, especially in dense star-forming gas in spiral arms. We might be preferentially finding HII regions far away from the parental gas, biasing the measured offsets toward the large side (T08). This, however, has proved not to be the case. The ability of Hα emission to trace the locations of star forming regions has been shown recently by a comparison of Hα and Paschen α images of M51 (Egusa et al. 2011). Even in the densest regions in a spiral arm, the majority of HII regions, if not all, can be seen in Hα emission, though their fluxes could be significantly attenuated. Hα emission is the best locater of HII regions for offset measurement since their positions are the only parameter required.

The 24μm emission is less sensitive to extinction and might be a better locator of star forming regions that are embedded deeply in a dense star-forming spiral arm. However, it may not be as straightforward a star formation tracer as previously thought, since the emission could be from dust heated by longer-lived, older stellar populations (Liu et al. 2011). In addition, the dust could be heated by the continuum emission longward of the Lyman limit from young stars. The shorter-wavelength emission is mostly absorbed in the vicinity of the young stars and forms HII regions, but the longer-wavelength photons can potentially travel farther and heat up dust not immediately associated with the young stars. If this is the case, the 24μm may not pinpoint sites of recent star formation. The 24μm image is also sensitive to the distributions of both heating sources and the gas/dust. If the gas spiral arm and recently-formed stellar spiral arm are spatially offset (e.g., the stellar arm should be downstream within a corotation radius; Roberts 1969), the young stars may illuminate the gas/dust spiral arm from the front-side and shift the peak of the 24μm emission. There is little doubt that young stars are the dominant source of dust heating around star forming regions, and their discrete appearance is very clear in the 24μm image. However, contamination by the escaped photons from HII regions and the older stellar population could be possibly biasing the offset measurements using 24μm emission to the small side.

A concentration of CO ($J = 1 - 0$) emission is the clearest tracer of dense molecular spiral arms and is aligned perfectly with narrow dust lanes in optical images (Koda et al. 2009). The critical density for collisional excitation of the low-J CO line is high (e.g., $\sim$ a few $\times$ 100 cm^{-3} Scoville & Sanders 1987), and all young star forming regions in the Milky Way are

associated with giant molecular clouds (GMCs), which are bright in CO. There is no doubt that high-resolution CO data show the locations of the gas spiral arms that are being compressed by the spiral density-wave.

It also had seemed reasonable to assume that the HI emission is adequate to locate the enhancements of gas density in a spiral arm (T08 and F11). However, the small, and often zero, offsets of SF tracers from HI, as opposed to the large offsets from CO, are a clear sign that the HI emission peaks are not tracing the compressed gas in the spiral arm. In fact, the HI peaks are almost always at the downstream side of the CO peaks (Figure 3.2 and Figure 3.9). The zero offsets to SF tracers most likely indicate that the HI emission is tracing gas that is photo-dissociated by recent star formation (Allen 2002). (Blitz et al. 2007) showed that GMCs are often found at the peaks of HI emission in the HI-dominated galaxy M33, but there is also more extended HI emission across the galaxy in regions without GMCs. HI peaks may trace locations where the gas will not form into stars. It is remarkable that the fraction of molecular gas does not change azimuthally across spiral arms in M51 (Koda et al. 2009), and therefore the effect of photodissociation is small in terms of the global evolution of the gas phase in the spiral galaxy. However, this small change makes a huge impact in the identification of the HI arm – since overall the abundance of atomic gas is low – and likely caused the discrepancy in the previous studies. Perhaps there is some enhancement of HI emission along the gas spiral arm, but in most cases it is washed out by the stronger emission of the photo-dissociated HI gas, as indicated by the zero/small offsets between HI and SF (T08 and F11). These observational results require a reconsideration of the notion of a short GMC life-cycle, an argument largely based on the offset measurements with HI and 24μm emissions (T08). The offset measurement does not indicate the lifetime of GMCs, since the gas stays mostly molecular even after spiral arm passages and star formation.

Therefore, we conclude that CO and Hα are the best tracers of the compressed gas in spiral arms and the associated star forming regions, respectively. The HI emission does not necessarily trace the compressed, star-forming gas in the spiral arm; instead it traces predominantly the gas photo-dissociated by recent SF. Emission from 24μm could be tracing an older stellar population in addition to areas of recent SF and many not pinpoint the site of SF due to the offsets between the dust and young star distributions.

In this work our discussion of the offset is limited to M51, and we can not make any general conclusion. Nevertheless, our finding that HI traces

the photo-dissociated gas, rather than star-forming dense gas, offers a natural explanation for the general discrepancies in the previous studies. The best combination of tracers (CO and Hα) shows clear spatial offsets and indicates larger, mostly positive offsets than previously suggested using the HI data (T08), although the positive offsets are not ordered as predicted by the standard density-wave theory.

3.5.2 Model Limitations to the Offset Measurement

The offset method is based on only a few assumptions, i e., a constant $\Omega_{\rm p}$ and Δt and pure circular rotation. Its simplicity assures robustness, but has some weaknesses as well. We note and summarize several limitations here which are likely related to the large scatter found in the plots presented above. Some of the limitations come from the model (Equation 1), and the others are from intrinsic location-to-location variations of gas conditions and star formation in spiral arms.

An intrinsic spatial variation of CO and Hα distributions along spiral arms is a source of a systematic error. As discussed in §3.4, the spiral arms are not simple, continuous structures; at small scales they appear as ensembles of more discrete clumps in both CO and Hα images. The spiral arms go back and forth between the downstream and upstream sides, and this wiggling directly affects the offset measurement. The typical amplitude of the wiggle is about 200 pc and contributes to the scatter in Figure 3.6. We should note that this type of error tends to cancel out and does not bias offset values systematically. In addition, the molecular gas shows filamentary structures (or spurs) in the interarm regions at the downstream side of spiral arms (Koda et al. 2009). These interarm structures can potentially limit the offset measurement, especially using the cross-correlation method where such individual structures are neither identified nor rejected in the analysis.

One of the other limitations is the finite lifetime of HII regions. The star formation timescale Δt derived by the previous studies ranges between $\lesssim 3\,$Myr (T08) to $\gtrsim 10\,$Myr (E09).

Some of these timescales are as short as (or less than) the typical lifetime of HII regions ($\sim 10\,$Myr). The derived timescales are meaningful only when they are comparable with or longer than the the lifetime of HII regions. If one obtains a shorter timescale, more careful consideration, such as taking into account the age distribution of HII regions, is necessary before any physical interpretation of the results.

The assumption of a constant pattern speed is commonly adopted, but it is possible that this assumption is not valid. Indeed, it has been suggested that $\Omega_{\rm p}$ changes radially in M51 (Meidt et al. 2008). In particular, the grand-design spiral arms in M51 could be driven by the companion galaxy (NGC 5195). (Oh et al. 2008) discussed, based on theoretical modeling, that Ω_p in tidally-driven spiral arms may vary with radius. The mostly positive offsets that we found in M51 are an indication that the material is flowing through the spiral pattern. Therefore, the spiral needs to be a wave, not a concentration of material. This, however, does not mean that the spiral pattern speed is constant with radius (i.e., the traditional density wave). If the stellar spiral density enhancement lives longer than the gas crossing time, the observed results can be explained without a stationary spiral pattern. Note that the assumption of constant $\Omega_{\rm p}$ has an impact neither on the offset measurement itself nor on our conclusion that the cause of the discrepancy in the previous studies is the choice of tracers.

The circular rotation of galaxies is another assumption that most studies adopt. T08 calculated the directional changes in gas orbits due to the spiral arm potential and concluded that its impact on Δt is very small (i.e., substantially less than a factor of two). Another important factor is the change of the amplitude, not only the direction, of gas velocity due to a symmetric galactic potential. Gas orbits in spiral galaxies are often described as ovals (Wada 1994; Onodera et al. 2004; Koda & Sofue 2006). In an axisymmetric galactic potential the gas moves inward and outward; the speed being a maximum at the points on the semi-minor axis of the orbit, and a minimum on the semi-major axis. Spiral arms form primarily due to this slowdown on the semi-major axis; the gas stays longer on the spiral arms, which leads to the density enhancement. More precisely, the spiral density enhancement occurs even if we do not account for the shock (which produces even more enhancement), and is proportional to the passage times through the spiral structure $t_{\rm cross} \propto 1/(\Omega(r) - \Omega_p)$. $\Omega(r)$, and therefore $t_{\rm cross}$, change substantially during the orbital motion, and can change the surface density in spiral arms by an order of magnitude (Onodera et al. 2004, their figure 11).

To estimate the effect of this slow down to Δt, we estimate a difference in rotational velocities between circular orbits assumed in Eq. (1) and elliptical orbits that form spiral arms.Assuming that the gas is traveling in an elliptical orbit with the eccentricity $e = \sqrt{1 - b^2/a^2}$ (maximum and minimum distances a and b, respectively) and that the galactic potential is isothermal (i.e., flat rotation curve, $\Phi \propto ln(r)$), conservation of energy and angular

momentum provide

$$\frac{v_a}{v_c} = \frac{\Omega_a}{\Omega_c} = \sqrt{\ln(1-e^2)\,\frac{(e^2-1)}{e^2}} \tag{3.3}$$

where v_a is the rotation velocity at the maximum distance a for an elliptical orbit, v_c is the circular rotation velocity at radius a. Ω_a and Ω_c are the angular speeds corresponding to v_a and v_c. For example, assuming an elongated orbit (e = 0.6-0.8), derived pattern speed ($\Omega_{\rm p} = 30\,{\rm km\,s^{-1}\,kpc^{-1}}$), and rotation velocity ($\sim 200\,{\rm km\,s^{-1}}$), $\Delta t \propto 1/(\Omega - \Omega_{\rm p})$ changes from its value under circular rotation by a factor of 2-3 (but up to 10-30) at radii of 4-6 kpc . If the non-circular motion, the very essence of spiral arms, is taken into account, the derived Δt under the assumption of circular rotation is an underestimate by a factor of 2-3. It is important to note that the non-circular motions do not explain the discrepancy in the measured offsets. They affect the interpretation of the azimuthal offsets, but not their measurements. [Note again that the main focus of this study is the measurements.] In order to confirm our simple analytic calculations, we compare the simplistic circular rotation model with the numerical simulations by (Dobbs & Pringle 2010) and F11 that include non-circular motion. We use the offsets measured by F11 between the gas and 100 Myr old clusters in the simulations. The pattern speed of their stationary spiral model is 20 ${\rm km\,s^{-1}\ kpc^{-1}}$ and the rotation curve is roughly flat with a peak velocity of 220 ${\rm km\,s^{-1}}$. We adopt these parameters for our circular rotation model. Figure 3.10 shows the expected offsets for the circular rotation model, Eq. (1), compared to the offset from the numerical simulations. It is clear that the circular rotation model over predicts the offsets by a factor of two in this radius range. Therefore, the gas motion across the spiral arm slows down in the more realistic numerical simulations. The difference is expected to be larger around the co-rotation radius ($\sim$ 11 kpc in this parameter set). These results are consistent with our simple calculation of non-circular orbits. We conclude that the circular rotation model adopted in the previous studies tends to underestimate the SF timescale by a factor of 2-3. Development of an orbit model that fits M51 is beyond the scope of this paper, but this discussion provides a caveat that the Δt derived from the offset method is likely a lower limit of the SF timescale, which could be about an order of magnitude greater when the non-circular motion is taken into account. This could also be evidence against a short GMC lifetime.

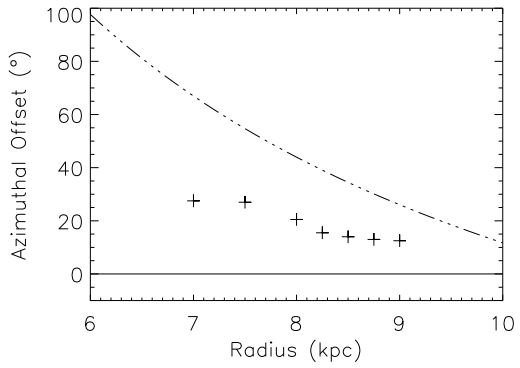

Figure 3.10 Comparison of offsets from two models: the analytical circular rotation model adopted in most offset studies (dash-dotted line) and more realistic numerical simulations using a stationary spiral pattern by (Dobbs & Pringle 2010) and F11 (crosses). The simulations include non-circular motions across spiral arms, and therefore trace any slowdown of gas and stellar motions. The two models adopt the same global pattern speed, Ω_p = 20 $\mathrm{km\,s^{-1}\ kpc^{-1}}$, and a flat rotation curve with a peak velocity of 220 $\mathrm{km\,s^{-1}}$. The offsets are measured between the gas and a 100 Myr-old stellar population. The offsets in the numerical simulations are lower by a factor of ~ 2 than those predicted by the circular rotation model, indicating that the gas and stars slow down considerably during spiral arm passage.

3.6 Summary

The discrepancy found between the previous offset measurements (T08, E09, F11) is significant. E09 found relatively large offsets, which are consistent with the predictions of the density-wave theory and possibly gravitational collapse of the dense gas formed in spiral arms. T08 found offsets an order of magnitude smaller, which would suggest extremely rapid star formation and destruction of giant molecular clouds in a spiral arms (i.e., faster than the free-fall timescale of the gas). Most striking are the non-ordered offsets found by F11, which could argue against the traditional density-wave theory. To elucidate the cause of the discrepancy, we repeated the previous studies using the gas tracer emissions (CO and HI) and SF tracer emissions (Hα and 24μm) and applying the two measurement methods that were developed in the previous studies.

We analyzed the spiral arms in M51 and found that the primary cause of the discrepancy is the use of different gas tracers. In particular, the HI 21 cm line emission traces predominantly the gas photo-dissociated by recently-formed stars, but not necessarily the compressed, star-forming gas in spiral arms. In fact, the HI peaks are almost always at the downstream side of the CO peaks. This explains the small or non-ordered offsets between HI and SF tracers found by T08 and F11 using HI data. It is important to use CO emission to trace the parental gas for SF. In our comparison of CO and Hα emission we found mostly positive spatial offsets with substantial scatter. The positive offsets suggest that there is a density wave and that material is flowing through the spiral arm. However, this may not be a density wave of the simplest form with a single pattern speed. The ability of Hα emission to locate the positions of young star-forming regions (even in very dense environments) has been confirmed previously by (Egusa et al. 2011), although its flux suffers significantly from large dust attenuation.

We compared several other differences in the analyses of the previous studies, and found that nothing but the tracers contribute significantly to the discrepancy. The differences that we compared include those in the offset measurement methods, spatial resolution, and bin size. The dominant cause of the discrepancy is the different choice of the tracers in the previous studies. HI emission does not necessarily trace the sites of compressed gas nor star formation, and contaminated significantly by photodissocation due to young stars.

Chapter 4

Tracing the Unresolved Dense Cores in ISM

HCN and HCO+ are emitted from a dense component of molecular gas which has been observed to be closely related to star formation (Gao & Solomon 2004b; Wu et al. 2005). Previous works have shown a near linear correlation, that spans seven orders of magnitude, between the total infrared luminosity and HCN & HCO+ luminosity. Those relations link Galactic dense cores on parsec scales to spirals and starburst galaxies on kilo-parsec scales. We test these relationships using intermediate points with the dense gas luminosities with our new 400 pc scale single dish observations. We also compare our new higher resolution, 200 pc scale, interferometric maps with the bulk molecular gas and recent star formation.

This Chapter presents the distribution of dense molecular gas, HCN and HCO+, in nearby grand design spiral galaxy M51. In the previous Chapter, the initial and final stages of the gas evolution were examined via the geometrical offsets in M51. Now, we focus on the intermediate stage of gas evolution where dense star forming clumps and cores form within the bulk molecular gas. To do this we use the gas tracers HCN and HCO+ to compare the dense gas component of the ISM with the bulk molecular gas and recent star formation. The HCN and HCO+ distribution has been mapped in the central 7 x 7 kpc made with GBT W-band Receiver and mapped with higher resolution interferometer observations along a region of the western spiral arm using data from the OVRO and CARMA arrays. These data were presented in Chapter 2 but a brief overview of the data is included in this Chapter.

4.1 Introduction

Stars form in the densest parts of molecular gas. In particular, star formation is concentrated in high density ($n \sim 10^4$ cm^{-3}) regions within giant molecular clouds (GMCs) (Lada 1992). These dense star forming regions only represent a few precent of the total GMC mass (Enoch et al. 2007b) and only a small fraction of the total GMC mass actually forms stars. Molecular gas, as oppose to atomic gas, is the main site of star formation (Young & Scoville 1991b). Thus, understanding the formation of these dense pre-star forming clumps is important to understanding the formation of stars.

The most common molecule used to trace the molecular interstellar medium (ISM) is ^{12}CO(1-0) hereafter CO. One popular technique for understanding the relationship between gas and star formation has been through the empirical Kennicutt-Schmitt relationship, which relates the projected star formation surface density to the surface density of gas of HI and H_2 through a power law relationship with an index N - ranging from 1-3(Kennicutt & Evans 2012). Despite its popularity, the Kennicutt-Schmitt relationship only gives the average SFR and gas surface density over a given area. It is not pinpointing the dense regions from which stars forms, especially given the wide ranges of physical scales this relationship is investigated.

In order to probe the dense sites of star formation in the ISM, the molecular gas tracer HCN (1-0) is commonly used to study the dense gas relevant for star formation (Gao & Solomon 2004b, and references, herein). Due to its higher dipole moment, $\mu \sim 3$ D, higher densities are required for collisional excitation of HCN compared to that of CO, $\mu \sim 0.1$ D. Making the expected critical density for excitation of HCN higher than that of CO by 2-3 orders of magnitude from the dependence of μ^3 seen in 1.26. Since HCN emission is only emitted from dense parsec-scale regions of the ISM, it allows for studies of the dense gas without needing to spatially resolve the HCN emitting regions.

Molecular gas, traced by HCN, has been shown to have a linear correlation with star formation in a sample of spiral and (Ultra) Luminous Infrared Galaxies ((U)LIRGS) that is tighter than the correlation with CO (Gao & Solomon 2004b). Multiple studies have since found that there is a tight empirical relationship between the dense gas (HCN (1-0) and HCO+ (1-0), hereafter, HCN and HCO+, respectively) and star formation as traced primarily by total IR luminosity. These studies have ranged from star forming cores in the Milky Way (Wu et al. 2005, 2010; Ma et al. 2013) to single

pointing of spirals and (U)LIRGS (Gao & Solomon 2004b,a; Graciá-Carpio et al. 2008; Juneau et al. 2009). The same linear correlation connects these two completely different scales, MW cores and galaxies. Wu et al. (2005) proposed that this linear correlation can be explained if HCN (and HCO+) are tracing dense clumps where each clump produces a stellar cluster. The presence of HCN and HCO+ would indicate presence of star forming gas. Observations of HCN and HCO+ in nearby galaxies is beginning bridge these two previous scales of observations (Kepley et al. 2014; Usero et al. 2015b) Since this linear relationship spans five orders of magnitude, mapping HCN and HCO+ emission in nearby galaxies is important to test the proposed basic unit of star formation and also probe the physical processes involved with star formation on intermediate scales.

Nearby grand design spiral, M51, provides a testbed to study the dense molecular gas in the context of this correlation, as it is close (8.2 Mpc) and also rich in molecular gas (Koda et al. 2009; Schinnerer et al. 2013). We study M51 in two different aspects. In addition, the presence of young HII regions and stellar clusters along the spiral arms (Lee et al. 2011; Sánchez-Gil et al. 2011) make it an ideal test bed to study the role of dense gas in star formation.

In this Chapter, we study the distribution of HCN and HCO+ in M51 and their relationship with the bulk molecular gas and recent star formation. We begin by showing HCN and HCO+ trace a dense part of the ISM and are, thus, good tracers of dense gas. We discuss our dense gas observations, 400 parsec-scale (pc-scale) single dish observation of the central disk & higher resolution $\sim$ 200 pc-scale interferometric observations along a region of spiral arm, as well as supplement data in §4.2. We continue by presenting the 400 pc-scale observations and the distribution of dense gas in the disk, §4.3. We compare the kinematics between the dense gas with the bulk molecular gas, CO. We test our measurement against the previous relationship between L_{TIR} and the dense gas luminosities. We compare the radial and azimuthal variations of HCN and HCO+ across the disk with CO. In §4.4, we focus on HCN and HCO+ distribution localized along the western spiral arm using interferometry observations at a 200 pc-scale. We qualitatively investigate the bulk molecular gas, as traced by CO, in comparison with the dense gases and looking at local variations in the dense gas fraction compared to Σ_{H_2}. We highlight a region of spiral arm where there is HCN emission present without evidence of recent star formation. Followed by §4.5, where our observations are put in the context of the Wu et al. (2005) postulate, regarding HCN

as a basic unit of star formation. We also consider the effects of local gas conditions and SFE have on the relationships between L_{TIR} and the dense gas luminosities. We conclude with a summary in §4.6.

4.1.1 How 'dense' is the gas HCN and HCO+ are tracing?

The critical density of HCN determined from the Large Velocity Gradient (LVG) approximation calculation can be an order of magnitude lower than if the critical density was determine from only the spontaneous emission coefficient. In order to better understand the density ranges that HCN and HCO+ trace, we utilize this approximation to model the radiation transfer of these molecular lines (Scoville & Solomon 1974; Goldreich & Kwan 1974). This analysis provides a simultaneous analysis of the radiative transfer and excitation of level population. Using the LVG analysis developed for Koda et al. (2012), collision rates obtained from Yang et al. (2010). We determine the expected temperature and density ranges necessary for HCN (1-0) and/or HCO+ (1-0) emission, to quantify a critical density expected for our observations.

The LVG analysis requires as input the molecular abundance and the velocity dispersion associated the the clump. To determine the velocity gradient seen in typical Galactic clumps, we find the typical range of observed line widths and sizes of clumps from Wu et al. (2010). They find a range of line widths of HCN from 3.7 km $s^{-1}$to 5.7 km $s^{-1}$with mean line width is $\Delta v = 3.9 \pm 1.0$ km $s^{-1}$and median value of 3.7 km s^{-1}. Clump sizes range from 0.1 pc to 1.5 pc with mean clump size of 1.13 pc $\pm$ 1.09 and median 0.71 pc. With these values, dv/dr ranges from 2.5 km s^{-1} pc^{-1} to 57 km s^{-1} pc^{-1}. These values are also comparable to the measured properties of HCO+ emission from 303 massive clumps by Barnes et al. (2011). A more recent study of HCN dense clumps conducted using the MALT90 survey, found similar values for size and velocity width (Foster et al. 2011). HCN abundances, X_{HCN}, ranges from $2 - 6 \times 10^{-8}$ relative to H_2 (Loison et al. 2014). Typical HCO abundance, X_{HCO+}, are thought to likely range ranges from $0.5 - 2 \times 10^{-9}$ (Girart et al. 2000). Ionization in the dense star-forming regions are likely responsible for variations in HCO+ abundance based on environment (Papadopoulos 2007). Using these values in the LVG analysis, we determine the expected density ranges traced by HCN and HCO+ emis-

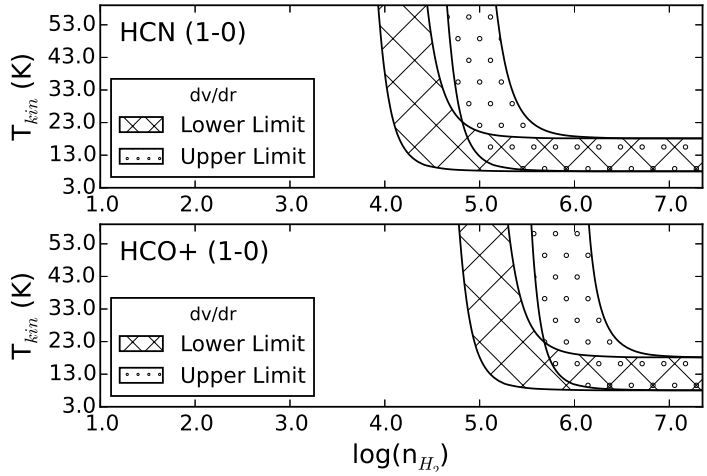

Figure 4.1 The results from our LVG calculation for HCN(top) and HCO+ (bottom). The range of main beam temperatures are plotted as functions of the gas kinetic temperature, T_{kin} and H_2 density, n_{H_2}. The crossed (dotted) curves represent the lowest (highest) values of dv/dr for the range of clump size and line widths from Wu et al. (2010). Typical galactic GMCs have a density of $\log_{10}(n_{H_2}) = 2.5$. The region between the curves represent beam temperatures in a range of 5 - 15 K. The upper bound at 15 K and the lower bound at 5 K for each range of dv/dr.

sion. Figure 4.1 shows the parameters space for T_{kin} and n_{H_2} (HCN (HCO+) in the top (bottom) panel). The shaded regions represent the range of main beam temperatures between 5 - 15 K expected assuming $X_{HCN} = 4 \times 10^{-8}$ and $X_{HCO} = 1 \times 10^{-9}$ and a lower (higher) limit on the velocity gradients of 0.31 km s^{-1} pc^{-1} (8.6 km s^{-1} pc^{-1}) shown as the crossed (dotted) region.

From Figure 4.1, HCN and HCO+ trace densities above 10^4 and 10^5, respectively, independent of temperature. These molecular line emissions must come from a component of the ISM which is denser than the typical bulk GMC environment, which for comparison, have typical $T_{kin} \sim 10\ K$ and $n_{H_2} = 300\ cm^{-3}$ in galactic GMCs (Scoville & Sanders 1987; Solomon et al. 1987) In particular, we can define the critical density, n_{crit} for each of these two molecular transitions as being $n_{crit} \sim 10^4$ cm^{-3} and possibly upwards of 10^5 cm^{-3} under certain physical conditions. The n_{crit} can also be determined

only from the spontaneous emission coefficient,

$$n_{\rm crit} \approx \frac{A_{10}}{\sigma v}. \tag{4.1}$$

For HCN, with an $A \approx 2.0 \times 10^{-5}$ s^{-1}, the critical density can be estimated using $\sigma \sim 10^{-5}$ cm^{-2} and $\nu \approx 10^5$ cm s^{-1} as $n_{\rm crit} \approx 10^5$ cm^3. Likewise, if this is done for HCO+, $A \approx 4.5 \times 10^{-5}$ s^{-1}, a similar $n_{\rm crit}(\sim 10^5$ cm$^{-3})$ is found. With the addition of the escape fraction coefficient, the spontaneous emission coefficient will be replaced with βA$_{10}$, decreasing the critical density (Scoville & Solomon 1974; Goldreich & Kwan 1974).

Both the HCN and HCO+ emission have a weak dependence of the temperature on the emitting regions, the density threshold is much stronger. The critical densities for both of these lines is high and rather independent of temperature. This analysis provides a basis to better understand the gas traced by HCN and HCO+ presented in this work.

4.2 Observations and Data Reduction

4.2.1 Molecular Gas Emission

Single Dish Observations

Observations were made using the W-band receiver and GBT Spectrometer to map HCN (v$_{rest}$=88.63160 GHz) and HCO+ (v$_{rest}$=89.18853 GHz), simultaneously, across the central 3′ x 3′ (7 kpc x 7 kpc) of M51. These observations were made during the 13A and 13B observing semesters (GBT projects 13A_108 and 13B_179). All observations were made using two spectral windows with a bandwidth of 200 MHz each. Details of the observations, such as observation date, weather conditions, aperture efficiencies, system temperatures, are listed in Table 4.1.

The following procedures outline our GBT observing plan. At the start of each observation, holography scans were performed to optimize the dish surface, these were repeated every three hours. Pointing and focusing calibration were made every hour. The receiver gain was calibrating using the hot and cold loads [1]. The mapping scans were made along both the RA and Dec directions. There were four mapping sequence used, two along the RA

[1] http://www.gb.nrao.edu/4mm/

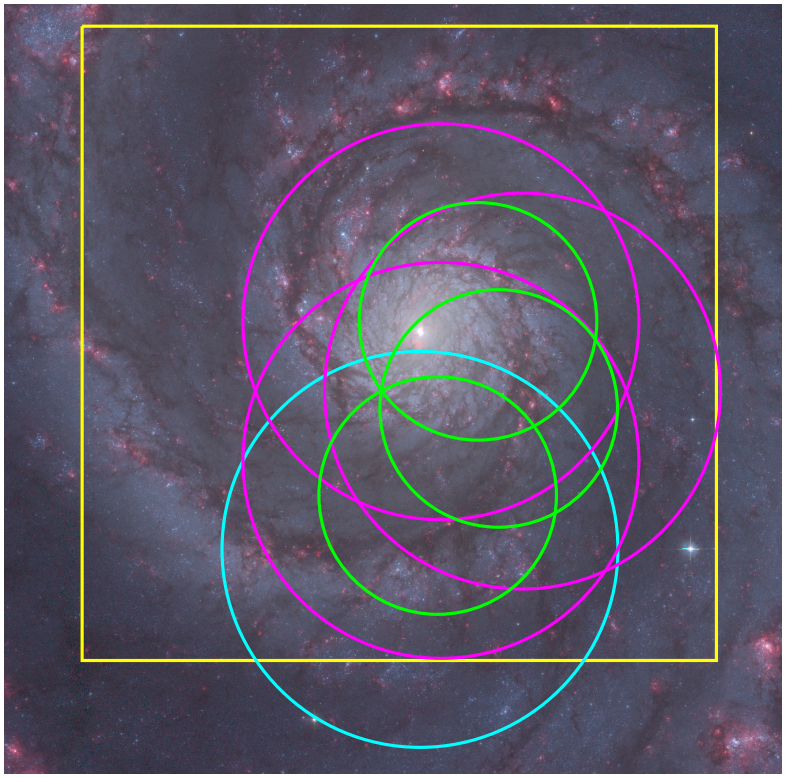

Figure 4.2 Hubble Space Telescope optical composite image of M51. (Blue - 435W, Green - 555W, Red - 658N, Hα.) Plotted on the image are the FOV coverages for the additional millimeter observations of the HCN and HCO+ data presented in this paper. The yellow dashed line represents the FOV coverage the Green Bank Telescope single dish OTF map. The magenta dashed lines show the FOV for the three CARMA C array data pointings. The green dashed lines show the FOV for the three OVRO pointings and the blue dashed line shows the single additional CARMA D array pointing.

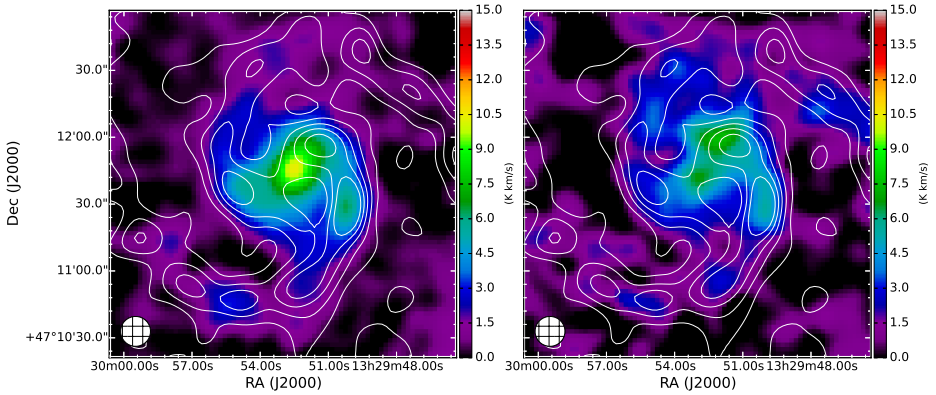

Figure 4.3 Single dish GBT On-the-fly map. Left: Integrated HCN (1-0) intensity map and right: integrated HCO+ (1-0) intensity map. Both figures are shown in units K km s^{-1}. The white contours in both images present the bulk molecular gas as traced by a CO integrated intensity map from (Koda et al. 2009) smoothed to match the resolution of these maps. The beam is shown as a blue circle in the bottom left corner of each of the panels.

direction and two in the Dec direction. Each of the four mapping sequences was used six times, mapping the total region a total of 24 times. The map scans in the same direction were offset by 5″. References observations were made 7.5′ from the top and bottom of the center of map for the Dec scans and 6′ from the right and left of the center map. The "OFF" reference scan for a given "ON" scan was determined by weighting the two adjacent OFF scans based on the relative time taken between the scans. A linear baseline was subtracted from each of the calibrated spectra. Each scan was corrected for the atmospheric opacity using the GBT weather models[2]. The aperture efficiencies were determined from the flux measurement of pointing sources, 1153+495 and 0927+390. The absolute fluxes were found from CARMA CALfind database over the time period of our observations. The aperture efficiencies yielded constant flux densities within each observing semester. Aperture efficiencies were converted to main beam efficiency and was found to vary less for our extended emission.

Maps were generated from the calibrated spectra using the GBT Imaging

[2]http://www.gb.nrao.edu/∼ rmaddale/Weather

Pipeline. The RA and Dec scans were mapped separately and combined using the *NOSTAR*[3] basket-weave procedure to minimize systematic noise resulting from the scan direction. A mask was created from smoothed CO (1-0) (Koda et al. 2009) and HI (Walter et al. 2008) maps. The final cubes have a resolution of 10″ (400 pc) and have spectral resolution of 3.8 km s^{-1} for HCN and 3.3 km s^{-1} for HCO+. The typical noise per channel (T_{mb}) is 54 mK (HCN) and 93 mK (HCO+). For a subset of our observations the system temperatures for the HCO+ observations were significantly higher than HCN, resulting in the increased noise in the HCO+ cube. Integrated intensity maps of both HCN and HCO+ are presented in Figure 4.3. The observing beam is shown in the bottom left corner.

Interferometry

The nucleus and western spiral arm of M51 was mapped in HCN and HCO+ using observations made with the Owens Valley Radio Observatory (OVRO) and, more recently, the Combined Array for Research in Millimeter Astronomy (CARMA). The OVRO observations were made between October 2003 and May 2004. The OVRO array consists of six dishes, each 10m in diameter. A three pointing mosaic was made and the FOV of the pointing are shown as green circles in Figure 4.2. We made HCN (HCO+) channel maps with a synthesized beam of 7″.7x7″.4 (7″.8x7″.5) with a per channel RMS of 6.6 mJy $beam^{-1}$(8.1 mJy $beam^{-1}$) at 6.765 km s^{-1}(6.723 km s^{-1}).

The CARMA observations were made throughout the month of October 2010 in the C array configuration under the project code c0587. The CARMA array consists of the six 10m dishes from the OVRO array and an additional nine 6m dishes from the former Berkeley Illinois Maryland Association (BIMA) array. Baselines varied between 30m and 350m in the C configuration. A three pointing mosaic was observed at the same locations as the previous OVRO observations but with an extended FOV due to the addition of the 6m dishes. The increased FOV and locations of pointings are shown in Figure 4.2 in purple. We made HCN (HCO+) channel maps with a synthesized beam of 2″.4x1x2″.1 (2″.4x2″.1) with a per channel RMS of 6.6 mJy $beam^{-1}$(7.0 mJy $beam^{-1}$) at a velocity resolution of 6.765 km s^{-1}(6.723 km s^{-1}).

[3]NOSTAR, Nobeyama OTF Software Tools for Analysis and Reduction, was developed at NRO.

Table 4.1. Observation details for GBT Data

Date	Obs. Sem	UT	Weather	Calibrator [Jy]	τ	T_{sys} HCN, HCO+	η_{mb} HCN, HCO+
2013-03-22	13A	22:15-7:30	Excellent	0927+390 (4.9) 1153+495 (2.0)	0.07	82, 112	0.25, 0.28
2013-03-23	13A	22:30-6:30	Excellent	1153+495 (2.0)	0.07	79, 110	0.28, 0.32
2013-03-29	13A	22:00-01:00	Excellent	1153+495 (2.0)	0.09	81, 115	0.22, 0.31
2014-01-04	13B	03:00-07:30	Excellent	1153+495 (1.6)	0.08	80, 83	0.23, 0.21
2014-01-13	13B	00:30-05:00	Excellent	1153+495 (1.6)	0.08	92, 91	0.20, 0.15
2014-01-15	13B	23:15-04:00	Poor	1153+495 (1.6)	0.09	90, 91	0.24,0.25
2014-01-17	13B	02:00-08:00	Good	0927+390(4.1) 1153+495(1.6)	0.14	92, 96	0.21,0.23
2014-01-21	13B	01:30-07:30	Good	3C273 (6.0)	0.16	107, 110	0.20,0.18

To extend our FOV to cover more of the spiral arm, we have also included an additional observation from the CARMA array in D configuration obtained December 2013 under the project code c1167. In D array, baselines vary in length from 10m to 150m. This observation was made with a single pointing along the western spiral arm to extend the FOV. The location of this pointed observations can be seen in blue in Figure 4.2. We made HCN (HCO+) channel maps with a synthesized beam of $5''.2$ x $4''.4$ ($5''.3$ x $4''.4$) with a per channel RMS of 1.6 mJy beam^{-1}(2.0 mJy beam^{-1}) at a velocity resolution of 17.6 km s^{-1}(17.5 km s^{-1}). Details of the three different observations can we found in Table 1.

In this Chapter, we present a combined sets of the interferometer data for each dense gas emission line. This combines the OVRO, CARMA C, and D array data but only uses visibilities in range corresponding to the baselines of the D array data, this removes the longer baseline data and can be thought of as a form of smoothing the original OVRO and CARMA C array data. With the addition of the CARMA D array data we wanted to make sure the UV coverage was similar across our extended FOV. Natural weighting as applied when inverting the visibilities. Moment maps were made from the MIRIAD (Sault et al. 1995) package *moment* using a mask made from CO (Koda et al. 2009) and HI (Walter et al. 2008) emission, both smoothed to $20''$. We compare the recovered flux in the region to the single dish map and find that the interferometry maps are recovering $\sim 80\%$ of the flux from the single disk map with the CARMA maps along the spiral arms.

For the HCN (HCO+) channel maps were made using a synthesized beam of $5''.6$ x $5''.5$ at 17.6 km s^{-1}($5''.6$ x $5''.5$ at 17.5 km s^{-1}), the velocity increment of the CARMA D array data. The typical noise levels of the channel maps are 2.2 mJy beam^{-1}(3.3 mJy beam^{-1}). Integrated intensity maps of the low resolution data are presented in Figure 4.4.

We detect significant HCN and HCO+ emission in the central region and along the western spiral arm. For Figure 4.4, CO maps have been smoothed to gridded to match the corresponding set of HCN and HCO+ map. For our analysis in this paper we choice a sensitivity cutoff when the sensitivity has dropped by a factor of 2, this corresponds to the FOV clip of the maps. The HCN and HCO contours in the maps correspond to 3σ, 5σ, 7σ, and 9σ. The CO contours are to help identify the spiral arms. The observing beam is shown in the bottom left corner of each panel.

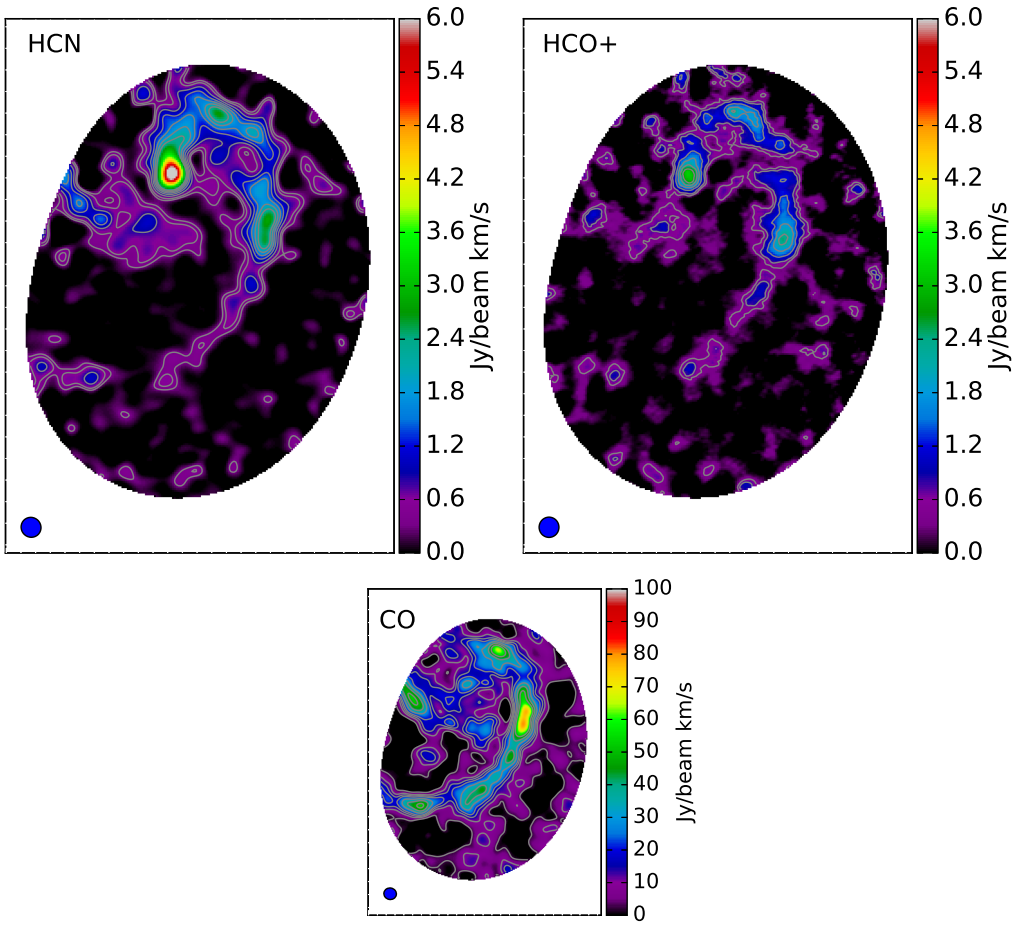

Figure 4.4 Interferometry maps of spiral arm in M51. These maps include the OVRO, CARMA C, and CARMA D data. The FOV coverage of these observations can be seen in Figure 4.2. Left: Integrated HCN (1-0) intensity. Right: Integrated HCO+ (1-0) intensity. Bottom: Integrated CO (1-0) intensity from Koda et al. (2009) smoothed to the resolution of the dense gas tracers. The contours for the HCN and HCO+ panels are multiples (3,5,7,9) of the corresponding to the σ values. The beam size is shown in the bottom left corner for each panel. The images are in units Jy beam^{-1} km s^{-1}.

Table 4.2. Observation Details for Interferometry data

	OVRO	CARMA C	CARMA D
Velocity Increment (km s^{-1})	6.77 (6.72)	6.77 (6.72)	17.6 (17.5)
Synthesized beam (HCN)	7.”7x7.”4	2”.64x2”.3	5.”2x4.”4
Synthesized beam (HCO+)	7.”8x7.”5	2.”4x2.”1	5.”3x4.”4
Total Observation Time (h)	149	28	32
Observation Dates	Oct 2003 - May 2004	Oct 2010	Dec 2013
Pointing Centers (RA, Dec)	13:29:50.75	13:29:52.18	13:29:52.7
	+47:11:24.0	+47:11:45.9	+47:10:48.4
	13:29:51.5	13:29:52.2	
	+47:11:24.0	+47:11:45.9	
	13:29:51.501,	13:29:50.2	
	+47:11:02.0	+47:11:28.4	

4.2.2 IR Emission & Total IR Map

In order to map the total IR luminosity we use the empirical derived relationships from Dale & Helou (2002), which utilizes emission from 24μm, 70μm, and 160μm to determine the total IR luminosity as

$$L_{\rm TIR} = \xi_1 \nu L_\nu(24\mu{\rm m}) + \xi_2 \nu {\rm L}_\nu(70\mu{\rm m}) + \xi_3 \nu {\rm L}_\nu(160\mu{\rm m})[{\rm W}] \quad (4.2)$$

where [ξ_1, ξ_2, ξ_3] = [1.559, 0.7686, 1.347] for a redshift of z=0. This covers the total 3-1100 μm flux for the normal galaxy infrared SED shapes. The IR maps use in this paper to determine the total IR luminosity are from the Herschel Space Observatory and Spitzer Space Telescope. We use the Photodetector Array Camera and Spectrometer (PACS) images from Herschel at 70 μm and 160μm presented in Mentuch Cooper et al. (2012). In addition, we use MIPS 24μm data from Spitzer, that was reprocessed in Bendo et al. (2012). Our treatment of the IR data follows that of Parkin et al. (2013) and we derive a consistent $F_{\rm TIR}$ map before converting it to $L_{\rm TIR}$. The final $L_{\rm TIR}$ map has a resolution of 12″. Previous work studying the correlation between HCN line luminosity and total IR luminosity used the four IRAS bands to measure the total IR luminosity (8-1000 μm) following Sanders & Mirabel (1996).

4.3 Global Distribution of Dense Gas From Single Dish Observations

4.3.1 CO & HCN/HCO+Gas Morphology

The global HCN and HCO+ emission generally follows that of the bulk molecular gas distribution in the disk. Our single dish maps, Figure 4.3, are shown with CO contours, to show the morphology of the bulk molecular gas. The single dish maps show a similar distribution to the HCN maps presented in Kohno et al. (1996) both in the central region, bar, and spiral. There is intense emission of HCN in the central region. There is a similar emission in the central region traced by HCO+, but it is not as strong as what is seen in HCN. The clear enhancement in the center is due to AGN activity, specifically outflowing HCN associated with the jets. This emission is not seen strongly in CO. This enhancement has been seen before Kohno et al. (1996) and the AGN activity was recently analyzed by Matsushita et al. (2015).

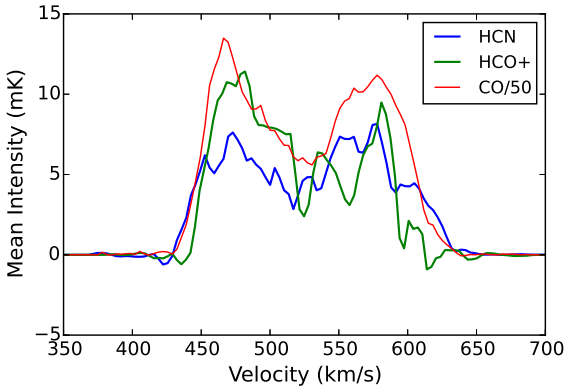

Figure 4.5 Disk averaged intensity of M51 for GBT maps of HCN (blue), HCO+ (green), and CO (1-0) (red) (Koda et al. 2009, 2011). The CO intensity has been divided by 50.

The velocity profile of the disk also matches the bulk molecular gas. The disk averaged intensity profile of the HCN and HCO+ emission are shown in Figure 4.5. The line profiles for the two dense gas tracers agree with CO(1-0) emission from Koda et al. (2009, 2011). These line profiles were made by using a conservative mask of smoothed HI (Walter et al. 2008) and CO (Koda et al. 2009, 2011) to select the regions of each channel associated with this face on disk. The line profiles were smoothed with a boxcar smooth by four channels to a velocity resolution of 15.2 km $s^{-1}$for HCN and 13.2 km $s^{-1}$for HCO+. Since a mask was applied to isolate regions where emission is expected the edge channels do not accurately reflect the noise, but for this spectra was find a SNR of around 4 - 5 for this smoothed spectra.

Along the spiral arm traced by CO contours, both dense gas tracers coincide with the spiral arms, and although the spiral arms are not resolved at this resolution. Both HCN and HCO+ trace the CO spiral arm along the western spiral arm, but HCO+ traces the CO southern spiral arm better than HCN. HCN and HCO+ emission is likely not coming from a diffuse component of the ISM, but from a denser component, $n_{H_2} \geqslant 10^4 cm^{-3}$ associated with the spiral arms.

4.3.2 Dense Gas Luminosity and L_{IR} Comparisons

Understanding the relationships between HCN, HCO+, and star formation on a global scale is important to studying the evolution of the ISM. Previous work has shown a near linear correlation between the total infrared luminosity and dense gas tracer luminosities between Galactic dense clumps and spiral and starburst galaxies (Gao & Solomon 2004b; Wu et al. 2005, 2010; Ma et al. 2013). The L_{TIR} can be used to probe the star formation rate (SFR). There is a relationship spanning nine-orders of magnitude between the galactic and extragalactic measurements, however there is a three order of magnitude gap separating the groups of measurements. This gap corresponds to $\sim$ kpc-scale resolution. To investigate this gap using M51, we have smoothed the GBT HCN and HCO+ images to the resolution of the L_{TIR} map. We regrid the images to the same coordinate system and binned all the maps such that each pixel represents an individual resolution element ($12''$). The luminosities of the dense gas tracers were found by multiplying the line intensities of a pixel by the pixel area. Pixels with less than 3σ were not included in this analysis.

In Figure 4.6, we show the relationship between the total infrared luminosity, L_{TIR}, and the dense gas map L_{HCN} & L_{HCO+} on a log-log plot for the disk of M51. The results for HCN are shown on the left panel and the HCO results are shown on the right panel. In addition to the results for M51, we include additional data from galactic observations Wu et al. (2010, HCN) and Ma et al. (2013, HCO+), extragalactic observations (Graciá-Carpio et al. 2008; García-Burillo et al. 2012; Juneau et al. 2009, HCN & HCO+) and observations in nearby M82 (Kepley et al. 2014, HCN & HCO+). The data points corresponding to the central nuclear emission have been removed.

For the disk of M51, the relationship between L_{HCN} and L_{TIR} shows a positive correlation. A similar trend is seen with HCO+. The relationships found by Wu et al. (2005) and Ma et al. (2013) fitting for both galactic and extragalactic observations are shown as dashed line for HCN and HCO+, respectively. In addition, we show the LIRG/ULIRG relationships from (Graciá-Carpio et al. 2008) for both HCN and HCO+, dotted line. The points in M51 lie below the LIRG/ULIRG relationship suggesting that M51 has a lower SFR than the ULIRG star bursting environments (Graciá-Carpio et al. 2008; García-Burillo et al. 2012). Similar trends are seen between L_{HCO+} and L_{TIR}.

The points in M51 deviate from the Wu et al. (2005) relationship by a factor of 3. In addition, the points for M51 are offset from what was seen in

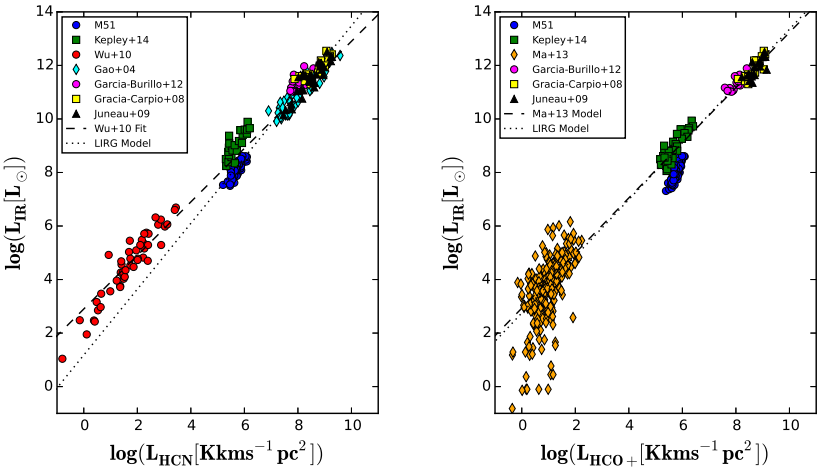

Figure 4.6 L_{TIR} and L_{HCN} (left) and L_{HCO+} (right). Spiral Arm points for M51 are shown in blue circles. In addition, we include galactic observations Wu et al. (2010, HCN) and Ma et al. (2013, HCO+), extragalactic observations Graciá-Carpio et al. (2008); García-Burillo et al. (2012); Juneau et al. (2009, HCN & HCO+) and observations in nearby M82 Kepley et al. (2014, HCN & HCO+). The dashed line shows the fits from Wu et al. (2010, HCN) and Ma et al. (2013, HCO+) and the correspondings fits for ULIRGS from (García-Burillo et al. 2012) are shown as a a dotted line. Both axes are plotted on a log scale. The measurements of the dense gas along spiral arm line along the same linear correlation as the galactic cores, spirals, and starbursts over eight orders of magnitude with some scatter. The central points associated with the XDR region have been removed.

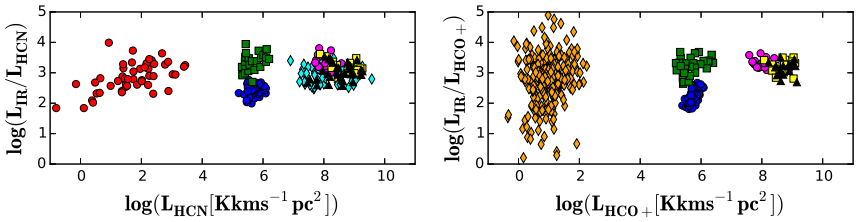

Figure 4.7 L_{TIR}/L_{HCN} and L_{HCN} (left) and L_{LIR}/L_{HCO+} and L_{HCO+} (right). Both axes are plotted on a log scale.The points have the same labeling and color scheme as the points in Figure 4.6.

M82 (Kepley et al. 2014), an offset of 0.5 dex. We are confident that this offset is real and not due to a calibration error. Our observations are consistent with those of HCN from single pointing. Kepley et al. (2014) did a similar check with their M82 data. As an addition check, we reduced archival data from Kepley et al. (2014) and are able to reproduce the offset. We explore possible causes of this offset in 4.6. Specifically, if additional factors play a role in determine the star formation efficiency or mass to light ratio. Kepley et al. (2014) found radial gradient within the deviations from the relationship for HCN and TIR in M82 suggesting there are intrinsic variations . These intrinsic variations may also explain the spread of measurements found by Ma et al. (2013).

To further investigate the SFR over our range of dense gas luminosities, Figure 4.7 shows, the ratio of L_{IR} to each dense gas luminosity. This ratio plots shows more into the deviations seen in the slope of the relationship in Figure 4.6. L_{IR} is a proxy of SFR and likewise, if the dense gas luminosities can each be thought of as being proportional to the dense gas mass. By looking at the ratio of the two we can probe a star formation efficiency for dense gas, SFE_{dense}. Figure 4.7 allows a better look at the spread of the points and more importantly, the scatter around the near linear relationships from Wu et al. (2005, 2010) and Ma et al. (2013), for HCN and HCO+, respectfully. The smallest amount of deviations exist for the extragalactic single pointing observations with increasing spread in the distribution of points down to the smallest scales shown in this plot.

The ratio L_{TIR}/L_{HCN}, should be constant if there is a linear correlation

between dense gas and star formation rate. This spread could be due to variations in the SFE_{dense} . In a sample of LIRGs and ULIRGS, Graciá-Carpio et al. (2008) finds that the L_{TIR}/L_{HCN} is not constant, as they find a superlinear relationship between L_{HCN} and L_{IR}, similar to seen at observations at higher redshift (Wu et al. 2005). GMCs in M33 also show some of the highest L_{IR}/L_{HCN} ratios observed, comparable with the ratios measured in ULIRGS and high-z galaxies (Buchbender et al. 2013). This suggests a dramatic change in SFE_{dense} giving more evidence that SFE may be changing in environments. If LIRGS and ULIRGS are probing starbursting galaxies, this may contribute to some of the variations compared to local normal star forming regions. In addition, could explain why observations of M82 lie above those for M51.

4.3.3 Variations in HCN and HCO+ across the disk

The radial distribution of the dense gas within the disk can help to distinguish between various physical processes responsible for the emission of dense gas. Specifically, if the dense gas emission is being excited due to the AGN and activity in the XDR or via star forming processes in PDR regions along spiral arms. The central region of M51 that our GBT observations cover include the star forming spiral arms, bar, and Seyfert 2 nucleus (Ho et al. 1997). The distribution seen in Figure 4.4 shows variations between the dense molecular gas and the bulk molecular gas traced by CO, specifically in the central region.

Figure 4.8 shows the radial distribution of the HCN/CO and HCO+/ CO brightness ratio. The central 400 pc shows an increase in the value of the dense gas ratio with both traces, the largest being with HCN. This increased ratio value is also seen in Kohno et al. (1996). Both ratio values continue to decrease with increasing ratios, but the change is gradual compared to the values in the central regions. These ratios are the average in a radial annuli, there will be some azimuthal variation between arm and interarm regions that are not captured in this plot. In addition to looking the brightness ratio between the dense gas and the bulk molecular gas, we also consider the brightness ratio of HCN/HCO+. From Figure 4.9, HCN emission is elevated above 1 in the central region and the bar regions. In the region dominated by the spiral arms, the HCN/HCO+ ratio is less than one. Along two IRAM single pointing observations along the spiral arm in M51 by Watanabe et al. (2014) find similar intensity between HCN and HCO+, suggesting ratio of

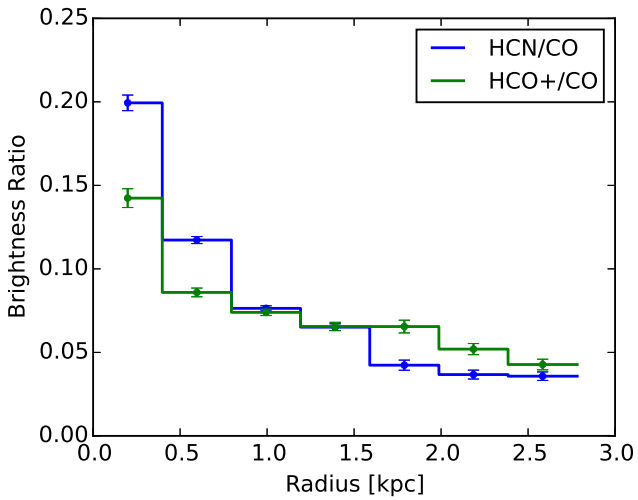

Figure 4.8 Brightness Ratio of dense gas tracers, HCN (blue) and HCO+ (green) with CO as a function of radial distance in M51. The ratio is averaged in 400 pc annuli.

near unity. It should be noted that our observations are radial profiles, where as the IRAM observations are isolated along spiral arms. Recent ALMA observations of NGC 253, find slightly elevated HCN/HCO+ ratio above unity in the central region but find value near unity with little change across the disk (Meier et al. 2015). These results are similar to our measurements across the disk in M51.

In addition to the radial variations seen across the central regions of M51, we also investigate the variations between spiral arm and interarm in the disk. In order to determine the azimuthal variations across the disk, we fit a logarithmic spiral pattern to the spiral arms in M51 using the CO integrated emission. This logarithmic spiral pattern can be seen in Figure 4.10 (right) in the white line. We bin the disk according to this logarithmic spiral pattern in 30° bin, shown in Figure 4.10 traced in green. The center AGN and bar regions are excluded from this analysis. The azimuthal binned averages are shown in Figure 4.10 (left), HCN/CO average is plotted on top and HCO+/CO average is plotted on the bottom of the panel. The phase angle is defined counterclockwise from the white spiral line, therefore the angle increases in the direction of gas flow. The two sets of blue and red

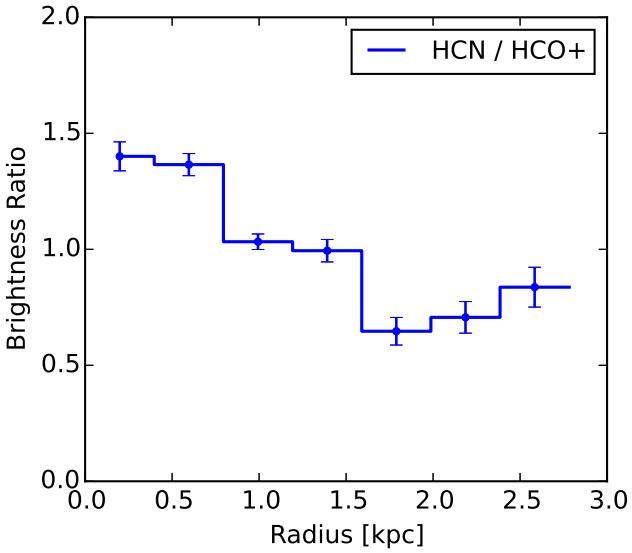

Figure 4.9 Brightness Ratio of HCN and HCO+ as a function of radial distance in M51. The ratio is averaged in 400 pc annuli.

lines, represent a trace of the upstream and downstream sides of the spiral arm, respectively, and are shown in Figure 4.10.

From Figure 4.10 we can see that HCO+/CO ratio has some variation across spiral arm. The HCO+/CO ratio is increased along the spiral arms compared to the interarm regions. As a dense gas tracer, increases in the HCO+/CO ratio implies that there is an increase of dense gas along spiral arms. If this dense gas is the precursor to star formation, this may suggests that the spiral arms create conditions under which more dense gas develops, and thus more star formation occurs. There is a hint of a trend seen in the HCN/CO ratio. However, due to our sensitivity limits, we can not determine with certainty, if HCN/CO ratio varies between spiral arm and interarm regions.

To increase the SNR in the regions along the disk, we divide the disk into three regions: spiral arm, interarm, and center. Using this region map, Figure 4.11, we determine the HCN/CO and HCO+/CO ratios between the arm and interarm region. We do not include the central region in this analysis, as it has previously been explored in the radial profiles. Along the spiral arm regions, we find an average HCN/CO of 1.1 ± 0.1 and in the interarm regions

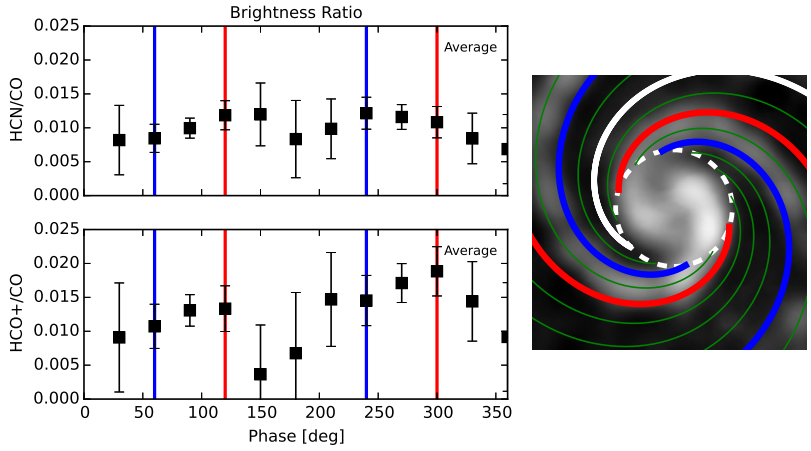

Figure 4.10 Left: Average brightness ratio of HCN (top) and HCO+ (bottom) compared to CO. The data is averaged of 30 logatermic spiral pattern fit to the spiral arms of M51. The blue and red regions, represent the upstream and downstream sides of the spiral arms. The phase is defined such that the gas flow direction is in the same direction as the increasing phase. Right: CO integrated intensity map used as a reference to show the defined spiral pattern from which the data was binned. The white line shows the location where the phase is defined as zero. The blue and red lines, show the edges of the spiral arm bins seen in the plots on the left. The green lines show 30° phase bins. The central region inside the dotted white line is executed from these averages.

the HCN/CO ratiois 0.78 ± 0.45. Compared to HCO+/CO, the spiral arm ratio value has an average of 1.5 ± 0.2 and an upper limit can be placed in the interarm regions of ¡0.7. There is a clear difference between the arm and interarm regions in HCO+/CO, but it is still not possible to say that the HCN/CO ratio varies between the arm and interarm regions.

4.4 High Resolution Distribution Along Spiral Arm of Dense Gas

To further study the formation of dense gas, we focus on the dense gas at higher resolution along the spiral arm, where the single dish maps showed

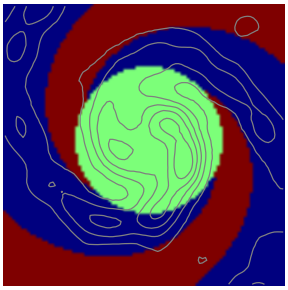

Figure 4.11 Map of the defined regions of the disk. The blue regions are defined as associated with the spiral arms and the red regions are defined as interarm regions. The central region is shown in green and is excluded from either the spiral arm or interarm regions. CO integrated intensity contours are overplotted as a reference.

the emission to be localized. In order to better study how the dense gas is distributed along the spiral arm, we look at the higher resolution CARMA data. In Figures 4.12 and 4.13 we show the velocity channel maps of the HCN and HCO emission, respectively. The contours start at a 3σ detection then increase at 2σ intervals. The contours are plotted on CO emission smoothed to match the spatial resolution of the HCN and HCO+ channel maps. The CO was also regrid to match the HCN and HCO+ channel resolution. The spiral arms are traced out at 3σ structures between the different velocity channels and allow for definition of the spiral arms in both HCN and HCO+ emission. These channel maps show the dense gas emission along western spiral arm. Both HCN and HCO+ appear coincident with the CO spiral arms throughout the channels.

The dense gas emissions typically appears along the peaks of the CO emission. There does not appear to be any offset between channel maps between the dense gas and the bulk molecular gas at this velocity resolution. Typical spiral arm velocity width in this region of M51 appears to be ~ 50 km s^{-1}, as seen in bulk molecular gas maps (Koda et al. 2009).

The HCN and HCO+ peaks appear in the same locations as the peaks in CO emission. LIke seen with the global single dish map, the main difference is in the central region, where the HCN and HCO+ emission is bright. There is a large concentration of HCN (and HCO+ to a lesser extent) in the central

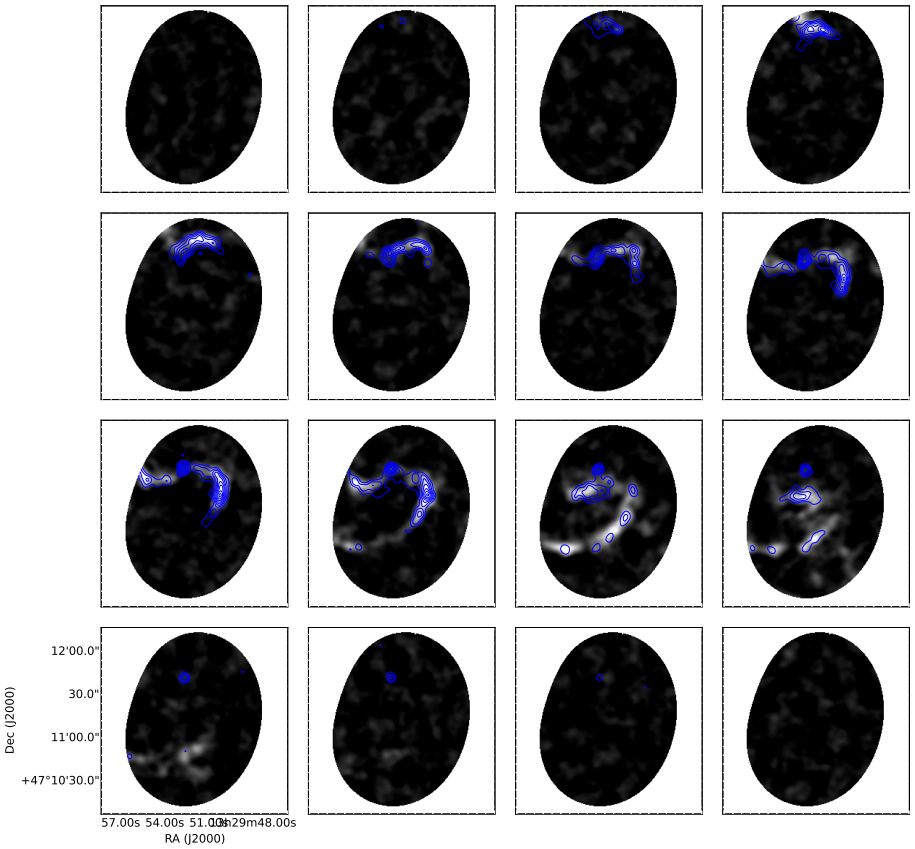

Figure 4.12 Contour channel maps of HCN emission overplotted on CO maps from Koda et al. (2009, 2011) smoothed to match the resolution of HCN emission and regridded to match the 17.6 km/s channel resolution.

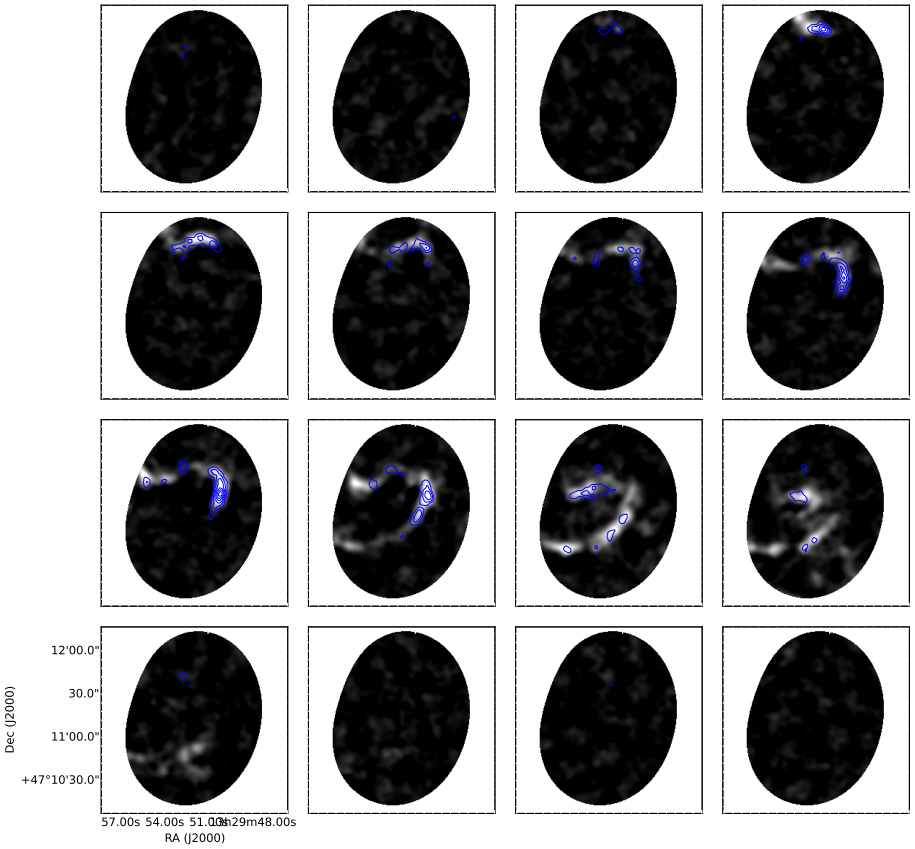

Figure 4.13 Same as Figure 4.12 but for HCO+

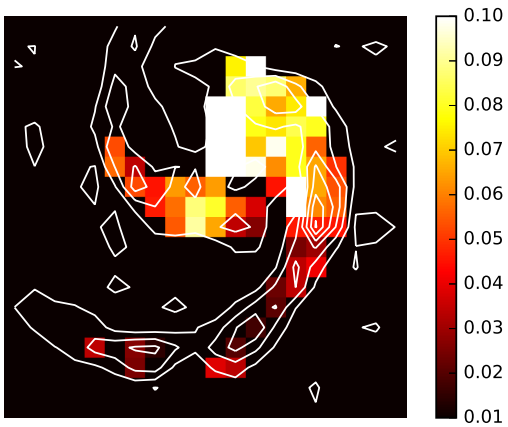

Figure 4.14 Map of the dense gas mass fraction along the western spiral arm in M51. CO Contours are plotted in white to show the location of the bulk molecular spiral arm. No clear evidence of offset or increasing dense gas mass fraction towards the downstream side of the spiral arm.

region, which is quite different from that of the CO emission. This feature was also seen in Nguyen et al. (1992b) and Kohno et al. (1996). There is an asymmetry along the bar ends, which is seen in all three tracers. There are some differences between the HCN and HCO+ emission along the spiral arm, but overall the emission is quite similar and the peaks are located at similar positions.

4.4.1 Dense Gas Fraction Across the Disk

Variations between dense gas and bulk gas, can help probe different physical conditions that exist across the disk in M51. As opposed to radial profiles, we now consider ratio values across the disk at higher resolution. Along the spiral arms we are recovering 80% of the flux with our CARMA maps and therefore use our higher resolution CARMA maps to look at changes in the dense gas fraction along the spiral arm. Specifically, we want to understand what variations exist across spiral arm that may impact the star formation seen associated with spiral arms.

Figure 4.14 shows the dense gas emission fraction, I_{HCN} / I_{CO}, with CO

contours over plotted.This figure is scaled to focus on the variations in dense gas emission fractions across the spiral arms. The fraction is seen in the central region are ~ 0.4. In addition, the build up of gas along the bar ends leads to an increase of surface density and also the intensity fraction around 0.2. We find along spiral arms the intensity fraction is ≤ 0.1. We find ratio values consistent with Helfer & Blitz (1993) measurements in M51. No clear evidence of offset or increasing dense gas mass fraction towards the downstream side of the spiral arm. There is some variation along the spiral arm in dense gas emission fraction. The dense gas mass fraction varies between 0.03 and 0.05. The highest dense gas fraction regions do not necessarily appear on top of locations with the most CO emission, although they do appear in the spiral arm traced by the bulk molecular gas.

To help understand the role of the bulk molecular gas environment to the formation of dense molecular we want to see if there is any relationship between $\Sigma_{\rm H_2}$ and the molecular dense gas mass fraction ($\rm M_{dense}/M_{H_2}$). The mass of molecular gas can be derived using the CO luminosity from a CO-to-H_2 conversion factor, typically known as $\alpha_{\rm CO}$. The mass of molecular gas as determined for the Milky Way Bolatto et al. (2013) can be written as

$$\rm M(H_2) = 4.3\ L_{CO}\ M_{\odot}(K\ km\ s^{-1}\ pc^2)^{-1}. \tag{4.3}$$

To determine the molecular *dense* gas mass we follow the same procedure as Gao & Solomon (2004b) and determine $\rm M_{dense}$ from the conditions within a virialized cloud core with average density $\rm n_{H_2}$ = 3 x 10^4 $\rm cm^{-3}$ and $T_{\rm b} \sim$ 35K (Radford et al. 1991).

$$\rm M_{dense}(H_2) \approx 2.1 \frac{\langle n_{H_2} \rangle^{1/2}}{T_b} L_{HCN} \tag{4.4}$$

$$\sim 10\ \rm L_{HCN}\ M_{\odot}(K\ km\ s^{-1}\ pc^2)^{-1} \tag{4.5}$$

In the discussion, we consider variations in the conversion factor from $\rm L_{HCN}$ to $\rm M_{dense}$. However, here we continue in this section assuming a constant conversion factor.

We compare the molecular dense gas mass fraction with the surface density in Figure 4.15. There does not appear to be any strong correlation with changes in $\Sigma_{\rm H_2}$. The outlier points that correspond to the highest dense gas fraction are located in the central AGN region and near the bar ends. Dense gas emissions appear along the spiral arm coincident with CO emission, but

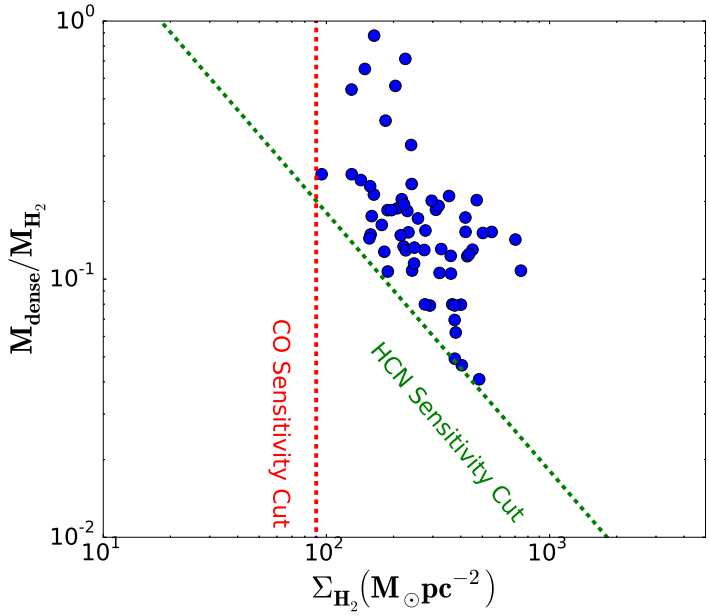

Figure 4.15 Plot of the dense gas mass fraction verse surface density, Σ_{H_2}. CO sensitivity limit is shown in red and the HCN sensitivity limit is shown in green. There is no clear evidence of increasing dense gas fraction with increasing Σ_{H_2}.

the regions with the highest surface density do not correspond with the regions of highest dense gas fraction, similar to what was seen in Figure 4.14. However, given our sensitivity limits, no statement came be made about the existence of a trend between surface density and dense gas fraction, or more generally the conditions required for the formation of dense gas.

4.4.2 Comparison with Recent Star Formation

Dense gas tracer emissions from HCN and HCO+ are thought to be precursors to star formation (Gao & Solomon 2004a). In Figure 4.16, we compare the integrated intensity maps of HCN (right) and CO (left) with recent star formation tracer, Hα. The contours show the molecular gas emissions. The dense gas emission falls along the dust lanes, suggesting that it embedded in the optically think bulk molecular spiral arm. At the HCN emission peaks

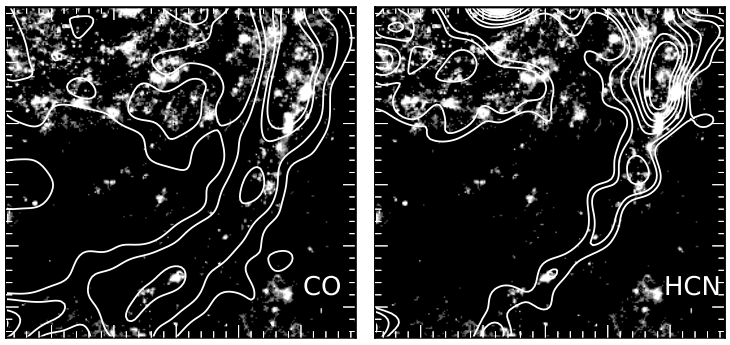

Figure 4.16 Comparison of molecular gas emission, CO (left) and HCN (right) with Hα. Localized along a region of the spiral arm where there are low levels of HCN emission but there is no high mass star formation.

there is always evidence of recent massive star formation, as traced by Hα. In addition to the HCN emission peaks, there is lower levels of emission present along the spiral arms that do not correspond to the massive star formation traced by Hα.

A region along the western spiral arm in M51 has recently been highlighted by (Meidt et al. 2013) as having high CO surface density, but lacking corresponding recent star formation. This region although do not show much evidence of massive star formation, as traced by Hα, does not appear to vary from the global trend seen for M51 in the L_{IR} - L_{HCN} relationship. This region which shows different behavior between the bulk molecular gas, traced but CO, does not appear unique when compared to the rest of the measurements across the disk. This is supported by the variations that are seen in the dense gas ratio in this same region of spiral arm, see Figure 4.14.

4.5 Discussion

4.5.1 HCN as a tracer of a basic unit of star formation

A correlation does exist between L_{HCN} and L_{IR} but there is factor of 3 deviation of the M51 points from the Wu et al. (2005) fit, and this deviation is significant. This offset is larger than what is found by extrapolating the deviation in clump properties from Wu et al. (2005) to the deviation in simul-

taneous observations of multiple dense clumps at our intermediate kpc scale regions. In addition, the measurements in M82 and M51, which are both taken on similar spatial scales, are systematically offset from one another by 0.5 dex. Both of these observed characteristics, the deviation and the offset, need to be explained in the context of the L_{HCN} and L_{IR} correlation. We propose the following update: the primary factor in determining the relationship between HCN and IR luminosity is due to HCN tracing a basic unit of star formation, as was proposed by Wu et al. (2005). In addition, there is a secondary factor that causes some deviation around the correlation. Specifically, this secondary factor is likely caused by conditions within the ISM.

The deviation and offset among the observations, may suggest that global environment plays a role that has secondary effects on the correlation. Our measures in M51, span over $\sim$ 7kpc and the measurements are correlated and a similar correlation is seen in M82 Kepley et al. (2014). The large dynamical range of both measurements, suggests the global environment may be responsible for the deviations in the basic unit of star formation, IR-HCN correlation. For a single global environment, like an individual galaxy, the deviation in clump properties is small, but may have a larger variation between environments, this may explain what is seen between M51, M82, and the expected offset from Milky Way observations. Both M51 and M82 are molecularly rich, compared to the Milky Way and there are large differences in the global environment of the galaxies, M82 is a starbursting galaxy (Rieke et al. 1980) and M51 has a companion which can trigger a strong density wave. M82 is a starbursting environment where as M51 is an AGN environment. Variations exist in line ratios between M82 and M51, along with other nearby galaxies, from multi-line single dish studies (Krips et al. 2008). GMCs properties have been shown to vary in these two galaxies vary from those of the Milky Way (Hughes et al. 2013; Keto et al. 2005). GMCs in M51 tend to be brighter and larger with higher velocity dispersions compared to the GMCs in the Milky Way (Hughes et al. 2013). Observations of the clouds in the starburst environment of M82 suggest that star formation efficiency might change with cloud sizes which may imply different modes of star formation for GMCs that are different than what is present in the Milky Way (Keto et al. 2005). Clear environmental differences exist between these galaxies, it is important to understand how these differences effect the L_{HCN} and L_{IR} relationship and modes of star formation.

We consider three possible explanations for the offset and the deviation.

The first of these is related to variations in the mass to light ratio. If these conversation factors from luminosity vary across environment, it is likely that some scatter would exist. Since we can not directly measure the mass or the SFR, assumptions must be made on how and if the environment effect those conversions. The second possibility, is that there are intrinsic variations in the SFE_{dense}. Despite the gas traced by HCN being at a large, and similar, density, addition factors that influence the conditions in the ISM could promotion or hindering star formation. Overall, the SFE_{dense} may be similar, particularly on global scales, their may likely be some scatters. Lastly, there could be some combination of both of these effects adding to intrinsic deviations and offsets causing the secondary deviations. We discuss the possibility of mass to light and SFE variations separately, below. If the secondary deviations are due to the conditions of the gas, impacting either SFE or the mass to light ratio, it may explain the offsets and deviations from the linear relation and the factor of 3 does not degrade HCN as a tracer of a unit of star formation.

4.5.2 Variations in Mass (and SFR) to Light Conversion

The basic unit of star formation could be interpreted as a constant mass to light ratio for HCN and a constant SFR to light ratio for IR tracers. The presence of the offset of the M51 data could be explained if secondary effects create scatter in the mass to light conversion. We explore this possibility that the conversion factors vary based on simple gas physical conditions to explain the secondary effects resulting in the observed scatter. We seek to determine the dependence of physical parameters on a mass (SFR) to light conversion factor for HCN (IR) emission, such that, $L_{HCN} = \alpha M_{dense}$ and $L_{TIR} = \beta SFR$. Typically it was believed that α and β were constant. However, it is likely that α and β are variable and depending on the local environmental conditions, like temperature or turbulence.

Simple Model of the Mass to Light Conversion for HCN

We begin by looking at the HCN mass to light conversion factor, which would affect the points on the x-axis of Figure 4.6. The luminosity of optically thick HCN can be written as

$$L_{HCN} \propto R^2 T \sigma \tag{4.6}$$

where R is the core radius, T is the temperature of the core, and σ is the velocity dispersion of the core, which can be measured for individual cores in the galaxy. To determine the mass to light ratio, assume the mass mass of a dense core is in virial equilibrium. Given a core in virial equilibrium, the mass can be written in term of R and σ as

$$\mathrm{M_{VT}} \propto \mathrm{R}\sigma^2 \tag{4.7}$$

In order to determine the dependence of the conversion factor, take the ratio of the mass and luminosity to obtain the following,

$$\frac{\mathrm{M_{VT}}}{\mathrm{L}} \propto \frac{\mathrm{R}\sigma^2}{\mathrm{R^2T}\sigma} = \frac{\sigma}{\mathrm{RT}}. \tag{4.8}$$

Next, assume that σ is set by the turbulence. Turbulence, whether dictated by galactic dynamics, stellar feedback, etc., can be related to R, $\sigma \propto R^{1/2}$. The assumption of the turbulent relationship between R and σ may not be accurate on scales where gravitational forces dominate over turbulence but there is good agreement on a relationship between turbulence and size, spanning down to 0.1 pc (Kennicutt & Evans 2012) which is the range of the HCN emitting dense cores from Wu et al. (2010). It should be note, in observations of the galactic ISM cores, $\sigma \propto R^{1/3}$ may be better fit the observed data (Falgarone et al. 2009). Using the relationship between R and σ the conversion factor can be rewritten as:

$$\frac{M_{\mathrm{VT}}}{L} \propto \frac{\sigma}{\sigma^2 T} = \frac{1}{\sigma T}. \tag{4.9}$$

If this was written in terms of ρ instead of σ, this would have the same form as Equation 4.4. Both T and σ could contribute in setting the mass-to-light conversion factor for HCN. Warmer regions would have a smaller conversion factor. A similar result can be said for σ, more turbulent regions, will result in smaller conversion factors. If the scatter in the conversion factor comes from the dependence on velocity dispersion and temperature, it may be explain the scatter from the linear correlation. Considering the typical core σ from Wu et al. (2010), σ varies by a factor of two. This would correspond to the conversion factor varying by a similar factor of two to four for the virial mass conversion factor. This range could easily explain the offset or scatter of our points from the linear correlation. Specifically, the warmer or more turbulent the ISM, the smaller the mass to light ratio. This simple interpretation show

how the physical conditions in the ISM may explain observational variations in the mass to light ratio, and thus, be a model for the secondary effects in the basic unit of star formation interpretation.

Simple Model of the SFR to Light Conversion for IR emission

To relate IR luminosity to SFR, consider that the SFR is probed by the emission from dust that has been heated by recent star formation. This would affect only the y-axis of Figure 4.6. Measuring the IR emission, is probing the intensity. In the simplest form, intensity can be written as,

$$SFR \propto I \propto \alpha B(T)(1 - e^{-\tau}). \tag{4.10}$$

The dust being probed in the IR emission, in the simplest model can be determined from a single temperature blackbody, $B(T)$. In addition, there may be a filling factor term, α but we will treat this as a constant for our argument. For τ values that are much less than one, the intensity can be rewritten

$$SFR \propto I \propto B(T)\tau. \tag{4.11}$$

The optical depth, represents the emissivity, κ, multiplied by the dust column density $\Sigma_{\rm dust}$. Using the Rayleigh-Jean approximation, $B(T) \sim$ T, although at the wavelengths probed by Spitzer, this might not be the most accurate approximation, SFR becomes,

$$SFR \propto I \propto \alpha T \Sigma_{\rm dust}. \tag{4.12}$$

In this simplified model, the intensity, and thus, the SFR becomes a function of the temperature and the density of the dust. The four possible cases depending on high or low temperature and/or density may explain some of the scatter and offset present in Figure 4.6. In addition, the age, current star formation, and older stellar population may also influence the conversion from IR luminosity to SFR.

We want to determine if these conversion factors can explain the offset seen with our observations. We apply the conversions explained above to determine if an offset is expected between M51 and M82, as well as an offset of M51 from the original Wu et al. (2005) relationship, derived in part by Milky Way ISM conditions, we can determine the likelihood that our observed offset is due to a M/L conversion factor. Considering the local GMCs properties in M51 and M82, both galaxies tend to have GMCs that are larger and brighter

than the GMCs in the Milky Way (Keto et al. 2005; Hughes et al. 2013). This could explain an offset if both M51 and M82 had similar offsets from the original relationship, but this does not seem to explain the offset of M51. We have determined two conversion factors that can depend on the physical conditions within the ISM. Although this simple example *could* explain an empirical offset based on T and σ, as discussed above, it does not seem likely that the offsets seen in regards to the measurements made in M51 are solely based on a M/L conversion.

4.5.3 Variations in Star Formation Efficiency

Deviations from the linear correlation, like the factor of 3 offset seen in the M51 data, could be caused due to variations in the $\mathrm{SFE_{dense}}$. In the basic unit of star formation interpretation, a lower SFE could be explained by simply having dense clumps below the mass threshold proposed by Wu et al. (2005). If the clumps are less massive, there is not enough IR emission compared to clumps with masses high enough to produce massive stars, fully sampling the IMF. This explanation would require the dense star forming clumps in M51 to be smaller and not form the massive stars expected in the more massive clumps.

A second possibility, is that the $\mathrm{SFE_{dense}}$ varies between galaxies. Having $\mathrm{SFE_{dense}}$ that varied between galaxies, could explain the offset between M82 and M51, specifically, if the central starbursting region of M82 had an influence on SFE. In this case, the star formation in M51 would represent disk-mode star formation, whereas, M82, specifically the central region mapped in Kepley et al. (2014), would see an enhanced starbursting mode of star formation. Kepley et al. (2014) does find that in M82, compared to normal galaxies, there are regions with higher dense gas fractions. Future observations, resolving star formation in a range of nearby galaxies will help determine how and to what degree $\mathrm{SFE_{dense}}$ varies between galaxies and influences star formation.

Our interferometric observations of M51 reveal that along the spiral arms, dense gas is present but there is a lack of recent massive star formation, Figure 4.16. Since HCN and HCO+ emission is believed to be a signpost for sites of recent star formation, if the local conditions in the gas are such that dense gas is forming, stars should also be forming. The freefall time for the dense gas clumps would be very short, 10^5 yr, It is unlikely that we are catching a specific moment of star formation and stars are yet to form as the spiral arm

passage time is longer than the freefall time. Therefore, this region of the spiral arm is of interest as it appears to have a lower SFE and may support deviations in the linear correlation being caused by SFE_{dense}.

For a lower SFE, a physical mechanism is required that can create dense gas without forming as many stars. This mechanism needs to be specific to M51 as the measurements appear correlated. In the basic standard picture of star formation, there are two main steps required for star formation. In the first step, turbulence allows energy to cascade from large scales to small scales to form dense clumps within the molecular gas. In the second step, these dense clumps gravitationally collapse to form protostars. To explain our observations in the context of a lower SFE, a mechanism that allow for the creation of dense cores but prevent or stunt star formation.

Turbulence is believed to be one of the main drivers responsible for regulating and shaping the ISM. It cascades energy from large scales to smaller scales in ISM. The ability for turbulence to connect the large scales to the smaller scales, provides the coupling of the large scale environment to small scale environments that our observations suggest. On the largest scales, turbulence seems to acts against gravity to prevent GMC collapse. However, on the smaller scales, possibly those probed by HCN and HCO+, turbulence is thought to trigger dense clump formation (Mac Low & Klessen 2004). As turbulence increases, there is an increase in the amount of dense gas formed and star formation only occurs in the few over dense regions that are gravitational bound (Krumholz & McKee 2005). However, if the gas has more kinetic energy it may not be able to collapse into star forming regions. In terms of dense gas formation, turbulence can increase the efficiency of creating dense star forming gas, but another mechanism is required to keep the over dense clumps from gravitationally collapsing to form stars to keep SFE low.

Locally along spiral arms, there exist regions along the spiral arm with high molecular gas surface density but lack recent star formation as highlighted by Meidt et al. (2013). Our observations show dense gas emission along this regions of spiral arm. Since the development of dense gas is the intermediate stage of star formation between bulk molecular gas accumulation and star formation, this region is of interest to understand the processes regulating star formation. Meidt et al. (2013) proposed external negative pressure due to streaming motions in the large-scale galactic environment are responsible for preventing gravitational collapse. This is negative pressure would not allow for any gravitational collapse, but would likely result

in a lack of formation of dense clumps. Although SFE would be low, this external negative pressure is not enough alone to explain both the low SFE and the presence of dense gas.

4.6 Summary

In this chapter we present new sets of maps of the HCN and HCO+ emission in M51. One set of maps shows the central 3 ″ of the disk and the next set of maps shows a region of the western spiral arm . We investigate relationships between HCN, HCO+, CO, and star formation.

- The global distribution of the dense gas is localized along the spiral arms traced by the bulk gas tracer, CO (1-0).
- For intermediate point, the general linear relationship between L_{HCN} & L_{HCO+} and L_{IR} continued to hold, but there is an offset present in the measured points and previous fitted curve, this may be explained by variations in the mass to light ratio and/or SFE
- HCN and HCO+ emission appear coincident with bulk molecular gas, both spatially and with velocity.
- Regions along the spiral arms show dense gas emission without evidence of recent massive star formation.

Chapter 5

Conclusions

In this thesis, we test a new picture of the evolutionary sequence of gas across spiral arms. In this evolutionary sequence, molecular gas, which is present throughout the disk and organized in giant molecular clouds, approaches the gravitational potential of a spiral arm. Upon entry on the upstream side of a spiral arm, GMCs coagulate into larger molecular clouds. During spiral arm crossing, the gas within the molecular clouds becomes inhomogeneous forming over densities. These over dense cores become the future sights of star formation. Newly formed stars are seen exiting the spiral arms on the downstream side of the spiral arm. Using the face on galaxy M51, we investigated two aspects of this proposed evolutionary sequence.

First, we characterized the initial and final stages of the evolutionary sequence of gas picture by measuring the geometrical offsets between atomic and molecular gas emission and star formation tracers, Hα and 24μm in Chapter 3. Our study using CO as a tracer resolved a discrepancy between previously reported offsets (Egusa et al. 2004; Tamburro et al. 2008; Egusa et al. 2009; Foyle et al. 2011). The main cause of the discrepancy came from the choice of gas emission tracers. HI emission peaks appear on the upstream side of the spiral arm, but also appear on the downstream side of the spiral arm due to photo-dissociation due to recently formed stars. This result implies that future studies should use CO, as opposed to HI when measuring offset associated with pre-star forming gas and star formation. Both Hα and 24μm emission can be used for tracing star formation, similar offsets trends are seen between the two of them. A slight preference for using Hα exists in terms of ensuring that the initial and final stages of gas evolution have been observed, however, it is likely that this is not measuring

the initial location where stars are formed, but instead envelope the star formation process. By using Hα one may only be able to determine an upper limit on the high mass star formation timescale. Within that envelope there is likely star formation occurring earlier on spiral arms but is likely not seen due to the high extinction.

Using our measured offsets, we have shown that the offsets are primarily positive, but some scatter is present. The positive offsets suggests that gas is flowing through the spiral arm or density wave, however the scatter implies that the pattern does not need to be stationary single pattern speed. The updated picture of spiral arm gas evolution presented in this thesis, has been developed on the assumption that the gas dynamics are dictated by a density wave and gas is flowing through the spiral arms. The offsets present in Chapter 3 suggest that in the region of the disk where we measured offsets, gas dynamics in M51 are determined by a density wave. Higher resolution observations of M51 also measures similar offsets between CO and 24μm (Schinnerer et al. 2013), but the disk dynamics are likely more complicated. This is also seen in independent measurements of the pattern speed within M51, multiple pattern speeds exist across the disk and dominate in different regions (Meidt et al. 2008). The gas dynamics in M51 prove to be more complicated, but this does not degrade the usefulness of the offset method used in this thesis, but highlight the complexity of the disk dynamics, and potentially the sequence of gas evolution.

Across the disk of M51, it is likely the different dynamical processes dictate the motion of the gas, and thus the impact on star formation. Colombo et al. (2014) divides the disk regions into simple regions, central, arm, and interarm, but they also proceeds to classify the disk of M51 into a wide range of environments. These environments include density wave spiral arms, with upstream and downstream regions of a density wave spiral arms, but also in regions of the disk that appear to be dictated by a material arm. The regions probed in this study falls within Colombo et al. (2014) density wave influenced spiral arms regions. However, this presents an interesting task for future work and also a need for large scale, high resolution mapping of nearby galaxies. There is a need to probe the dynamics of nearby galaxies, but also to see if measurements, like the offsets between the bulk molecular gas and star formation, varies in these different environments and across galaxies. The offset method is one technique that can allow for both the galactic dynamics and the ISM evolution to be studied, many more exist and will be developed as high quality maps of nearby galaxies continue to be observed.

In Chapter 4, we present new sets of HCN and HCO+ maps. These maps were obtained for this thesis using the GBT and CARMA array. This research used these dense gas maps to probe the role of dense gas in the evolutionary sequence of gas across spiral arms by comparing the distribution of dense molecular gas with the bulk molecular gas and recent star formation. These dense gas maps show the emission is isolated along the spiral arms. Using our 400 pc-scale observations taken with the GBT, we tested the relationship previously reported between dense gas luminosity and IR luminosity that spans from Milky Way observation of dense gas cores at parsec scales with observations of nearby galaxies at kilo-parsec scales. (Wu et al. 2005). These new measurements agree with the overall correlation, but there is some deviation suggesting that secondary effects are cause by variations in the dense gas star formation efficiency.

The offsets seen between M51, M82, and the original Wu et al. (2005) relationship suggest that across an individual galaxy, star formation efficiency is similar due to the small scatter of the measured points, but galaxy-to-galaxy variations exist. Similar observations are seen when comparing the bulk molecular gas to star formation in samples of nearby galaxies (Kennicutt & Evans 2012). These galaxy-to-galaxy differences in SFE suggest that there likely a global processes which dictate the SFE more than conditions in localized regions. This may be related to the nature by which stars form, ie. starburst verse disk mode star formation. Further studies of nearby galaxies will help determine if SFE, as probed by dense molecular gas tracers is bimodal or instead exists on a spectrum like is seen in nearby galaxies and GMCs (Bigiel et al. 2008; Keto et al. 2005).

The role of galactic environment continues to have an impact in regards to the dense gas development in disk galaxies. Our 200 pc-scale interferometric observations show that tracers of massive star formation appear on peaks of HCN emission, but there are variations of the dense gas mass along the spiral arms. In addition, we see a hint of evidence of an increased dense gas fraction along spiral arm regions compared to the interarm regions. This suggests that spiral arms not only organize gas, but also play a role in the evolution of the gas. In the Milky Way, similar evolution is seen across spiral arms in CO. The gas appears denser and more structured along spiral arms, and remains more diffuse in the interarm regions (Sawada et al. 2012). The continued and future high resolution mapping of nearby galaxies will help to pinpoint the exact role of spiral arms in this evolutionary sequence.

Dense gas appears to be better correlated with SFR as first seen in (Gao

& Solomon 2004b) and in this thesis we continued to explore this correlation. Looking forward, ALMA and other millimeter instruments, which are sensitive to a wide range of various emission lines which will probe many different aspects of the complex ISM environment. Meier et al. (2015) has shown the wide range of spectra line that can be investigated with ALMA. This will expand our view of the ISM and allow for a better understanding of the ISM through the complex chemistry probed by multi-line surveys. This will help us better understand the role that molecules, like HCN and HCO+, play in the star formation process.

This thesis aimed to test a new evolutionary sequence of gas. Future observations with ALMA and the ongoing CANON survey will continue to study this expanding view of the evolutionary sequence of gas across spiral arm. ALMA will be able to provide the highest resolution observations to date over a wide range of emission lines which will probe many different aspects of the complex ISM environment. In addition, the CANON sample covers a large span of galaxy type and will be able to test this evolutionary sequence of gas used in this thesis in this range of different galaxies to study if this evolutionary sequence is unique to M51 or universal across galaxy types. The work presented in this thesis creates solid foundation from which to explore more complicated aspects of gas evolution, global dynamics, and star formation.

Bibliography

Allen, R. J. 2002, in Astronomical Society of the Pacific Conference Series, Vol. 276, Seeing Through the Dust: The Detection of HI and the Exploration of the ISM in Galaxies, ed. A. R. Taylor, T. L. Landecker, & A. G. Willis, 288

Barnes, P. J., Yonekura, Y., Fukui, Y., et al. 2011, ApJS, 196, 12

Bendo, G. J., Galliano, F., & Madden, S. C. 2012, MNRAS, 423, 197

Bigiel, F., Leroy, A., Walter, F., et al. 2008, AJ, 136, 2846

Binney, J., & Tremaine, S. 2008, Galactic Dynamics: Second Edition (Princeton University Press)

Blitz, L. 1993, in Protostars and Planets III, ed. E. H. Levy & J. I. Lunine, 125–161

Blitz, L., Fukui, Y., Kawamura, A., et al. 2007, Protostars and Planets V, 81

Blitz, L., & Williams, J. P. 1999, ArXiv Astrophysics e-prints, astro-ph/9903382

Block, D. L., & Wainscoat, R. J. 1991, Nature, 353, 48

Bolatto, A. D., Wolfire, M., & Leroy, A. K. 2013, ARA&A, 51, 207

Buchbender, C., Kramer, C., Gonzalez-Garcia, M., et al. 2013, A&A, 549, A17

Burke, B. F., & Graham-Smith, F. 2009, An Introduction to Radio Astronomy

Colombo, D., Hughes, A., Schinnerer, E., et al. 2014, ApJ, 784, 3

Dale, D. A., & Helou, G. 2002, ApJ, 576, 159

Dame, T. M., Elmegreen, B. G., Cohen, R. S., & Thaddeus, P. 1986, ApJ, 305, 892

Dobbs, C., & Baba, J. 2014, PASA, 31, 35

Dobbs, C. L., & Pringle, J. E. 2010, MNRAS, 409, 396

D'Onghia, E., Vogelsberger, M., & Hernquist, L. 2013, ApJ, 766, 34

Donovan Meyer, J., Koda, J., Momose, R., et al. 2013, ApJ, 772, 107

Egusa, F., Koda, J., & Scoville, N. 2011, ApJ, 726, 85

Egusa, F., Kohno, K., Sofue, Y., Nakanishi, H., & Komugi, S. 2009, ApJ, 697, 1870

Egusa, F., Sofue, Y., & Nakanishi, H. 2004, PASJ, 56, L45

Emerson, D. T., & Graeve, R. 1988, A&A, 190, 353

Enoch, M. L., Glenn, J., Evans, II, N. J., et al. 2007a, ApJ, 666, 982

—. 2007b, ApJ, 666, 982

Evans, N. J., Dunham, M. M., Jorgensen, J. K., et al. 2009, VizieR Online Data Catalog, 218, 10321

Falgarone, E., Pety, J., & Hily-Blant, P. 2009, A&A, 507, 355

Foster, J. B., Jackson, J. M., Barnes, P. J., et al. 2011, ApJS, 197, 25

Foyle, K., Rix, H.-W., Dobbs, C. L., Leroy, A. K., & Walter, F. 2011, ApJ, 735, 101

Fujii, M. S., Baba, J., Saitoh, T. R., et al. 2011, ApJ, 730, 109

Gao, Y., & Solomon, P. M. 2004a, ApJS, 152, 63

—. 2004b, ApJ, 606, 271

García-Burillo, S., Usero, A., Alonso-Herrero, A., et al. 2012, A&A, 539, A8

Girart, J. M., Estalella, R., Ho, P. T. P., & Rudolph, A. L. 2000, ApJ, 539, 763

Goldreich, P., & Kwan, J. 1974, ApJ, 189, 441

Goldreich, P., & Lynden-Bell, D. 1965, MNRAS, 130, 125

Gould, R. J., Gold, T., & Salpeter, E. E. 1963, ApJ, 138, 408

Graciá-Carpio, J., García-Burillo, S., Planesas, P., Fuente, A., & Usero, A. 2008, A&A, 479, 703

Heiderman, A., Evans, II, N. J., Allen, L. E., Huard, T., & Heyer, M. 2010, ApJ, 723, 1019

Helfer, T. T., & Blitz, L. 1993, ApJ, 419, 86

Helfer, T. T., Thornley, M. D., Regan, M. W., et al. 2003, ApJS, 145, 259

Hirota, A., Kuno, N., Sato, N., et al. 2011, ApJ, 737, 40

Ho, L. C., Filippenko, A. V., & Sargent, W. L. W. 1997, ApJS, 112, 315

Hughes, A., Wong, T., Ott, J., et al. 2010, MNRAS, 406, 2065

Hughes, A., Meidt, S. E., Colombo, D., et al. 2013, ApJ, 779, 46

Juneau, S., Narayanan, D. T., Moustakas, J., et al. 2009, ApJ, 707, 1217

Kalnajs, A. J. 1965, PhD thesis, HARVARD UNIVERSITY.

Kennicutt, R. C., & Evans, N. J. 2012, ARA&A, 50, 531

Kennicutt, R. C., Calzetti, D., Aniano, G., et al. 2011, PASP, 123, 1347

Kennicutt, Jr., R. C., Armus, L., Bendo, G., et al. 2003, PASP, 115, 928

Kepley, A. A., Leroy, A. K., Frayer, D., et al. 2014, ApJLett, 780, L13

Keto, E., Ho, L. C., & Lo, K.-Y. 2005, ApJ, 635, 1062

Klessen, R. S., & Glover, S. C. O. 2014, ArXiv e-prints, arXiv:1412.5182

Klessen, R. S., & Hennebelle, P. 2010, A&A, 520, A17

Koda, J., & Sofue, Y. 2006, PASJ, 58, 299

Koda, J., Scoville, N., Sawada, T., et al. 2009, ApJLett, 700, L132

Koda, J., Sawada, T., Wright, M. C. H., et al. 2011, ApJS, 193, 19

Koda, J., Scoville, N., Hasegawa, T., et al. 2012, ApJ, 761, 41

Kohno, K., Kawabe, R., Tosaki, T., & Okumura, S. K. 1996, ApJLett, 461, L29

Kolmogorov, A. 1941, Akademiia Nauk SSSR Doklady, 30, 301

Krips, M., Neri, R., García-Burillo, S., et al. 2008, ApJ, 677, 262

Krumholz, M. R., & McKee, C. F. 2005, ApJ, 630, 250

Lada, C. J., Alves, J. F., & Lombardi, M. 2007, Protostars and Planets V, 3

Lada, C. J., Forbrich, J., Lombardi, M., & Alves, J. F. 2012, ApJ, 745, 190

Lada, C. J., & Lada, E. A. 2003, ARA&A, 41, 57

Lada, C. J., Lombardi, M., & Alves, J. F. 2010, ApJ, 724, 687

Lada, E. A. 1992, ApJLett, 393, L25

Larson, R. B. 1981, MNRAS, 194, 809

Lee, J. H., Hwang, N., & Lee, M. G. 2011, ApJ, 735, 75

Leroy, A., Bolatto, A., Stanimirovic, S., et al. 2007, ApJ, 658, 1027

Leroy, A. K., Walter, F., Bigiel, F., et al. 2009, AJ, 137, 4670

Lin, C. C., & Shu, F. H. 1964, ApJ, 140, 646

—. 1966, Proceedings of the National Academy of Science, 55, 229

Lindblad, B. 1963, Stockholms Observatoriums Annaler, 22, 5

Lintott, C., Schawinski, K., Bamford, S., et al. 2011, MNRAS, 410, 166

Liu, G., Koda, J., Calzetti, D., Fukuhara, M., & Momose, R. 2011, ApJ, 735, 63

Loison, J.-C., Wakelam, V., & Hickson, K. M. 2014, MNRAS, 443, 398

Louie, M., Koda, J., & Egusa, F. 2013, ApJ, 763, 94

Ma, B., Tan, J. C., & Barnes, P. J. 2013, ApJ, 779, 79

Mac Low, M.-M., & Klessen, R. S. 2004, Reviews of Modern Physics, 76, 125

Mac Low, M.-M., Klessen, R. S., Burkert, A., & Smith, M. D. 1998, Physical Review Letters, 80, 2754

Mangum, J., Emerson, D., & Greisen, E. 2000, in Astronomical Society of the Pacific Conference Series, Vol. 217, Imaging at Radio through Submillimeter Wavelengths, ed. J. G. Mangum & S. J. E. Radford, 179

Masters, K. L., Nichol, R. C., Hoyle, B., et al. 2011, MNRAS, 411, 2026

Matsushita, S., Trung, D.-V., Boone, F., et al. 2015, ApJ, 799, 26

Meidt, S. E., Rand, R. J., Merrifield, M. R., Shetty, R., & Vogel, S. N. 2008, ApJ, 688, 224

Meidt, S. E., Schinnerer, E., García-Burillo, S., et al. 2013, ApJ, 779, 45

Meier, D. S., Walter, F., Bolatto, A. D., et al. 2015, ApJ, 801, 63

Mentuch Cooper, E., Wilson, C. D., Foyle, K., et al. 2012, ApJ, 755, 165

Mo, H., van den Bosch, F. C., & White, S. 2010, Galaxy Formation and Evolution

Nguyen, Q.-R., Jackson, J. M., Henkel, C., Truong, B., & Mauersberger, R. 1992a, ApJ, 399, 521

—. 1992b, ApJ, 399, 521

Oh, S. H., Kim, W.-T., Lee, H. M., & Kim, J. 2008, ApJ, 683, 94

Onodera, S., Koda, J., Sofue, Y., & Kohno, K. 2004, PASJ, 56, 439

Papadopoulos, P. P. 2007, ApJ, 656, 792

Parkin, T. J., Wilson, C. D., Schirm, M. R. P., et al. 2013, ApJ, 776, 65

Radford, S. J. E., Downes, D., & Solomon, P. M. 1991, ApJLett, 368, L15

Rebolledo, D., Wong, T., Leroy, A., Koda, J., & Donovan Meyer, J. 2012, ApJ, 757, 155

Regan, M. W., Thornley, M. D., Helfer, T. T., et al. 2001, ApJ, 561, 218

Richardson, L. F. 1920, Royal Society of London Proceedings Series A, 97, 354

Rieke, G. H., Lebofsky, M. J., Thompson, R. I., Low, F. J., & Tokunaga, A. T. 1980, ApJ, 238, 24

Rix, H.-W., & Rieke, M. J. 1993, ApJ, 418, 123

Roberts, W. W. 1969, ApJ, 158, 123

Rohlfs, K., & Wilson, T. L. 2000, Tools of radio astronomy

Sánchez-Gil, M. C., Jones, D. H., Pérez, E., et al. 2011, MNRAS, 415, 753

Sanders, D. B., & Mirabel, I. F. 1996, ARA&A, 34, 749

Sanders, R. H., & Huntley, J. M. 1976, ApJ, 209, 53

Sault, R. J., Teuben, P. J., & Wright, M. C. H. 1995, in Astronomical Society of the Pacific Conference Series, Vol. 77, Astronomical Data Analysis Software and Systems IV, ed. R. A. Shaw, H. E. Payne, & J. J. E. Hayes, 433

Sawada, T., Hasegawa, T., & Koda, J. 2012, ApJLett, 759, L26

Schinnerer, E., Meidt, S. E., Pety, J., et al. 2013, ApJ, 779, 42

Scoville, N. Z. 1990, in Astronomical Society of the Pacific Conference Series, Vol. 12, The Evolution of the Interstellar Medium, ed. L. Blitz, 49–61

Scoville, N. Z., Polletta, M., Ewald, S., et al. 2001, AJ, 122, 3017

Scoville, N. Z., & Sanders, D. B. 1987, in Astrophysics and Space Science Library, Vol. 134, Interstellar Processes, ed. D. J. Hollenbach & H. A. Thronson, Jr., 21–50

Scoville, N. Z., & Solomon, P. M. 1974, ApJLett, 187, L67

Sellwood, J. A. 2013, Dynamics of Disks and Warps, ed. T. D. Oswalt & G. Gilmore, 923

Sellwood, J. A., & Balbus, S. A. 1999, ApJ, 511, 660

Sellwood, J. A., & Carlberg, R. G. 1984, ApJ, 282, 61

Sofue, Y., Tutui, Y., Honma, M., et al. 1999, ApJ, 523, 136

Solomon, P. M., Rivolo, A. R., Barrett, J., & Yahil, A. 1987, ApJ, 319, 730

Solomon, P. M., Sanders, D. B., & Scoville, N. Z. 1979, ApJLett, 232, L89

Spitzer, L. 1978, Physical processes in the interstellar medium

Tamburro, D., Rix, H.-W., Walter, F., et al. 2008, AJ, 136, 2872

Thompson, A. R., Moran, J. M., & Swenson, Jr., G. W. 2001, Interferometry and Synthesis in Radio Astronomy, 2nd Edition

Thornley, M. D. 1996, ApJLett, 469, L45

Toomre, A. 1981, in Structure and Evolution of Normal Galaxies, ed. S. M. Fall & D. Lynden-Bell, 111–136

Toomre, A., & Toomre, J. 1972, ApJ, 178, 623

Usero, A., Leroy, A. K., Walter, F., et al. 2015a, ArXiv e-prints, arXiv:1506.00703

—. 2015b, ArXiv e-prints, arXiv:1506.00703

Vogel, S. N., Kulkarni, S. R., & Scoville, N. Z. 1988, Nature, 334, 402

Wada, K. 1994, PASJ, 46, 165

—. 2008, ApJ, 675, 188

Wada, K., Baba, J., & Saitoh, T. R. 2011, ApJ, 735, 1

Walter, F., Brinks, E., de Blok, W. J. G., et al. 2008, AJ, 136, 2563

Watanabe, Y., Sakai, N., Sorai, K., & Yamamoto, S. 2014, ApJ, 788, 4

Williams, J. P., de Geus, E. J., & Blitz, L. 1994, ApJ, 428, 693

Wu, J., Evans, II, N. J., Gao, Y., et al. 2005, ApJLett, 635, L173

Wu, J., Evans, II, N. J., Shirley, Y. L., & Knez, C. 2010, ApJS, 188, 313

Yang, B., Stancil, P. C., Balakrishnan, N., & Forrey, R. C. 2010, ApJ, 718, 1062

Young, J. S., & Devereux, N. A. 1991, ApJ, 373, 414

Young, J. S., & Scoville, N. Z. 1991a, ARA&A, 29, 581

—. 1991b, ARA&A, 29, 581

Appendix A

CANON Survey Overview

The CANON - **CA**RMA-**NO**BEYAMA **N**earby-galaxy CO (1-0) Survey, PI Jin Koda, is a survey of 29 northern spiral galaxies. The survey combines observations from the CARMA array and the Nobeyama 45m single dish telescope. CARMA is a 15 antennae interferometer made up of nine 6m antennae from the Berkeley Illinois Maryland Association (BIMA) array and six 10m antennae from the OVRO array. The Nobeyama dish is a 45m single dish at the Noybeyama Radio Observatory.

The goal of the survey is to measure CO and ^{13}CO in a sample of northern spiral galaxies to investigate GMC properties and their variation across galactic environment, molecular gas fraction, and star formation laws. The survey targets a wide range spiral types (flocculent, intermediate, and grand design). These galaxies can not be observed by ALMA due to their location in the northern hemisphere. The sample has been selected to match observations taken with the Spitzer/SINGS and Herschal KINGFISH sample (Kennicutt et al. 2003, 2011). Many of the galaxies have archival data from the THINGS survey (Walter et al. 2008) and past Hubble Space Telescope observations. The sample of galaxies and some basic properties are shown in Table A. The CANON survey will be one of the largest surveys of molecular gas in nearby spiral galaxies.

Since Spring 2012, approximately 600 hours of CARMA observations have been obtained. This represents approximately half of the total CARMA data required for this survey. These data was obtained in the second generation of CANON interferometry data collection. Between Spring 2012 and Summer 2014, I have lead the reduction and calibration of the CARMA observations. The reminder of this section will describe the the observation goals, data

collection processes, and calibration of the CARMA data I performed for the CANON sample.

The observations were designed to map the central 2-3′ of the sample galaxies with 2-3″ resolution. Interferometric observations were done in both C and D CARMA array configuration with baseline lengths of 26 - 370m and 11 - 148m, respectively, using 15 antennas in 19 pointings. Some galaxies were mapped with only 7 pointings due to their smaller angular size on the sky. OTF maps of the galaxies are made with the Nobeyama 45m telescope. The CARMA observations provide the high resolution imaging and the Nobeyama observations provide total flux information by adding in the short baselines CARMA can not observe, including V(0,0). This short spacing problem see with interferometric data is described in §2.2.1.

The observations were preformed by onsite observers using observing scripts generated and verified locally at Stony Brook before being submitted to the observatory. The observations were made with the 16 sideband receiver, eight upper sidebands and eight lower sidebands. For the CANON survey, we only use the data collected in the upper sideband. A graphical display of the frequency configuration for the upper sideband are shown in Figure A.2. The two black lines around 110 and 115 GHz correspond to the ^{13}CO and CO emission lines, respectfully. Four of the sidebands are aligned to observe CO and the other four are aligned to observe ^{13}CO. There is a wide band with a 500MHz bandwidth and three adjacent 62MHz bandwidth narrow bands centered on the emission line. The wide band data was used for calibration purposes whereas the narrow bands will be used for analysis.

A mosaicing technique is used to cover the 2 - 3′ region around the galaxy, which makes observations at multiple points. The field-of-views for each pointing overlap to obtain constant sensitivity over a wider range than a single pointing. For most of the galaxies, a 19-point mosaic is used. The number of pointings used per galaxy can be seen in Table A. This overlapping observing pattern mosaic can be seen in Fig. A.1 for a 19-point pattern. The observations constantly rotate between the 19 pointings to ensure that the sky is sampled evenly over the full FOV.

CANON survey data was collected between March 2012 and December 2013. Once data was collected and released by the observatory, usually within 24 hours after observations, I visually inspected the data locally at Stony Brook. Any problems with the data, not highlighted by the observatory, were recorded. Any concerns I saw were reported at weekly observer telecons ran by CARMA. After a visual inspection of the data, similar calibration

Table A.1. CANON Survey Details

Galaxy Name	# of Mosaic Pointings	Distance (Mpc)	Arm Class	V_{hel} (km/s)
NGC 3034	19	3.5		203
NGC 6946	19	5.5	9	48
NGC 5194	151	8.2	12	463
NGC 3627	19	8.9	7	727
NGC 4631	19	9.0		606
NGC 4736	19	5.3	3	308
NGC 3521	19	9.0	3	805
NGC 5055	19	8.2	3	504
NGC 4254	19	20.0	9	2407
NGC 7331	19	15.7		816
NGC 4536	19	25.0		1808
NGC 2403	19	3.5	4	131
NGC 4321	45	20.0	12	1571
NGC 2798	7	24.7		1726
NGC 4826	19	5.6	6	24.7
NGC 3351	19	9.3	6	778
NGC 5195	7	8.2		552
NGC 0628	19	11.4	9	657
NGC 5033	19	13.3	9	875
NGC 4569	19	20.0		-235
NGC 2976	19	3.5	3	3
NGC 3031	19	3.5	12	-34
NGC 3184	19	8.6	9	592
NGC 3938	19	12.2	9	809
NGC 3198	19	9.8		663
NGC 4559	19	11.6		816
Mrk33	7	21.7		1461
NGC 2841	19	9.8		638
NGC 4579	19	20.0	9	1519

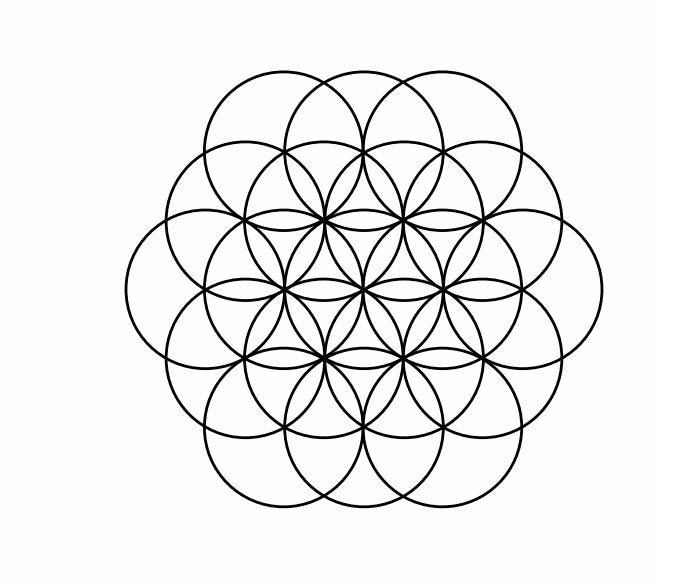

Figure A.1 Mosaic pattern for 19-point observations for CANON galaxies from the CARMA observatory.

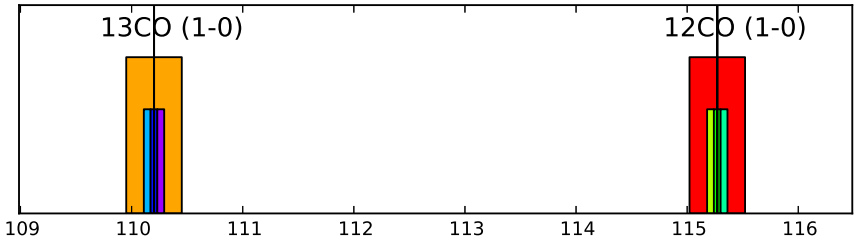

Figure A.2 Graphical display of the upper sideband frequency configuration for the CANON galaxies survey CARMA observations.

steps as described above in §2.2.4 were performed. In the summer of 2014, I completed the data calibration for all the CARMA data. The Nobeyama data is in the final data collection stages. For the galaxies where all the data has been collected, the two sets of data are in the process of being combined and imagined for analysis. Although the final data products from this survey were not available in time to be analyzed for this thesis work, a significant amount of work went into leading the calibration of these data.